Microfluidic Studies of Interfacial Transport

Elif Karatay

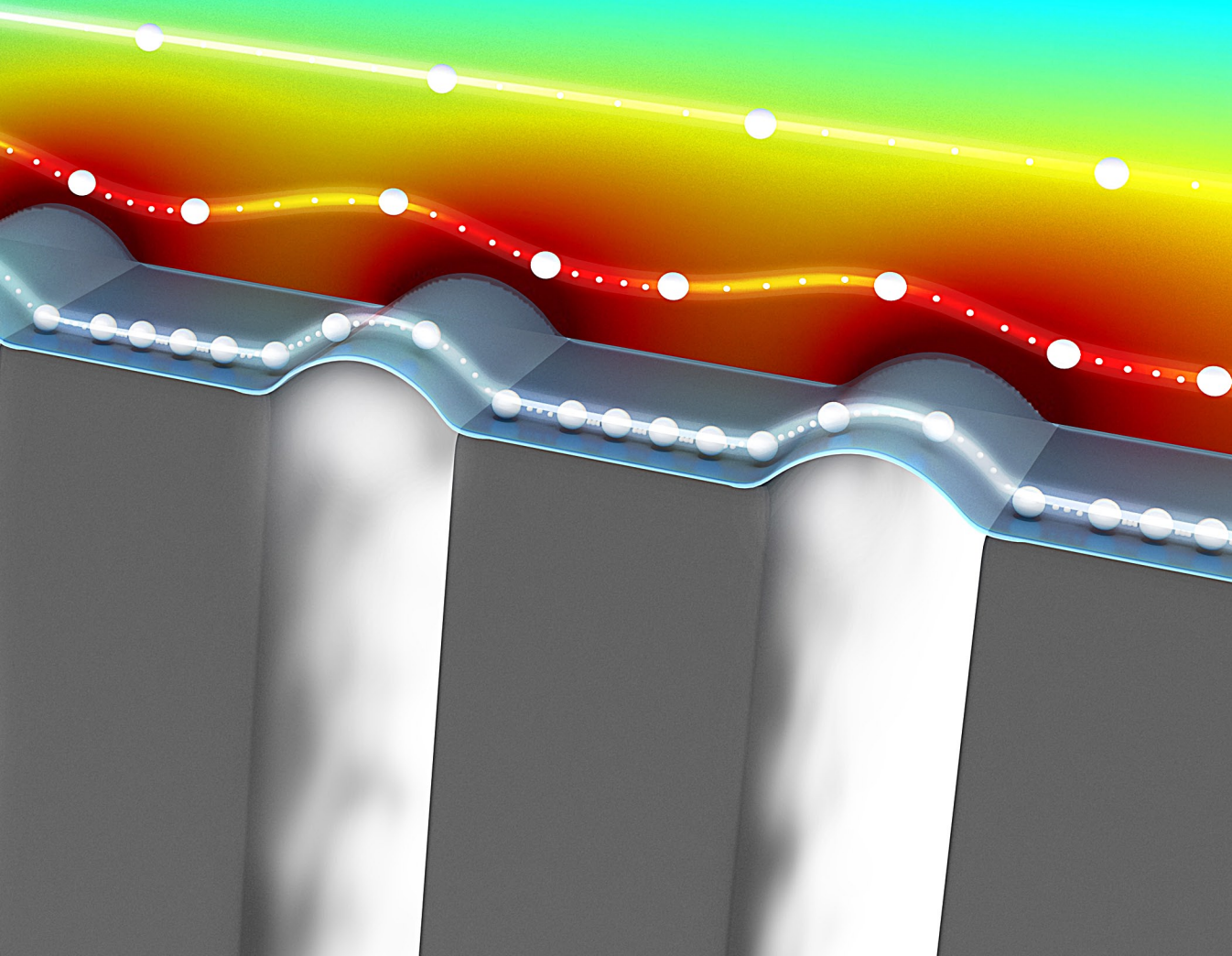

MICROFLUIDIC STUDIES
OF
INTERFACIAL TRANSPORT

The research presented in this thesis was supported financially by the Process on a Chip programme (PoaC project number 053.65.007), which is part of Advanced Chemical Technologies for Sustainability (ACTS).

Promotion committee
Prof. Dr. Gerard van der Steenhoven (Chairman)

Prof. Dr. Ir. R. G. H. (Rob) Lammertink (Promotor)
Assist. Prof. Dr. Peichun Amy Tsai (Assistant Promotor)

Prof. Dr. Ing. Matthias Wessling
Prof. Dr. Detlef Lohse
Prof. Dr. Han Gardeniers
Assoc. Prof. Dr. Jens Harting
Assist. Prof. Dr. Ali Mani

Cover is designed by Elif Karatay and prepared by Jonathan Bennink, Tingle.

Microfluidic Studies of Interfacial Transport
ISBN:978-90-365-0691-5
DOI:10.3990/1.9789036506915
URL: http://dx.doi.org/10.3990/1.9789036506915

Printed by Gildeprint Drukkerij, Enschede, The Netherlands

MICROFLUIDIC STUDIES OF INTERFACIAL TRANSPORT

DISSERTATION

to obtain
the degree of doctor at the University of Twente,
on the authority of the rector magnificus,
prof. dr. H. Brinksma,
on account of the decision of the graduation committee,
to be publicly defended
on Friday 27 September 2013 at 16.45

by

Elif Karatay
born on 1984
in Isparta, Turkey

This thesis is approved by:
Prof. Dr. Ir. R. G. H. (Rob) Lammertink (promotor)
Assist. Prof. Dr. Peichun Amy Tsai (assistant-promotor)

To
My Mother Emel Karatay
and
Celal Cem Alp

Contents

1 Introduction **1**

1.1 Background 3

1.1.1 Gas Liquid Contacting 3

1.1.2 Ion Concentration Polarization 8

1.2 Scope of the Thesis 13

2 Oxygenation by a superhydrophobic slip G/L contactor **23**

2.1 Introduction 24

2.2 Experimental 26

2.2.1 Glass Chips 26

2.2.2 Membranes 26

2.2.3 Chip Assembly 27

2.2.4 Experiments and Set-up 28

2.3 Numerical Analysis 29

2.4 Results and Discussion 31

2.4.1 Numerical Simulations 31

2.4.2 Membrane Morphology 33

2.4.3 Gas Transport 36

2.5 Conclusions 41

3 Transport on Bubble Mattresses **47**
3.1 Introduction . . . 48
3.2 Numerical Simulations . . . 50
3.2.1 Evaluation of Effective Slippage . . . 52
3.2.2 Evaluation of Mass Transfer Enhancements . . . 53
3.3 Results and Discussion . . . 55
3.3.1 Momentum Transport . . . 55
3.3.2 Interfacial Mass Transport . . . 57
3.4 Conclusions . . . 61

4 Control of Slippage with Tunable Bubble Mattresses **67**
4.1 Introduction . . . 68
4.2 Experimental . . . 68
4.2.1 Microfluidic Device . . . 68
4.2.2 μPIV Experiments . . . 70
4.2.3 Calculation of Effective Slip Length . . . 71
4.2.4 Calculation of Effective Friction Factor . . . 71
4.3 Results and Discussion . . . 73
4.3.1 Measured Velocity Profiles . . . 73
4.3.2 Comparison of b_{eff} with the analytical asymptotic solutions . . . 76
4.3.3 Dependence of Hydrodynamic Slippage on Bubble Geometry . . . 78
4.4 Conclusions . . . 81

5 Rate of Gas Absorption on a Slippery Bubble Mattress **85**
5.1 Introduction . . . 86
5.2 Experimental Methods . . . 88
5.2.1 Microfluidic Setup . . . 88
5.2.2 FLIM Experiments . . . 89
5.3 Numerical Simulations . . . 91
5.3.1 Governing Equations . . . 91
5.3.2 Mass Transfer Boundary Conditions . . . 93
5.4 Results and Discussion . . . 96
5.4.1 FLIM Measurements . . . 96
5.5 Rate of O_2 Absorption . . . 97
5.6 Conclusions . . . 105

6 Ion Selective Membranes in Microfluidics **113**
6.1 Introduction . . . 114
6.2 Experimental Methods . . . 115
6.2.1 Membrane Preparation . . . 115
6.2.2 Characterization of Membranes . . . 116
6.2.3 Microfluidic Setup . . . 118
6.3 Results and Discussion . . . 123
6.3.1 Membrane Formulation and Characterization . . . 123
6.3.2 Swelling Behavior of Batch Membranes . . . 127
6.3.3 Microfluidic Ion Exchange Membranes . . . 132
6.4 Conclusions . . . 145

7 Summary and Outlook **151**
7.1 Summary . . . 151
7.2 Outlook . . . 155
7.2.1 Gas Liquid Contacting . . . 155
7.2.2 Charged Interfaces in Microfluidics . . . 161
7.3 Samenvatting . . . 167

Acknowledgements **177**

Appendices **179**

A Conductivity Measurements **179**
A.1 Calibration of the Impedance Analyzer . . . 179
A.2 Description of the Impedance Analyzer . . . 183

List of Figures

1.1 Illustration of concentration polarization 4
1.2 Mass transfer correlations of non-wetted porous hollow fiber gas-liquid contacting membranes. 5
1.3 A schematic illustration of hydrodynamic slippage 7
1.4 Simplified schematic representation of classical electrodialysis 9
1.5 Schematic representation of micro and nano channel intersections 12

2.1 PVDF membrane integrated G/L contacting micro-device . 28
2.2 2D and 3D numerical simulations 32
2.3 Effect of internal membrane structure 37
2.4 Average outlet oxygen concentrations obtained for different channel depths as functions of residence time 39
2.5 Oxygen mass transfer with micro-structured membranes . . 40

3.1 Microbubble mattress configuration 50
3.2 Dimensionless effective slip length $2b_{eff}/L_g$ profiles as functions of protrusion angles θ and surface porosities φ 56
3.3 Numerical results of the pressure-driven flow over a microbubble unit at $\varphi = 0.5$ for varying protrusion angles 56

3.4 Dissolved species mass flux enhancement E^{ψ}, fluid flux enhancement E^{ϕ} and enhancement of outlet bulk concentration E^{c} as functions of protrusion angles θ and surface porosities φ 59

4.1 Controllable microfluidic bubble mattress and computational bubble unit cell 69
4.2 Experimental microbubble units 74
4.3 Detailed velocity profiles measured by μPIV 75
4.4 Average velocity profiles measured by μPIV 76
4.5 Experimental and numerical effective slip lengths b_{eff} as functions of the protrusion angle θ and surface porosity φ . 79
4.6 Experimental and numerical effective friction factor C_f and numerical drag reduction as functions of the protrusion angle θ and surface porosity φ 80

5.1 Microfluidic bubble mattress and oxygen dissolution at bubble surfaces 90
5.2 Schematic illustration of the applied boundary conditions and the effects of interface resistances on the concentration profiles in the presence of liquid flow 93
5.3 Successive lifetime fields in axial position x 98
5.4 Experimental and numerical local dissolved oxygen profiles 99
5.5 Successive local dissolved oxygen profiles at different axial x positions and local convective oxygen flux 102
5.6 O_2 fluxes J_{O_2} as functions of axial x positions and Re obtained by FLIM measurements and numerical calculations . 103

6.1 Selective UV irradiation by photo-masking 119
6.2 Impedance Measurements 121
6.3 Photo-polymerization of DADMAC 124
6.4 Photo-crosslinking of poly(DADMAC) 124
6.5 Photo-crosslinking of poly(DADMAC) and p(VP) 125

6.6 ATR-FTIR spectra of binary component membranes with different compositions 126
6.7 ATR-FTIR spectra for different crosslinking densities 127
6.8 Effects of the membrane composition on swelling 129
6.9 The effect of ionic strength of the electrolyte solutions on the swelling 131
6.10 The layout of the microfluidic chips 132
6.11 Different types of microfluidic devices 133
6.12 In-situ fabrication of pure DADMAC membranes 134
6.13 Selective UV exposure of stationary DADMAC/NVP solutions 135
6.14 Membranes with controllable swelling properties prepared by the developed fabrication method 137
6.15 Experimental and numerical local salt concentration profiles as a function of diffusion time 138
6.16 Current-Voltage (I-U) measurements 140
6.17 Visualization of local charge transport 141
6.18 Microscope images of a solution seeded with particles under DC bias 143
6.19 Image stack of fluorescent particles in a three-channel design chip 144

7.1 Slippage on deforming bubbles. 157
7.2 Marangoni mixing on a slippery porous membrane. 160
7.3 Schematic representation of some critical parameters for ICP at OLC. 162
7.4 Micro/nano-fluidic devices 163
7.5 Developing ion depletion/enrichment layers in initially static flow conditions 164
7.6 Transient nature of ICP at OLC under pressure-driven flow 165

A.1 Conductivities of the stock solutions as a function of salt concentration. 179

A.2 A representative measured Bode plot 180
A.3 Measured and calculated cell constants K_{cell} 181
A.4 The block diagram of the in-house built impedance analyzer 183
A.5 Trans-impedance amplifier unit on the chip holder 185
A.6 Power supply and post-amplifier units of the impedance analyzer 186
A.7 Gain-phase detector and logarithmic detector units of the impedance analyzer 187

List of Tables

2.1 Internal characteristics of home made membranes in comparison to commercial membrane 34
2.2 Contact angle measurements of flat/micro-structured membranes 35

4.1 Comparison of effective slip length results with the asymptotic limits 77

6.1 All compositions of the prepared membranes 117

1

Introduction

Originally emerging from the field of analytical chemistry, micro total analysis (μTAS) systems and lab-on-chip (LOC) systems have evolved dramatically since the early 1990's. Due to the availability of rapidly developing micro/nano-fabrication techniques, the field has received enormous attention in various disciplines. μTAS and LOC systems are widespread and find use in many scientific and industrial contexts. [1] The wide range of microfluidic studies include; (i) microsensors with fluidic components (*e.g.* valves, pumps and flow sensors), (ii) miniaturization of analytical chemical tools such as filters, needles, mixers, (iii) chemical separations, (iv) portable bio/chemical handling and analysis systems, (v) microreaction technology and process intensification, (vi) life sciences related applications (*e.g.* point-of-care diagnostics, drug release, biological scaffolds, assays and cell analysis, high-throughput DNA sequencing). [1–5]

Besides these tremendous number of diverse applications, the fundamental studies of physical, chemical and biological processes in microsystems are growing substantially. The utilized microdevices have often complex geometries consisting of networks of channels and complicated local microstructures. Therefore, the design and optimization of these devices require an interplay of multiple physical effects. Regarding the fluid transport in most of the microfluidic systems, pressure gradients, electrokinetics and capillarity often play a crucial role. Complex relationships can

arise between the physical characteristics of the micro/nano-channels and the behavior of the fluids flowing through these channels. The fluid constitutive relations are strongly affected by the existence of the strongly confined boundaries in microfluidic devices. Investigation of fundamental physical processes at the corresponding scales give key insights into the development of LOC systems. Furthermore, these circumstances lead to interesting variants of well-studied fluid dynamical problems and some new fluid responses near confined interfaces in microfluidics. [1, 7]

In micro-scale systems, the relative importance of the forces acting on a fluid element changes compared to the macro-regime. The volume forces like gravity and inertia which are prominent in macro-scale become negligible in microfluidic systems. [6] As the characteristic length scales are diminished, surface interactions become dominant in microfluidics compared to the behavior of the bulk. These surface forces including interfacial tension effects, molecular level forces as hydrophilic/hydrophobic interactions, electrohydrodynamics near charged interfaces are often used in manipulation of microflows. Integrating such interfaces in microfluidic devices is highly attractive for exploiting both applied and fundamental aspects of such complex fluid flow phenomena dominated by interfacial forces.

The transport phenomena at interfaces often determine or limit the process performance, as also encountered in macro-scale systems. Therefore, direct investigations of interfacial transport of momentum, mass and heat at the interfaces in micron scale are highly appreciable for further optimization of various micro- and macro- scale technologies. Microfluidics offer an ideal platform allowing for the integration of surfaces with precise and controllable interfaces and direct measurements of transport phenomena driven at these interfaces. Within this context, interfacial mass and momentum transport near (i) soft gas-liquid interfaces and (ii) charged ion selective interfaces are studied in the presented study. The momentum and mass transfer near gas-liquid interfaces established in porous hydrophobic polymeric substrates (**Chapter 2**) and in hydrophobic silicon microgrooves (**Chapters 3-5**) are thoroughly investigated. Regarding the ion selective boundaries, the integration of tailored-hydrogels (**Chapter 6**) and micro/nano-channel intersections (**Chapter 7**) within microfluidic platforms is described, providing a promising outlook on the associated

ion transport.

1.1 Background

1.1.1 Gas Liquid Contacting

The presence of a liquid flowing adjacent to a porous medium is common in many engineering problems ranging from groundwater hydrology to membrane based processes where characterization for both fluid dynamics and the porous medium, *e.g.* permeability and porosity, becomes important. [11] Membrane contactors have been suggested for various conventional industrial processes such as distillation, extraction and gas absorption/stripping. [12] In these processes, gas-liquid phases and liquid-liquid phases are separated by a porous membrane which only acts as a stabilizing interface. In general, it is not the enhanced transport properties but rather the large area to volume ratios that have attracted attention in membrane based contacting in comparison to conventional dispersed phase contactors. [12–14] Other advantages of membrane based contacting are the elimination of flooding and entrainment of the dispersed phase due to the hydrodynamic decoupling of different phases. [12, 14]

Concentration Polarization

In processes that involve transport of mass across an interface, concentration gradients establish at each side of the interface. This phenomenon is often called as concentration polarization. [13] Similar polarization phenomena at interfaces occur during the transport of heat and charge. Figure 1.1 illustrates the formation of concentration polarization gradients on both sides of a porous membrane contacting gas and liquid under forced convection. The mass transfer resistance, and hence the polarization in the gas phase is commonly neglected due to the fast diffusion of gases. The mass transfer resistance in the liquid phase flowing adjacent to the membrane surface determines the concentration profiles of the dissolved gas and thereby the interfacial transport rates. As shown in Figure 1.1, for a liquid flowing in laminar regime, the shear stress at the membrane interface affects the evolution of the concentration polarization profiles.

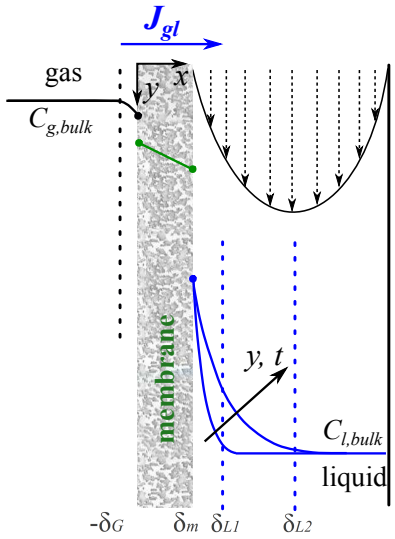

Figure 1.1: Illustration of concentration polarization in membrane based gas-liquid contacting The concentration gradients are shown in gas phase, gas filled porous membrane (δ_m) and the liquid phase flowing in laminar regime. The boundary layer thicknesses in gas (δ_G) and liquid phases (δ_{L1}, δ_{L2}) are depicted by dash lines. The liquid side boundary layer thicknesses increase as the liquid flows downstream (y) or as the residence time (t) increase.

In membrane based gas-liquid contactors, the membrane is often reported as a separate phase inducing additional mass transfer limitation and hence contributing to the overall mass transfer resistance. [12–14] Mass transfer characteristics of membrane gas-liquid contactors have been widely studied for two concepts where the pores of the membrane are either filled with the gas phase or with the liquid phase. [12, 15] The overall mass transfer resistances have been expressed by 'resistance-in-series' models taking into consideration the resistances of the gas phase, the membrane phase, and the liquid phase. [12, 15]

The mass transfer characteristics of gas absorption/desorption have been investigated in various experimental and theoretical studies with a focus on porous membrane characteristics such as wettability, gas permeance and porosity to obtain operation stability over a large range of gas

and liquid flows. [15–18] The effects of surface porosity and inter-pore spacing of porous gas-liquid contacting membranes on the dissolved gas mass transfer have been studied. [18–20] In a previous study by Kreulen et al. [18], the active mass transfer area of non-wetted porous hollow fiber membranes has been reported equal to the total membrane area, regardless of the porosity of the hollow fiber membranes. (Fig. 1.2) At the porous fiber walls, with alternating gas/liquid and solid/liquid interfaces, homogeneous gas saturation condition has been reported and attributed to the extremely small distances between the pores (*i.e.* solid/liquid interfaces) compared to the distance for diffusion to the center of the fiber. [18] These findings highlight the common assumptions in gas-liquid contacting membranes that the porous wall is fully saturated and the liquid phase transport resistance is dominant for non-wetted membranes.

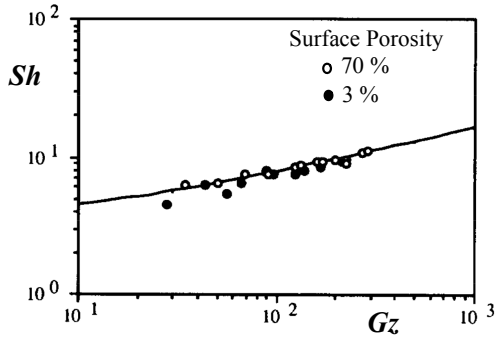

Figure 1.2: Mass transfer correlations of non-wetted porous hollow fiber gas-liquid contacting membranes. The gas absorption data in terms of Sherwood Sh and Graetz number Gz obtained by measurements on 70 % (∘) and 3 % (•) porous fibers in a very good agreement with the analytical solution for a fully saturated no-slip wall (——).

The influence of the hydrodynamics on the gas/liquid contacting performance of the porous hollow fibers has been studied in relation to geometric and operational parameters (fiber diameter d and liquid flow rates, respectively), and the intrinsic liquid properties, diffusivity D and viscosity μ of the liquid. [18] Analogous heat transfer solutions have been employed and dimensionless Graetz type mass transfer correlations have been used to obtain liquid mass transfer coefficients k. (Fig. 1.2) The

Sherwood number (Sherwood number, $Sh = kd/D$) provides a measure of the mass transfer occurring normal to the surface with respect to the diffusivity. The mass transfer in the liquid phase is a function of mass diffusivity and hydrodynamics. The mass transfer correlations are often given as [21]

$$Sh = \frac{kd}{D} = a \cdot Re^b \cdot Sc^c \tag{1.1}$$

where a, b, c are constants, Re is the Reynolds number and Sc is the Schmidt number given as the ratio of momentum (ν) and mass (D) diffusivity. In order to obtain the mass fluxes, the mass transfer coefficients k are estimated from the Sherwood Sh correlations. (Eqn. 1.1) Theoretical derivation of these correlations require the analytical solution of microscopic mass and momentum balances. In membrane based gas-liquid contacting studies, the liquid velocity in the hollow fiber membranes or channels confined by the membranes is often calculated from the Hagen-Poiseuille equation by considering the porous heterogeneous membrane surface as flat and non-slippery. [16–18] Whereas a partial slip boundary condition at porous interfaces have been reported in previous studies on fluid flow at porous media/fluid interfaces. [22–24]

Reduction in hydrodynamic flow resistance is highly desirable in particular when the length scales become smaller. For a fluid flowing in a channel with cross-sectional scale a, the pressure gradient scales with $\Delta P \sim 1/a^4$ for a fixed volume flow rate. [8] For a fluid flow with constant viscosity μ, the same flow rate Q can only be maintained by applying larger ΔP for decreasing length scales, a. However for the same applied ΔP, even larger flow rates can be obtained via hydrodynamic slippage. (Fig. 1.3a) Therefore drag reduction in narrow channels is of great importance and has been investigated intensively for over two decades. [1, 6, 8, 9]

For macroscopic flow systems, the assumption of a non-slippery boundary for viscous fluids flowing along a solid wall has been experimentally validated to be highly accurate, and hence the no-slip boundary condition is commonly used. [9, 10] However recent controlled experiments in the (sub)micrometer range have demonstrated that the no-slip boundary

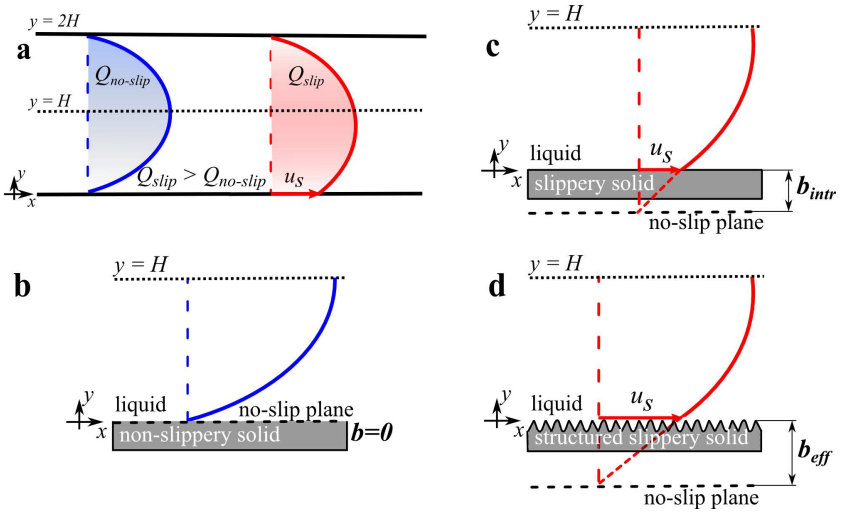

Figure 1.3: A schematic illustration of hydrodynamic slippage. (a) The flow rate (Q) obtained on a slippery surface is larger compared to a non-slippery surface. (b) On a slippery surface, the slip length (b) and wall slip velocity (u_s) is zero. (c) The hydrodynamic slippage on flat hydrophilic/hydrophobic substrates may reveal a small intrinsic slip length (b_{intr}) (d) The hydrodynamic slippage on rough or topographically engineered hydrophobic substrates providing shear free gas-liquid interfaces can give rise to larger effective slip lengths (b_{eff})

condition may not be entirely valid for a Newtonian fluid flowing over solid surfaces. [9, 10] The extent of hydrodynamic slippage is typically expressed in terms of the slip length. The slip length is interpreted as the extrapolated distance below the solid surface where the liquid velocity would equal zero, *i.e.* where the no-slip boundary condition would be satisfied ($b = u_s/\nabla u$). (Fig. 1.3c) [6, 8–10]

Different kinds of substrates with various physicochemical properties have been extensively investigated for hydrodynamic slippage. [9, 25–28, 31] In these previous studies, the slip length has been often categorized based on the physicochemical properties of the substrates. The first is the intrinsic or molecular slip which has often been reported for flat hydrophobic substrates. [9, 10] (Fig. 1.3c) The intrinsic slip lengths so far, are reported to be on the order of nanometers and often regarded as negli-

gible. [9, 10, 25, 26] The second is the apparent slip which has often been attributed to a thin layer of low viscosity film in between the liquid and the solid substrate. [10] The effective slippage reported for micro-patterned (super)hydrophobic substrates suggesting hybrid (liquid-gas and liquid-solid) interfaces [9, 10] is a combination of intrinsic and apparent slippage. (Fig. 1.3d) Effective slip lengths on the order of several micrometers have been obtained using these substrates including (super)hydrophobic microstructures that contain trapped gas bubbles. [27–31]

Various direct and indirect experimental techniques have been employed to measure hydrodynamic slippage. [32, 33] Choi et al. [26] have obtained slip lengths by correlating the applied pressure gradients to the measured flow rates in hydrophilic and hydrophobic channels. Steinberger et al. [34] used a dynamic surface force apparatus on superhydrophobic surfaces with a square lattice of cylindrical holes where the measured force values were correlated to the effective slip length values. Torque measurements using rheometers have also been reported for quantifying slippage on nano-engineered superhydrophobic surfaces. [28] Besides these experimental methods suggesting an indirect quantification of slippage, micro particle image velocimetry (μPIV) has been employed in resolving the flow fields and thereby providing a direct measurement of slip velocity. [9] μPIV has been used in resolving the flows in microchannels with flat hydrophilic, flat hydrophobic and micro-patterned channel walls. [25, 29–31]

Previous studies [31, 35] have shown that the Cassie-Baxter state, where the microstructures are filled with air, promotes slippage at the gas-liquid interfaces established in between the micro-structures. Transitions from Cassie state to Wenzel state [31] and even complete wetting [27] of the microstructures have been reported under convective flow conditions. Such instabilities at the gas-liquid interfaces are related to capillary forces, pressure differences between gas and liquid phases, and to some extent the dissolution of the trapped air into liquid. [9]

1.1.2 Ion Concentration Polarization

Ion concentration polarization (ICP) is a fundamental phenomenon related to diffusion limited charge transport near ion selective boundaries, such as ion exchange membranes, micro/nano-channel junctions, and electrodes.

ICP has been known and observed for ion selective membranes in electrically driven membrane processes such as electrodialysis for a century. [12, 13]

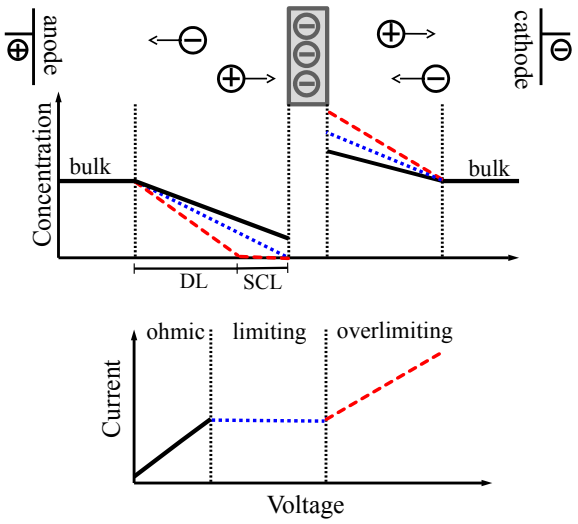

Figure 1.4: Simplified schematic representation of classical electrodialysis. Representative ion concentration profiles and current-voltage response obtained for a cation exchange membrane when a perpendicular electric field is applied. The ion depletion at the anode side and the ion enrichment on the cathode side is depicted for increasing potential difference.

In electrodialysis, the electric current is provided by the migration of counter ions through an ion selective membrane immersed in aqueous electrolyte solutions. [12, 13, 36, 37] The mass transfer of these charged molecules is driven by an electrical potential difference. Once an electric field is applied across an ion selective region (*e.g.* a cation exchange membrane, as illustrated in Fig. 1.4), current increases proportional to the applied voltage. Due to the differences in the rates of transport in the membrane phase and in the adjacent boundary layers, concentration gradients develop at each side of the membrane. The ions deplete on the anode side of the membrane and accumulate at the cathode side. Eventually, the ion concentration, and hence the conductivity vanishes at the anode side of the ion selective boundary (ion depletion, depicted by dotted

line in Fig. 1.4). This implies that an increased voltage will not lead to an increase in ion flux and a diffusion-limited current is reached. Therefore the performance of the separations are bound by this diffusion limited current. However, an overlimiting current (OLC) is observed even at higher electric potentials. [12, 38]

Besides the charged based separations at ion exchange membranes, ICP phenomena has encountered in many processes such as in electrochemical cells at electrode interfaces [39, 40] and in various electrically driven lab-on-chip applications at nanochannel interfaces [36, 41]. The mass transfer of the charged molecules are described by the Nernst-Planck equations and the continuity equation [39, 40, 42]

$$J_i = c_i u - D_i \nabla c_i - D_i z_i \frac{F}{RT} c_i \nabla V \tag{1.2}$$

$$\frac{\partial c_i}{\partial t} = -\nabla \cdot J_i \tag{1.3}$$

where J_i, D_i, c_i, and z_i denote the total flux, diffusion coefficient, concentration, and the charge number of species i, while V, u and t denote the electric potential, the velocity and time, respectively. F, R, and T are the Faraday constant, the gas constant, and the absolute temperature, respectively. Equation 1.2 describes the total ion flux as the summation of convection, Fickian diffusion and electromigration. The electric potential and the ion concentrations are coupled and given by the Poisson equation [39, 40, 42]

$$\nabla \cdot \nabla V = -\frac{F}{\epsilon} \sum_{i=0}^{n} z_i c_i \tag{1.4}$$

where ϵ is the dielectric permittivity. The strongly coupled Poisson-Nernst-Planck (PNP) equations describe the full charge and electric field distribution in electrically driven processes. [38, 42, 43] It is important

to note here that the Poisson equation is not bound to the common electroneutrality assumption ($\sum_{i=0}^{n} z_i c_i = 0$) and can be solved for the space charge density ρ_e ($=\sum_{i=0}^{n} z_i c_i$). (Eqn. 1.4)

The charge and momentum transport are interdependent via the velocity and potential distributions and thereby an accurate full description of all ohmic, limiting and overlimiting conductance (OLC) regimes require the full solution of the coupled sets of equations; the Navier-Stokes equations with the electrical body force terms and the PNP equations (Eqn. 1.2-1.4) [38, 43] In various theory and simulations, the coupled charge and momentum transfer have been studied in ohmic, limiting and also in OLC regimes, which are so far widely in 1D [37, 39, 40, 45, 47] and scarcely 2D. [48, 50] The nonlinear coupled multiphysics and multiscale nature of the ICP phenomena has been reported and described in detail in the recent reports of Bazant et al. [43], Zaltzman and Rubinstein [45], Mani et al. [44], Nikonenko [38], and Chang and Yossifon et al. [46].

Previous theoretical and numerical studies have reported that OLC is associated with an extended ion depletion zone (often described as space-charge layer) [42, 45, 47]. The overlimiting conductance at ion selective interfaces has been discussed to be originated from chemical effects (water splitting, pH variations) and physical effects (electroconvective mixing). [38, 52] Chaotic electrokinetic flows (such as vortices) in OLC regime have been predicted in various theoretical studies. [42, 45–48] The forefront theories describing these secondary chaotic flows at OLC include the electroconvection by electro-osmotic flow, transitions to electro-osmotic nonequilibrium instabilities and surface conduction in various size systems (thin or thick channels) with different charged surfaces (homogeneous or heterogeneous ion exchange membranes, or nanochannels). [45, 46, 48]

The effects of OLC has been reported in various experimental studies on many existing technologies suffering from ICP (*e.g.* electrodialysis, electrodeposition) and on many new lab-on-chip applications working under ICP principle. [38, 43, 57] Few recent experimental studies have focused on the mechanisms and dynamics of ICP induced OLC where the existence of the vortices and their trajectories were investigated by particle tracking methods. [53–56] The experimental progress requires local characterization of charge and momentum transfer near stable and controllable ion selective regions. Developing and implementing such interfaces in mi-

cro scale systems are crucial for acquiring a better understanding of the dynamics of ICP.

Ion Selective Interfaces in Microfluidics

Ion exchange membranes (IEMs) are well-established and widely used in charge based separations. [12, 13] IEMs in microfluidic devices are quite advantageous due to their versatility, robustness and large ion exchange area and capacity. Few recent experimental studies [53, 58, 59] have suggested integrating IEM to micro-devices for charged based separations. In the suggested micro-devices [53, 58, 59], the IEMs are sandwiched in between microchannels. This methodology allows for using well-characterized IEMs such as SPEEK and Nafion in microfluidics. [59] Fluid leakage is often problematic in sandwich type configurations.

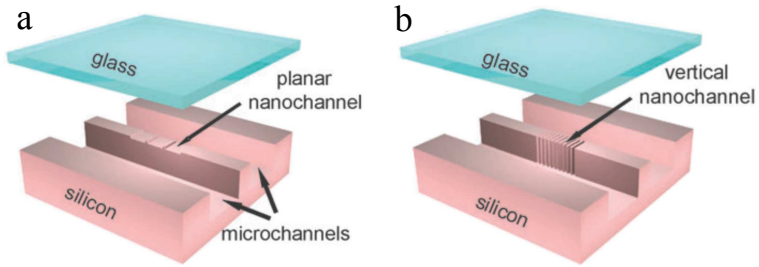

Figure 1.5: Schematic representation of micro and nano channel intersections. (a) A planar configuration of nanochannels where the widths of the nanochannels are micron size and the depths are in nano scale. (b) A vertical configuration of nanochannels where the widths of the nanochannels are in nano scale and the depths are micron size. Illustrations in (a-b) are adopted from [36].

Micro/nano-channel intersections have been employed in various experimental studies aiming at charge based separations. [36, 51, 52] Nanochannels (*i.e.* nanopores) can be ion selective due to the overlapping of electrical double layers of the nanochannel walls at moderate ion concentrations (up to ~ 10 mM). [36, 46, 47] The electrical double layer (*i.e.* the Debye screening length λ_D) is a typical measure of the thickness of the layer shielding the neutral bulk solution from the charged surface. [46] In

nanochannels the electrical double layers occupy the channel resulting in a selective ion exclusion effect. The counter ions of the nanochannel surface charge can permeate through the nanochannels whereas the co-ions are rejected. [36, 46] The nanochannels are often fabricated on typical lab-on-chip substrates such as glass and silicon having negative zeta potential (*i.e.* negative surface charge). Thereby the transport through the micro/nano-channel intersections is limited cationic species.

In the previous experimental studies, two kinds of nanochannel configurations are often encountered; the planar and vertical nanochannels. [36] In the planar configuration (Fig. 1.5a), the channel widths are in micrometer range whereas the depth of the channels are in nanometer range. This configuration allows for easy fabrication. However the ion selective micro/nano-channel intersections are located at one bottom/top edge of the microchannel where the confinement effects are most severe. [36] In the vertical type configuration (Fig. 1.5b), the widths of the nanochannels are in nanometer range, and the depth can be the same as the microchannel depth. The fabrication of such vertical type nanochannels is highly tedious.

1.2 Scope of the Thesis

Within the scope of this thesis, interfacial transport phenomena in microfluidics are investigated, aiming at a better understanding of fluid motion and the associated transport processes driven at interfaces which are commonly encountered in both micro- and macro-scale. The discussion is divided into two primary areas; (i) hydrodynamic slippage and interface driven mass transport near soft gas-liquid interfaces and (ii) ion concentration polarization near charge selective interfaces.

In **Chapter 2**, polymeric porous (super)hydrophobic flat and micro-structured membranes suggesting stable gas-liquid interfaces are presented. The fabricated membranes have been integrated in micro gas-liquid contacting devices. The gas transport in the microchannels confined by the presented porous membranes are investigated both experimentally and numerically. The gas uptake of the liquid in micro-gas-liquid contactors assembled with flat porous hydrophobic membranes and micro-structured porous superhydrophobic membranes are compared.

In **Chapter 3**, the numerical studies of momentum and mass transfer on bubble mattress like geometries, mimicking fictitious porous membranes, are described. The momentum and gas mass transfer in a microchannel with a boundary of alternating solid micro-ridges and gas filled micro-grooves aligned perpendicular to a pressure driven microflow are described. Simulations have been performed to investigate the influence of gas-liquid interface geometry on the hydrodynamic slippage and the coupled interfacial mass transfer of gas into liquid at equilibrium saturation conditions.

In **Chapter 4**, novel superhydrophobic microfluidic devices that allow the presence of stable and controllable microbubbles at the boundary of the microchannels are presented. The effect of micro-bubble geometry on the hydrodynamic slippage is examined experimentally and numerically at high resolution. The first experimental results of the effective slip lengths and the friction factors are revealed for a range of protrusion angles θ of the micro-bubbles into the flow using a micro-particle image velocimetry technique.

In **Chapter 5**, gas absorption studies at stable micro-bubble surfaces aligned perpendicular to a pressure driven laminar flow are provided. Interfacial mass transfer of gas has been studied for short contacting times. In situ local concentration gradients of dissolved gas are obtained by fluorescent life time imaging microscopy measurements. The interfacial mass transfer of dissolved gas are analyzed numerically considering (i) equilibrium saturation conditions and (ii) non-equilibrium conditions at the bubble surfaces.

In **Chapter 6**, the fabrication of hydrogel based ion exchange membranes in microchannels by selective photo-induced polymerization and crosslinking methods are presented. To control the charge and volume properties of the presented charge selective hydrogels, the chemistry of the membranes was tailored. Passive and active ion transport near the in-situ prepared microfluidic membranes are studied without applied potential and with applied DC potential across the membrane, respectively.

In **Chapter 7**, a summary of the presented microfluidic studies of interfacial transport is provided. The obtained results are evaluated with the concluding remarks and the gained key insights of interface driven transport at micro scale that can be essential for micro- or macro- scale

applications aiming at amplifying the transport driven at the interfaces. In the subsequent outlook, firstly some promising future perspectives for gas/liquid contacting in microfluidics are elaborated. Secondly, some critical aspects for ion concentration polarization induced electrohydrodynamics are discussed. Micro/nano-fluidic devices are presented including microchannels connected by an array of nanochannels. Preliminary findings on the ion concentration polarization induced electrokinetic instabilities are discussed, providing a promising outlook on the associated ion transport.

Bibliography

[1] Stone HA, Stroock AD, Ajdari A (2004) Engineering Flows in Small Devices: Microfluidics Toward a Lab-on-a-Chip. *Annu. Rev. Fluid Mech.* 36:381-411.

[2] Nguyen N-T, Wereley ST (2002) *Fundamentals and Applications of Microfluidics*, (Artech House, Norwood).

[3] Whitesides GM (2006) The origins and the future of microfluidics. *Nature* 442:368-373.

[4] Stone HA, Kim S (2001) Microfluidics: Basic Issues, Applications, and Challenges. *AIChE* 47(6):1250-1254.

[5] Andersson H, van den Berg A (2003) Microfluidic devices for cellomics: a review. *Sens. and Actuat. B* 92:315-325.

[6] Bruus H (2006) *Theoretical microfluidics*, (Lecture notes third edition).

[7] Schoch RB, Han J, Renaud P (2008) Transport phenomena in nanofluidics. *Rev. Modern Phys.* 80:839-883.

[8] Davis AMJ, Lauga E (2009) Geometric transition in friction for flow over a bubble mattress. *Phys. Fluids* 21:011701.

[9] Rothstein JP (2010) Slip on superhydrophobic surfaces. *Annu. Rev. Fluid Mech.* 42:89-109.

[10] Lauga E, Brenner MP, Stone HA (2007) in *Handbook of Experimental Fluid Dynamics*, eds Tropea C, Yarin A, Foss JF (Springer, New York), chap.19.

[11] Das DB, Hanspal NS, Nassehi V (2005) Analysis of hydrodynamic conditions in adjacent free and heterogeneous porous flow domains *Hydrol. Process.* 19:2775-2799.

[12] Mulder M (1996) *Basic principles of membrane technology.* (Second edition, Kluwer Academic Publishers).

[13] Mulder M (2004) *Membrane technology and applications* (Second edition, John Wiley & Sons Ltd.).

[14] Noble RD, Stern SA (1995) *Membrane Separations Technology: Principles and Applications, Ch 10; Membrane Contactors*, (Elsevier Science BV, Amsterdam).

[15] Ho WSW, Sirkar KK (1992) *Membrane Handbook, Volume 1, Ch. 46*, (Chapman and Hall).

[16] Mavroudi M, Kaldis SP, Sakellaropoulos GP (2006) A study of mass transfer resistance in membrane gas-liquid contacting processes. *J. Mem. Sci.* 272(1-2):103-115.

[17] Zhang HY, Wang R, Liang DT, Tay JH (2008) Theoretical and experimental studies of membrane wetting in the membrane gas-liquid contacting process for CO_2 absorption. *J. Mem. Sci.* 308(1-2):162-170.

[18] Kreulen H, Smolders CA, Versteeg GF, van Swaaij WPM (1993) Microporous hollow fibre membrane modules as gas-liquid contactors. Part 1. Physical mass transfer processes. *J. Mem. Sci.* 78:197-216.

[19] Keller HK, Stein TR (1967) A two-dimensional analysis of porous membrane transport. *Math. Biosci.* 1:421-437.

[20] Juhasz NM, Deen WM (1991) Effect of local Peclet number on mass transfer to a heterogeneous surface. *Ind. & Eng. Chem. Research* 30:556-562.

[21] Bergman TL, Lavina AS, Incropera FP, Dewitt DP (2007) *Fundamentals of Heat and Mass Transfer* (Seventh edition, John Willey & Sons).

[22] Beavers GS, Sparrow EM, Magnuson RA (1970) Experiments on coupled parallel flows in a channel and a bounding porous medium. *J. Basic Eng.* 92(4):843-848.

[23] Chellam S, Wiesner MR, Dawson C (1992) Slip at a uniformly porous boundary: effect on fluid flow and mass transfer. *J. Eng. Math.* 26(4):481-492.

[24] Ramon G, Agnon Y, Dosoretz C (2009) Heat transfer in vacuum membrane distillation: Effect of velocity slip. *J. Mem. Sci* 331:117-125.

[25] Tretheway DC, Meinhart CD (2002) Apparent fluid slip at hydrophobic microchannel walls. *Phys. Fluids* 14(3):L9.

[26] Choi C-H, Westin KJA, Kenneth SB (2003) Apparent slip flows in hydrophilic and hydrophobic microchannels. *Phys. Fluids* 15(10):2897-2902.

[27] Byun D, Kim J, Ko HS, Park HC (2008) Direct measurement of slip flows in superhydrophobic microchannels with transverse grooves. *Phys. Fluids* 20:113601.

[28] Choi C-H, Kim CJ (2006) Large slip of aqueous liquid flow over a nanoengineered superhydrophobic surface. *Phys. Rev. Lett.* 96(6):066001.

[29] Ou J, Perot B, Rothstein JP (2004) Laminar drag reduction in microchannels using ultrahydrophobic surfaces. *Phys. Fluids* 16(12):4635-4643.

[30] Ou J, Rothstein JP (2005) Direct velocity measurements of the flow past drag-reducing ultrahydrophobic surfaces. *Phys. Fluids* 17:103606.

[31] Tsai P, et al. (2009) Quantifying effective slip length over micropatterned hydrophobic surfaces. *Phys. Fluids* 21:112002.

[32] Chiara N et al. (2005) Boundary slip in Newtonian liquids: a review of experimental studies. *Reports on Prog. in Phys.* 68(12):2859.

[33] Bouzigues CI et al. (2008) Using surface force apparatus, diffusion and velocimetry to measure slip lengths. *Philos. Trans. of Roy. Soc. A: Math. Phys. & Eng. Sci.* 366(1869):1455-1468.

[34] Steinberger A, Cottin-Bizonne C, Kleimann P, Charlaix E (2007) High firction on a bubble mattress. *Nature Mater.* 6:665-668.

[35] Bhushan B, Jung YC (2007) Wetting study of patterned surfaces for superhydrophobicity. *Ultramicroscopy* 107(10-11):1033-1041.

[36] Kim SJ, Song YA, Han J (2010) Nanofluidic concentration devices for biomolecules utilizing ion concentration polarization: theory, fabrication, and applications. *Chem. Soc. Rev.* 39(3):912-922.

[37] Mishchuk N (2010) Concentration polarization of interface and nonlinear electrokinetic phenomena. *Adv. Coll. Int. Sci.* 160:16-39.

[38] Nikonenko VV *et al.* (2010) Intensive current transfer in membrane systems: Modelling, mechanisms and application in electrodialysis. *Adv. Coll. Int. Sci.* 160:101-123.

[39] Van Soestbergen M, Biesheuvel PM, Bazant MZ (2010) Diffuse-charge effects on the transient response of electrochemical cells. *Phys. Rev. E* 81:021503.

[40] Murphy WD, Manzanares JA, Mafe S, Reiss H (1992) A numerical study of the equilibrium and nonequilibrium diffuse double layer in electrochemical cells. *J. Phys. Chem.* 96:9983-9991.

[41] Wang YC, Han J (2008) Pre-binding dynamic range and sensitivity enhancement for immuno-sensors using nanofluidic preconcentrator. *Lab Chip* 8:392-394.

[42] Rubinstein I, Zaltzman B (2010) Extended space charge in concentration polarization. *Adv. Coll. Int. Sci.* 159(2):117.

[43] Bazant M, Kilic MS, Storey BD, Ajdari A (2009) Towards an understanding of induced-charge electrokinetics at large applied voltages in concentrated solutions. *Adv. Coll. Int. Sci.* 152:48-88.

[44] Mani A, Bazant M (2011) Deionization shocks in microstructures. *Phys. Rev. E* 84:061504.

[45] Zaltzman B, Rubinstein I (2007) Electro-osmotic slip and electroconvective instability. *J. Fluid Mech.* 579(1):173-226.

[46] Chang HC, Yossifon G, Demekhin EA (2012) Nanoscale electrokinetics and microvortices: How microhydrodynamics affects nanofluidic ion flux. *Annu. Rev. Fluid Mech.* 44:421-426.

[47] Yossifon G, Chang HC (2008) Selection of Nonequilibrium Overlimiting Currents: Universal Depletion Layer Formation Dynamics and Vortex Instability. *Phys. Rev. Lett* 101:254501.

[48] Dydek EV, Zaltzman B, Rubinstein I, Deng DS, Mani A, Bazant, M (2011) Overlimiting current in a microchannel. *PRL* 107:118301.

[49] Pham VS, Li Z, Lim KM, White JK, Han J (2012) Direct numerical simulation of electroconvective instability and hysteretic current-voltage response of a permselective membrane. *Phys. Rev. E* 86:046310.

[50] Belashova ED *et al.* (2012) Overlimiting mass transfer through cation-exchange membranes modified by Nafion film and carbon nanotubes. *Electrochim. Acta* 59:412-423.

[51] Höltzel A, Tallarek U (2007) Ionic conductance of nanopores in microscale analysis systems: Where microfluidics meets nanofluidics. *J. Sep. Sci.* 30(10):1398-1419.

[52] Zangle TA, Mani A, Santiago JG (2010) Theory and experiments of concentration polarization and ion focusing at microchannel and nanochannel interfaces. *Chem. Soc. Rev.* 39(3):1014-1035.

[53] Kwak R, Pham VS, Lim KM, Han J (2013) Shear Flow of an Electrically Charged Fluid by Ion Concentration Polarization: Scaling

Laws for Electroconvective Vortices. *Phys. Rev. Lett.* 110(11):114501-114506.

[54] Rubinstein SM, Manukyan G, Staicu A, Rubinstein I, Zaltzman B, Lammertink RGH, Mugele F, Wessling M (2008) Direct observation of a nonequilibrium electro-osmotic instability. *PRL* 101(23):236101.

[55] Kim SJ, Wang YC, Lee JH, Jang H, Han J (2007) Concentration polarization and nonlinear electrokinetic flow near a nanofluidic channel. *Phys. Rev. Lett* 99:044501.

[56] Yossifon G, Chang HC (2010) Changing nanoslot ion flux with a dynamic nanocolloid ion-selective filter: Secondary overlimiting currents due to nanocolloid-nanoslot interaction. *Phys. Rev. E* 81:066317.

[57] Balster JH (2006) *Membrane module and process development for monopolar and bipolar electrodialysis*, (PhD thesis, TNW-MTG, University of Twente).

[58] Park SC, Taek D, Kim HC (2009) Ion bridges in microfluidic systems. *Microfluidics nanofluidics* 6(3):315-331.

[59] Kwak R, Guan G, Peng WK, Han J (2012) Microscale electrodialysis: Concentration profiling and vortex visualization. *Desalination* 308:138-146.

2

Oxygenation by a superhydrophobic slip G/L contactor

The compelling need for efficient supply of gases into liquids or degassing of fluids within confined microchannels triggered this study on membrane assisted microchemical systems. Porous, hydrophobic, flat and micro-structured polyvinylidene fluoride (PVDF) membranes are fabricated and integrated to a glass G/L contacting microfluidic device with the aid of optical adhesives. The oxygen transport in microchannels, driven by convection and diffusion, is investigated both experimentally and numerically. The effects of intrinsic membrane morphology on the G/L contacting performance of the resultant membranes are studied. Experimental results obtained for the flat membranes are in a good agreement with the simulations performed with the assumptions of negligible gas phase and membrane mass transfer limitations. Micro-structured membranes revealed promoted apparent slippage and enhanced mass transport rates, exceeding the experimental performance of the flat membranes.

This chapter is based on the publication Karatay E, Lammertink RGH (2012) *Lab on a Chip*, 12:2922-2929.

2.1 Introduction

Gassing/degassing of fluids has dozens of applications in (bio)chemical engineering area for both reacting and non-reacting processes. Instead of employing conventional, direct contacting equipments, such as venturi injectors, wet scrubbers, distillation columns, and falling film wall reactors, utilization of membranes for contacting has various advantages. These include high interfacial area, hydrodynamic decoupling of different phases, and reduced mass transfer resistance. [1–3] Membrane contactors make important contributions to several useful process intensification methods: membrane reactors, absorbers, and degassers.

Porous, hydrophobic gas liquid (G/L) contacting membranes have been attracting increasing attention and have numerous applications in the removal of acidic gases, such as CO_2 [2–4], H_2S [5, 6], or NO_x from exhaust gases [7], ammonia removal from water [8], carbonation of soft drinks, and blood oxygenation (artificial lungs) [9, 10], as well as in heterogeneously catalyzed gas-liquid reactions due to the intense contact of G/L/S phases reducing the mass transfer limitations, separating gaseous and liquid reactants, and hence resulting in higher selectivities at higher conversions. [11, 12]

As reported elsewhere [12–16], the unique properties of microsystems deriving from their high surface to volume ratio, short molecular diffusion distance, easy scale up, highly reduced waste, precise control parameters, and the opportunity to integrate unit operations on these micro-scale devices are among the reasons for striking growth in research on microchemical systems. Since the early 2000s, there is an increasing tendency to utilize membranes for the integration of separation and reaction functionalities to the micro-devices. [10, 12–22] Noticeably, PDMS, being an optical transparent, rubbery polymer enabling gas permeation, flexibility, and easy integration to microdevices, is used as a membrane material in many fields. These include analytical, organometallic chemistry, and biology for G/L contacting purposes, specifically, for the delivery of controlled amounts of oxygen in tissue engineering applications [18–22], as well as in G/L phase photosynthesized oxygenations [13], and partial oxidation reactions. [12, 17] These recent studies, highlighting the compelling need to ensure efficient supply of gases into confined liquids in a controlled man-

ner with high accuracy, reveal the room for investigating new polymeric materials in membrane-integrated-microfluidics.

The advent of micro/nano-fluidics has motivated the great interest in interfacially driven transport in tiny channels where the bulk fluid motion is realized by convection. Because of the increasing hydrodynamic resistances with decreasing channel sizes, avenues for efficient fluid flow at such scales can be addressed. Pressure-driven flow can be enhanced by surfaces allowing hydrodynamic slippage of the fluid on the solid, amplifying the interfacially driven transport phenomena as well. Recent studies concluded that with a smooth hydrophobic surface, one can reach slip lengths not more than a few ten nanometers unless the assessment of surface roughness or topographic structures that are specifically engineered. [44] The existence of slip velocity on a porous surface has been verified. [45, 46] The slippage on porous materials is connected with the additional G/L interface of relevance to the gas injection/suction at the porous wall. These considerations imply the potential of new porous materials, which can be fabricated and topographically structured with simple methods, in microfluidics. These porous materials can significantly contribute to hydrodynamic slippage and hence to the improvement of interfacial phenomena, including gas transport to or from the confined microchannels.

PVDF is a very promising membrane contactor material due to its hydrophobicity and excellent chemical resistance, particularly towards oxidation. Its solubility in organic solvents allow ease of fabrication compared to other hydrophobic polymers such as polypropylene (PP), polyethylene (PE) and polytetrafluoroethylene (PTFE). Porous PVDF membranes are frequently used in membrane science for numerous applications [2–8], and in establishing intimate contact of G/L/S interfaces for heterogeneously catalyzed multi-phase reactions. [11] PVDF is also of interest in Bio-MEMS, for sensing and actuation applications due to its biocompatibility, and stable piezoelectric, impedance properties. [23, 24] The superior characteristics of PVDF make it prone to a broad range of new applications in microchemical systems.

In the field of microfluidics, direct bonding such as, anodic bonding, plasma bonding, fusion bonding is widely used. However, the applicability of these methods is limited by the type of material from which the chip components are produced. It can be limited by harsh conditions; high

temperature, oxidative plasma, high voltage, that can be destructive for the characteristic properties of the chip components. These considerations become more critical when one of the chip components is polymeric. Apart from direct methods, bonding techniques by means of gluing two components of the chip were reported to be effective at milder conditions. [25–27] A wide range of materials ; epoxy glue [28], Hysol [29], SU-8 [30], parylene [31], polyimide [25], PDMS [32], and UV-curable adhesives [27] were among the materials applied as an intermediate adhesive layer for bonding LOC substrates.

In the present study, porous, micro-structured, superhydrophobic PVDF membranes are integrated to fluidic glass chips by means of UV curable adhesives. Mass transfer efficiency of the proposed microdevice is tested by oxygen saturation experiments. The experimental results are verified by numerical modeling.

2.2 Experimental

2.2.1 Glass Chips

Meander microchannels for liquid flow, and micro-reservoir for gas flow are fabricated by standard photolithography followed by chemical (HF) wet etching on separate borofloat glass wafers. The wafers are diced to obtain the glass chips having dimensions of 2 cm x 1.5 cm. The channel width, and the channel height of the meandering channels are varied in the range of 300-500 μm, and 50-100 μm, respectively. The length of the microchannels are 13.5 cm. The micro-reservoirs for gas flow have the dimensions of 1.2 cm x 1.5 cm with a depth of 50 μm.

2.2.2 Membranes

PVDF membranes were prepared by immersion precipitation method [33]. 20 wt% PVDF (Solvay, Solef) is dissolved in dimethyl acetamide (DMAc, Merck) by magnetic stirring at 65^{o}C overnight. The polymer solution was cast at a thickness of 600 μm on a silicon wafer by an automatic film applicator. The polymeric films were phase separated in three different non-solvents; water, ethanol, and water/ethanol (50/50 v%) mixture.

The polymeric film was placed in the coagulation medium for 2 hours, after which the coagulation bath was replaced with the fresh non-solvent. The film was kept in this coagulation medium for 24 hours. The collapse of the pores were prevented by gradually replacing the aqueous based non-solvent by a non-solvent having a lower surface tension. The film was put in three consecutive ethanol (Assink Chemie) baths, followed by three consecutive n-hexane (Merck) baths. After the films were dried, they were kept in a vacuum oven at 30^oC. Micro-structured PVDF membranes including pillars with a diameter of 10 μm and an aspect ratio in the range of 1-4 were prepared by phase separation micro molding. [38] Wafers including microholes having a diameter of 10 μm, and separation distance of 10 μm with depths of approximately 13 μm and 35 μm were prepared by SU-8 patterning. The polymer solution was cast on these wafers, and hence the replica of the micro-structure pattern was obtained on the membranes. The morphology of the fabricated membranes were characterized by SEM (JEOL JSM 5600LV). Apparent porosity measurements were done with a pycnometer (Micromeritics, Accupyc 1330). N_2 permeance experiments were performed using capillary flow porometer (Porolux-1000) at 1 bar. Hydrophobicity of the membranes were tested by contact angle measurements (Dataphysics, OCA 20). The membranes were further characterized by clean water breakthrough pressure experiments. Flat, dense PDMS membranes with thicknesses of 100 μm were prepared by casting a prepolymer (Permacol B. V., RTV-A) and crosslinking agent (Permacol B. V., RTV-B) solution on a silicone wafer, followed by curing for one day at 60^oC. The ratio of prepolymer to crosslinking agent was 10:1, and the mixture was degassed before casting.

2.2.3 Chip Assembly

UV-curable adhesives were employed to bond porous, hydrophobic PVDF membranes to glass substrates. Among various different types available in the market, a fine selection was done for the specific polymer substrate of interest considering the viscosity, composition, and the solvents used in the formulation of the glue which affect the adhesion due to the hydrophobic nature of the membranes. NOA 78 (Norland Optical Adhesive), revealing a satisfactory adhesion, was selected as the gluing material between glass and PVDF membranes. The methodology reported by Arayanarakool et

al. [27] was employed. The glass chips to be bonded were cleaned by O_2 plasma (Harrick Plasma) for 10 minutes before bonding. The optical adhesive was spin coated on a blank glass plate at 2000 rpm for 90 seconds. A thin layer of this uncured glue was transferred to the structured glass substrates (including the meander channels and the gas sink) by means of a roller. Once the uncured glue was conveyed to the glass chips, the membrane is aligned such that the effective G/L contacting spots are not contaminated with the adhesive. Once the glass-membrane-glass assembly was cured by UV exposure for 10 minutes, it was inserted into a custom made chip holder, as shown in Figure 2.1a.

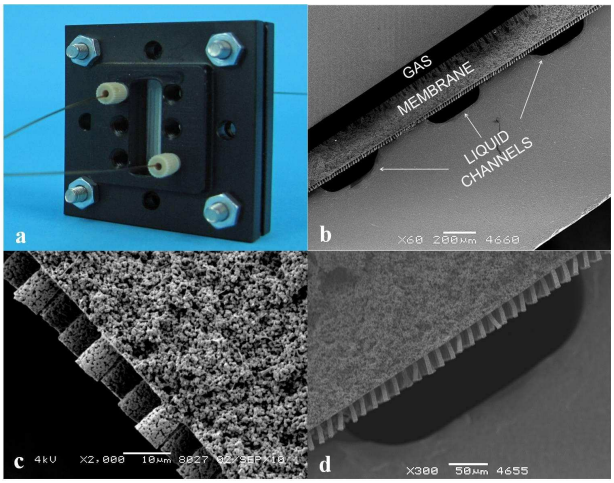

Figure 2.1: PVDF membrane integrated G/L contacting micro-device. (a) Optical image of PVDF membrane integrated micro-device with fluidic connections. (b) Cross sectional SEM image of gas sink-micro-structured membrane-liquid microchannels assembly at a magnification of 60X (c) Cross sectional SEM image of a microstructured membrane with short pillars. (d) Cross sectional SEM image of gas sink-micro-structured membrane-liquid microchannels assembly at a higher magnification of 300X.

2.2.4 Experiments and Set-up

A syringe pump (HARVARD Apparatus PHD 2000) was used to control the flow rate of liquid in the glass microchannels. Deoxygenated water is

used as liquid feed. Pure oxygen is fed to the micro-reservoir from the opposite side of the assembly. For the oxygen flow through the gas sink, either the flow rate of the gas (1 ml/min) was controlled by a mass flow controller (BRONKHORST, El-Flow) or the pressure of the gas (0-2 bar) was controlled by a pressure reducer. In the multilayer glass-membrane-glass assembly, the gas diffuses through the membrane to the liquid channel. The dissolved oxygen content of the outlet liquid was measured by a fiber optic oxygen sensor (FIBOX 3, PreSens). The experimental dissolved oxygen concentration data was recorded. The liquid flow rate was varied in the range of 25 μl/min to 2 ml/min while the gas flow rate and/or pressure was kept constant during the experiments.

2.3 Numerical Analysis

The oxygen concentration profile evolution in the microchannels is numerically studied. 2D and 3D models were solved by finite element methods (COMSOL Multiphysics v4.1). Subdomain mesh consisted of 1936, and 1314593 elements for 2D, and 3D cases respectively. In 3D simulations, the geometry of the meander channels structured on home-made glass chips was used as the computational domain. Whereas a simplified straight channel geometry was used in 2D analysis. Navier-Stokes equation for hydrodynamics is coupled with convection-diffusion equation for the mass transport and solved for the liquid side with an assumption of non-wetted membrane pores, hence neglecting mass transfer resistance across the porous membrane. Assuming the G/L interface is established at the liquid side of the membrane, the interface oxygen concentration (C_i) can be related to the partial pressure (P_i) of the gas at the interface by Henry's law

$$c_i = \frac{P_i}{H} \tag{2.1}$$

where $H = 7.67 \times 10^7 Pa.l/mol$ [39] is Henry's coefficient for O_2 in water. With physical adsorption at these conditions and a constant interface

concentration at the porous PVDF membrane boundary of the liquid side microchannels, mass transfer can be described by

$$u_y(x)\frac{\partial c}{\partial y} = D\frac{\partial^2 c}{\partial x^2} \tag{2.2}$$

where D is the oxygen diffusion coefficient in water ($D = 1.97 \times 10^{-9} m^2/s$) [39] and $u_y(x)$ is the velocity of the longitudinal bulk flow. The inlet boundary condition to the microchannel was ascribed to be zero. In three dimensional analysis, Navier-Stokes equation was numerically solved. In two dimensional analysis, the Hagen-Poiseulle slit analog velocity profile was imposed (Eqn. 2.3). A schematic illustration of 2D model geometry and the mass transfer boundary conditions are represented in Figure 2.2c.

$$u_y(x) = 4u_{max}\frac{x}{B}(1 - \frac{x}{B}) \tag{2.3}$$

The average O_2 concentration at the outlet of liquid side microchannel was determined by boundary integration over the normal outflow;

$$< c > = \frac{\int c u_y(x) dx}{\int u_y(x) dx} \tag{2.4}$$

Numerical analysis is also performed for oxygenation using a PDMS membrane, including the thickness of the dense PDMS membrane, for comparison purposes. Additional mass transfer resistance offered by the gas diffusion across the PDMS membrane and the applied boundary conditions are described in Eqns. 2.5a-2.5c.

$$D_m\frac{\partial^2 c_m}{\partial x^2} = 0 \tag{2.5a}$$

$$x = -L, \qquad c_m = c_{m,0} \tag{2.5b}$$

$$x = 0, \qquad D_m\frac{\partial c_m}{\partial x} = \dot{N}_{O_2}^{water} \tag{2.5c}$$

C_m is the concentration of oxygen in the membrane phase. $C_{m,0}$ is the adsorbed oxygen concentration at $x = -L$, where PDMS membrane contacts pure oxygen gas phase at 1 bar and 25^{o}C. $C_{m,0}$ is expressed in terms of oxygen partition coefficient in PDMS ($K_g = 0.3$) and concentration of oxygen in the gas phase ($C_{g,b} = 40$ mol/m^3) to be $K_g C_{g,b}$. Similarly, $C_{m,L}$, the desorped oxygen concentration at $x = 0$, where PDMS membrane contacts water flow in the microchannel, is expressed in terms of oxygen partition coefficient in water ($K_w = 10$) and local concentration of oxygen in the liquid phase (C) to be $K_w C$. The oxygen flux across the PDMS slab equals the oxygen flux to water ($\dot{N}_{O_2}^{water}$) at $x = 0$, and Eqn. 2.5c becomes

$$x = 0, \qquad D_m \frac{K_g c_{g,b} - K_w c}{L} = \dot{N}_{O_2}^{water} \tag{2.6}$$

For the liquid phase, Hagen-Poiseulle slit analog velocity profile (Eqn. 2.3) is used for longitudinal bulk flow, and the differential mass balance describing the oxygen concentration profile in the liquid (Eqn. 2.2) is numerically solved using the flux boundary condition represented in Eqn. 2.6. A schematic illustration of 2D model geometry including the PDMS membrane and the corresponding mass transfer boundary conditions are represented in Figure 2.2b.

2.4 Results and Discussion

2.4.1 Numerical Simulations

2D and 3D models governing the momentum and mass transfer in the liquid channels were solved with the assumptions of no slip conditions at the channel boundaries and equilibrium O_2 saturation condition at the membrane boundary. The mass transfer resistance across the porous membrane was ignored. Figure 2.2a represents the 3D model geometry and the steady state dissolved oxygen concentration profile in a meander microchannel. Here the width and height of the microchannel is 500 μm and

100 μm, respectively. The water flow rate is 250 μl/min corresponding to the Reynolds number of 10.6. As the surface plot illustrates, deoxygenated water is saturated along the channel as O_2 diffuses from the membrane to the water. The bottom surface boundary is prescribed to the solubility value of pure oxygen in water at 273 K and 1 bar (1.32 mol/m^3).

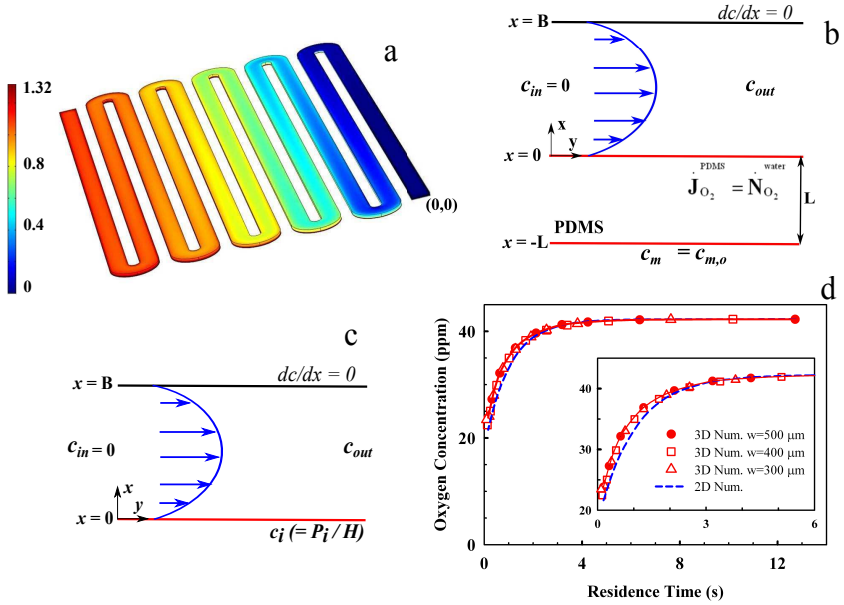

Figure 2.2: 2D and 3D numerical simulations. (a) 3D surface plot of oxygen concentration profile in a 500 μm wide and 100 μm deep meander microchannel. (b) Illustration of 2D numerical model settings regarding assemblies with PDMS membranes. (c) Illustration of 2D numerical model settings regarding assemblies with porous PVDF membranes. (d) The effect varying microchannel widths for 3D simulations and the comparison of 2D and 3D simulation results of the average outlet oxygen concentrations with respect to varying liquid residence times.

The mass transfer behavior of the liquid side for varying channel widths in the range of 300-500 μm are investigated and compared with 2D simulations for different liquid residence times. (Fig. 2.2d) The residence time of the liquid in the microchannel is calculated from the ratio of channel volume to flow rate. The volumes of 300, 400, and 500 μm wide channels are 3.2, 4.2 and 5.3 μl, respectively. As Figure 2.2d presents, the O_2 trans-

port is hardly influenced by the width of the liquid channel in this range. Furthermore, the two dimensional analysis, equivalent to a parallel plate configuration, agrees well with the three dimensional analysis. The slight deviations at higher flow rates can be attributed to the so-called race track affect at the corner of the meandering channels in 3D geometry.

The numerical results presented should show the fastest oxygen saturation possible, since the mass transfer limitations on the gas side and on the membrane side are neglected. Only the mass transfer limitation in liquid phase is taken into account as the G/L interface is situated at the liquid side of the membrane. Besides, equilibrium conditions are considered and the interface dissolved oxygen concentration is described by Henry's Law at G/L interfaces.

2.4.2 Membrane Morphology

Immersion precipitation is a phase separation process which includes the exchange of the solvent in the thin polymer film by the non-solvent in the coagulation bath. 20 wt % PVDF/ DMAc films were phase separated in three different coagulation mediums; water (M2), ethanol (M3), and water/ethanol (50/50 v%) (M1). The apparent porosity values of the prepared membranes, tabulated in Table 2.1, are comparable to a commercially available, hydrophobic membrane (Accurel PP 2E HF, MEMBRANA). The N_2 permeance results and breakthrough pressure values of these membranes are also tabulated in Table 2.1. As the gas permeation and breakthrough pressure values indicate, the coagulation medium, in which the membrane was formed, influences the internal membrane structure. The membrane phase separated in water (M2) revealed 100 times less permeance compared to the membrane phase separated in ethanol (M3), although the apparent porosity values of these membranes are approximately the same. The membrane phase separated in water/ethanol mixture (M1) has a N_2 permeance value in between M2 and M3, comparable to the commercial membrane.

These findings indicate the effect of coagulation medium on the surface porosity of the prepared membranes, as different non-solvents alter the rate of polymer precipitation. Similar to the permeance experiments, the

Table 2.1: Internal characteristics of home made membranes in comparison to commercial membrane

Membrane	Porosity(%)	N_2 Permeance(GPU [a])	P_b(bar)
Accurel	80	3.68×10^5	2.2
M1[b]	75	5.36×10^5	2.6
M2[c]	75	0.17×10^5	3.5
M3[d]	77	13.1×10^5	1.1

[a] 1GPU = $10^{-6} cm^3/cm^{-2}s^{-1}cmHg^{-1}$

[b] Phase separated in water/ethanol (50/50 v%)

[c] Phase separated in water

[d] Phase separated in ethanol

breakthrough pressure values of the prepared membranes are in agreement with the order of increasing effective porosity, M3 > M1 > M2.

In micro scale systems, porous materials have numerous benefits. In particular for gassing/degassing applications, where an additional layer is used to decouple the gas and liquid flow. Porosity can play a significant role, determining the mass transfer rate limiting step. The use of PDMS, being a highly permeable material to gases and vapors, has been acknowledged in bio-microfluidics by several authors [18–22]. The gases permeate by solution-diffusion mechanism in the dense PDMS films. The gaseous oxygen molecules incorporates in the PDMS membrane by preferential sorption. The adsorped oxygen diffuses across the PDMS film, and desorped at the other side, partitioning in water phase. This mode of oxygen transport across the membrane offers an additional mass transfer resistance proportional to film thickness. Using the literature N_2 permeability value [40], the N_2 permeance of a PDMS film with a thickness of 100 μm can be calculated to be 2.8 GPU, which is 5 orders of magnitude smaller than the N_2 permeance values of the porous PVDF membranes presented in Table 2.1. The pore sizes of the presented membranes are larger than the mean free path of the gas molecules, hence the transport limitation is negligible compared to dense membranes. In addition to mass transfer resistance, non-porous membranes show a selectivity over different gases. The O_2/N_2, and CO_2/N_2 selectivity values for PDMS are reported

to be 2 and 12, respectively. [40] Therefore, the transport rate of these gases through PDMS films are different, which could be critical for the applications in cell culture environments or Bio-MEMS related sensors and actuators where the exchange rate of those gases can be essential. Utilization of porous membranes in gas liquid contactors eliminates the size/affinity discrimination of the permeating gas molecules.

Table 2.2 presents the results of dynamic contact angle measurements. A flat porous PVDF membrane was pressed at 50^oC with 2 tones in a Hydraulic Press (Specac) to obtain a dense PVDF film (M0). The advancing contact angle of this smooth and dense PVDF film is measured to be 83^o ± 2^o, with a large hysteresis of 23. The flat, phase separated membrane (M1) showed an increased advancing contact angle, with a smaller hysteresis value due to the surface roughness induced by the internal pores. Contact angle values of micro-structured membranes M4, PVDF membranes with short pillars (Figure 2.1c), and M5, PVDF membranes with tall pillars (Figure 2.1d), were further improved to values above 160^o, with considerably diminished hysteresis. These observations are indicative of Cassie-Baxter state of topographically engineered M4 & M5 membranes. In this state, the liquid rests on the tops of micro-structures.

Table 2.2: Contact angle measurements of flat/micro-structured membranes phase separated in water/ethanol (50/50 v%) in comparison to dense PVDF film

Membrane	Advancing CA (^{o})	Receding CA (^{o})	Hysteresis
M0[a]	83	57	26
M1[b]	159	146	13
M4[c]	165	158	7
M5[d]	164	158	6

[a] Dense PVDF film

[b] Flat PVDF membrane

[c] PVDF membrane with short pillars

[d] PVDF membrane with tall pillars

Hydrophobic materials can prevent wetting and thereby can be used in minimizing the mass transfer limitations. Due to the hydrophobic nature

of PVDF polymers and the surface roughness obtained by the phase separation technique, M1 membranes reveal an improved hydrophobicity. The micro-structured membranes (M4 & M5) show superhydrophobic behavior due to the combination of surface roughness induced by the porosity and by the micro-pillars. These findings are in agreement with previous studies investigated composite G/L/S interfaces on micro-patterned surfaces [41–43] and imply the possibility of achieving Cassie-Baxter state on the prepared micro-structured membranes.

2.4.3 Gas Transport

The oxygen contacting performance of the porous, flat/micro-structured, hydrophobic/superhydrophobic PVDF membranes was tested. Oxygen diffuses across the membrane and G/L interfaces are established at the membrane boundary of the liquid channel. Dissolved oxygen evolving from the membrane boundary is convectively transported by the initially deoxygenated water flowing along the channel.

Figure 2.3a shows the influence of liquid flow rate on the oxygen uptake for different membranes in comparison to simulation results. For all of the membranes presented, larger residence times and hence lower water flow rates lead to higher outlet oxygen concentrations. The numerical results reveal that the oxygen concentration varies abruptly in the first 2 seconds and the channel (500 μm wide, 100 μm deep) is fully saturated within utmost 3 seconds. Home-made PVDF membranes phase separated in water/ethanol (50/50 v%) mixture (M1) and the commercial membrane are in well agreement with the simulation results. Figure 2.3a illustrates the oxygen uptake results for the membrane phase separated in water (M2). For these membranes the applied gas pressure was varied. The experimental results of M2 membranes shown in Fig. 2.3a were obtained for a gas pressure of 2 bars. The slower response and gas side pressure dependency of M2 membranes coagulated in water reveal an additional mass transfer resistance in the membrane side for oxygen diffusion. This additional mass transfer limitation for M2 membranes may stem from the wetting of the membrane pores or from the particular morphology of the membrane. A structure with closed pores adds a mass transfer resistance to O_2 diffusion across the membrane.

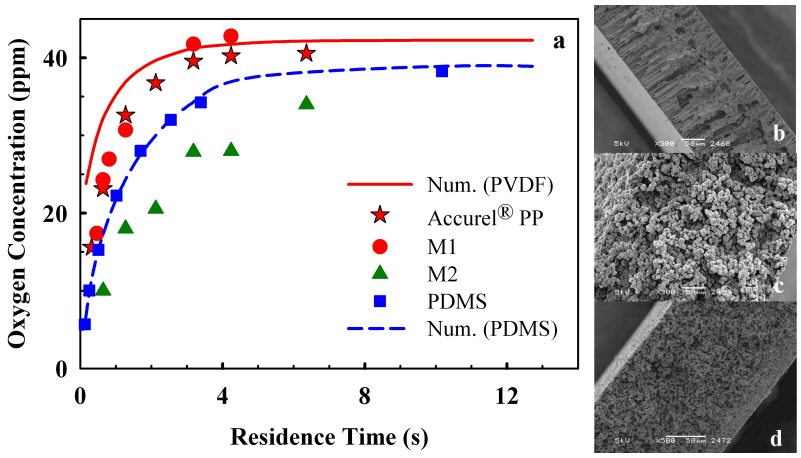

Figure 2.3: Effect of internal membrane structure. (a) O_2 absorption behavior of different membranes with respect to varying liquid residence time in a 500 μm wide and 100 μm deep channel. Cross sectional SEM images of 20 wt % PVDF membranes coagulated in water (b), in ethanol (c), and in water/ethanol (50/50 v%) (d)

Figure 2.3b-d show the cross sectional SEM images of the M2, M3, and M1 membranes, respectively. As can be clearly seen in Figure 2.3b, water as coagulant results in an asymmetric morphology with finger like macrovoids and a dense skin layer. Ethanol, as coagulant, results in a uniform morphology consisting of spherulites (Fig. 2.3c). The morphology of the resultant membranes indicate that water acts as a strong non-solvent, resulting in a dense skin layer, while ethanol acts as a milder non-solvent introducing a delay time for L/L demixing consistent with literature findings. [33, 34, 37] The slower G/L contacting response (Fig. 2.3a) and the lower N_2 permeance results (Table 2.1) of M2 membranes can be attributed to the formation of a denser layer and thereby showing an additional mass transfer resistance in gas diffusion across these membranes.

The gas liquid contacting experiments of membranes produced by ethanol coagulation (M3, Fig. 2.3c) were also conducted. However, liquid cross over to the gas side was observed for flow rates larger than 400 μl/min. Figure 2.3d illustrates the morphology of M1. Addition of ethanol eliminated the formation of macro-voids, and the skinned asym-

metric structure of phase separated membranes with pure water. Using water/ethanol (50/50 v%) mixture as coagulant results in successful gas/liquid contacting membranes, revealing gas transfer characteristics in a good agreement with the numerical simulations solved for non-wetted mode of operation. These findings and the O_2 transfer experiments clearly indicate the influence of membrane morphology on the G/L contacting performance of the resultant membranes and the opportunity of tuning porosity introduced in the micro-contactor. Moreover, the results of M1 membranes show that the dominant mass transfer resistance for O_2 transport is in the liquid phase. The G/L contacting interfaces formed at surface pores of the membrane decreases the hydrodynamic resistance in the confined microchannel.

The gas liquid contacting performance of a chip assembly including a flat dense PDMS membrane with a thickness of 100 μm is presented in Figure 2.3a, as a comparison to porous PVDF membrane results. In accordance to the PDMS simulation results, where the additional mass transfer resistance to O_2 diffusion across the PDMS membrane is included, the gas uptake is lower once the PDMS membrane is employed. Moreover, this major mass transfer resistance across the PDMS membrane retards the saturation of the microchannel, and an average outlet O_2 concentration of 39 ppm can be reached utmost. The microchannel is fully saturated within 3 seconds once the porous PVDF membranes are employed. The use of porous PVDF membranes eliminate the thickness dependent membrane side mass transfer resistances, reduce the residence time required for full O_2 saturation and eliminate any undesired size/affinity gas selectivity.

To investigate the mass transfer behavior in the liquid side, O_2 saturation experiments were performed for various flow rates of water with 400 μm wide channels having depths of 50 and 100 μm, respectively. The average oxygen concentrations at the outlets of the channels are plotted with respect to the intrinsic residence time for each channel depth (Figure 2.4). The results reveal that the saturation value of oxygen is reached faster for lower channel depth. Shorter diffusion distance in 50 μm deep channel results in a sooner saturation of the microchannel. Theory predicts the diffusion time of dissolved oxygen across the microchannel height to be proportional to the square of channel height, $H \sim \sqrt{2Dt}$, where D is oxygen diffusivity in water. As represented in Figure 2.4, the residence

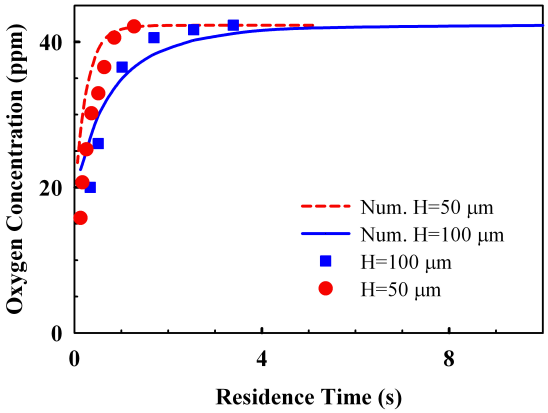

Figure 2.4: Average outlet oxygen concentrations as functions of residence time of the deoxygenated water for different channel depths. Here the width of the channels are 400 μm.

time required for full oxygen saturation across the cross section of the microchannels are scaled with the square of channel height. Experimental findings showed a residence time of approximately 0.6 and 2.5 seconds is sufficient for the oxygen saturation of 50 μm and 100 μm deep channels, respectively, validating the dominant mass transfer resistance is in the liquid phase.

The G/L contacting performance of the assemblies with the microstructured membranes were tested. PVDF membranes with shorter (M4) and taller (M5) micro-pillars were used. Figure 2.5 shows the oxygen uptake results measured at the outlet of the water channel of the assemblies including membranes M4 and M5 in comparison to the ones including flat M1 membranes. Once the micro-structured membranes are employed, gas uptake in the micro-channel is even faster compared to M1 flat membranes. This enhancement in the mass transport, which is driven by convection-diffusion, may suggest improved hydrodynamics. The superhydrophobicity of the microstructured membranes (Table 2.2) and the additional gas pockets in between the micro-pillars can induce slip flow at the membrane boundary of the microchannel, which promotes the mass transfer rate of oxygen.

From a practical viewpoint, wall slip can be desirable because of re-

duction in flow resistance. Furthermore, the hydrodynamic slippage can very significantly enhance transport phenomena originating at interfaces. Beavers et al. [45] were the first to investigate the fluid flow at porous media/fluid interfaces and proposed a slip boundary condition at these porous interfaces. Recent reports suggest rough, topographically and chemically heterogeneous, specifically engineered surfaces for generating slip velocity. [41–44] Previous studies [41–43] have shown that the Cassie-Baxter state promotes slippage at the G/L interfaces established in between the micro-pillars. Micro-structured PVDF membranes induces slippage with additional gas entrapment at the fluid boundary. The experimental results demonstrated in Figure 2.5 indicate amplified gas absorption rates and thereby reveal the realization of Cassie-Baxter state and partial slippage at the G/L/S boundaries established between porous micro-pillars. The enhancements of the oxygen uptake for the flow rates; 250, 500, and 750 μl/min are 14 %, 20 %, and 8 % for the microstructured membrane with shorter pillars (M4) and 16 %, 28 %, and 22 % for the microstructured membrane with taller pillars (M5), respectively. The decreased impact of micro-pillars at a higher flow rate of 750 μl/min may imply the transition from Cassie-Baxter to Wenzel state at higher pressures.

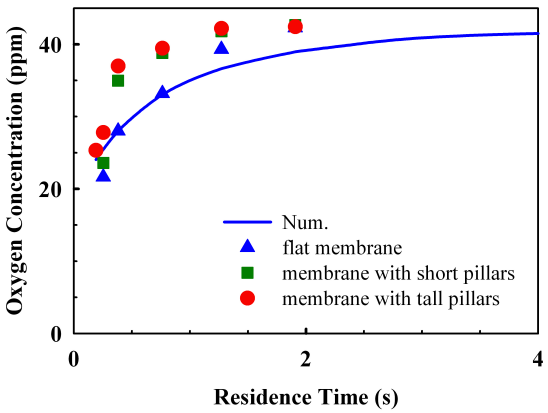

Figure 2.5: Influence of using micro-structured membranes on the oxygen mass transfer rate (width = 300 μm, height = 100 μm)

The enhanced mass transfer properties and promoted slippage make these superhydrophobic PVDF membranes prone to various applications.

The intrinsic tunable surface porosity enables the efficient supply and removal of gases for cells. The opportunity of generating shear-free boundaries at the G/L menisci in between the micro-pillars suggest these membranes as highly promising porous supports and/or as scaffolds for cells. The superhydrophobicity enables efficient water management. These promising properties of biocompatible, chemically resistant PVDF membranes affirm their high potential in many bio- related microfluidics, Bio-MEMS, tissue engineering, and cell culturing studies.

2.5 Conclusions

Porous, superhydrophobic PVDF membranes are integrated to microfluidic glass chips by the aid of UV-curable adhesives. Microfluidic devices comprising porous, superhydrophobic polymeric membranes and a conventional LOC substrate, glass, were stacked and sealed in a short time at ambient conditions. The developed assembly technique eliminated the necessity of mechanical compression in order to obtain a leak-free assembly, which in turn prevents any mechanical deformation of the membrane.

Oxygen transport experiments are in a well agreement with the numerical simulations of the proposed multiple layer micro G/L contactor. The experimental and numerical results obtained in this chapter showed;

1) The membrane morphology and hence membrane preparation parameters have an influence on the G/L contacting performance of the resultant membranes.
2) The opportunity of efficient supply of gases into liquids in a controlled manner.
3) The micro-structured membranes further enhance the mass transfer efficiency, as shear-free gas/liquid interfaces are established between the micro-structures, promoting the apparent hydrodynamic slippage.

The promising properties of the reported porous, superhydrophobic PVDF membranes enhancing all manifestations of interfacially driven phenomena confirms their high potential in various applications, in particular bio-related microfluidics and Bio-MEMS applications.

Bibliography

[1] Noble RD, Stern SA (1995) *Membrane Separations Technology: Principles and Applications, Ch 10; Membrane Contactors*, (Elsevier Science BV, Amsterdam).

[2] Rajabzadeh S,Yoshimoto S, Teramoto M, Al-Marzouqi M, Matsuyama H (2009) CO_2 absorption by using PVDF hollow fiber membrane contactors with various membrane structures. *Sep.and Pur. Technol.* 69(2):210-220.

[3] Li J-L, Chen B-H (2005) Review of CO_2 absorption using chemical solvents in hollow fiber membrane contactors. *Sep.and Pur. Technol.* 41(2):109-122.

[4] Mansourizadeh A, Ismail AF, Matsuura T (2010) Effect of operating conditions on the physical and chemical CO_2 absorption through the PVDF hollow fiber membrane contactor. *J. Mem. Sci.* 353(1-2):192-200.

[5] Wang D, Teo WK, Li K (2004) Selective removal of trace H_2S from gas streams containing CO_2 using hollow fibre membrane modules/contractors. *Sep.and Pur. Technol.* 35(2):125-131.

[6] Wang D, Teo WK, Li K (2002) Removal of H_2S to ultra-low concentrations using an asymmetric hollow fibre membrane module *Sep.and Pur. Technol.* 27(1):33-40.

[7] Park HH, Deshwal BR, Hang DJ, Choi WK, Kim IW, Lee HK (2009) Absorption of nitrogen dioxide by PVDF hollow fiber membranes in a G-L contactor. *Desalination* 243(1-3):52-64.

[8] Tan X, Tan SP, Teo WK, Li K (2006) Polyvinylidene fluoride (PVDF) hollow fibre membranes for ammonia removal from water. *J. Mem. Sci.* 271(1-2):59-68.

[9] Gabelman A, Hwang S-T (1999) Hollow fiber membrane contactors. *J. Mem. Sci.* 159(1-2):61-106.

[10] de Jong J, Verheijden PW, Lammertink RGH, Wessling M (2008) Generation of local concentration gradients by gasâĹŠliquid contacting. *Anal. Chem.* 80(9):3190-3197.

[11] Buonomenna MG, Drioli E, Bertoncello R, Milanese L, Prins LJ, Scrimin P, Licini G (2006) Ti(IV)/trialkanolamine catalytic polymeric membranes: Preparation, characterization, and use in oxygen transfer reactions. *J. Catalysis* 238(1):221-231.

[12] Schuster A, Lakshmanan R, Ponton J, Sefiane K (2003) Modelling a novel miniaturised reactor/separator system. *J. of Chem. Technol.* 78(2-3):342-346.

[13] Park CP, Maurya RA, Lee JH, Kim DP (2011) Efficient photosensitized oxygenations in phase contact enhanced microreactors. *Lab Chip* 11(11):1941-1945.

[14] Hessel V, Schouten JC, Renken A, Wang Y, Yoshida JI (2009) *Handbook of micro reactors*, (Willey VCH, Weinham).

[15] Hessel V, Hardt S, Löwe H (2004) *Chemical micro process engineering*, (Willey VCH, Weinham).

[16] de Jong J, Lammertink RGH, Wessling M (2006) Membranes and microfluidics: a review. *Lab Chip* 6(9):1125-1139.

[17] Park CP, Kim DP (2010) Dual-channel microreactor for gasâĹŠliquid syntheses. *J. Am. Chem. Soc.* 132(29):10102-10106.

[18] Polinkovsky M, Gutierrez E, Levchenko A, Groisman A (2009) Fine temporal control of the medium gas content and acidity and on-chip generation of series of oxygen concentrations for cell cultures. *Lab Chip* 9(8):1073-1084.

[19] Adler M, Polinkovsky M, Gutierrez E, Groisman A (2010) Generation of oxygen gradients with arbitrary shapes in a microfluidic device. *Lab Chip* 10(3):388-391.

[20] Skolimowski M, Nielsen MW, Emneus J, Molin S, Taboryski R, Sternberg C, Dufva M, Geschke O (2010) Microfluidic dissolved oxygen gradient generator biochip as a useful tool in bacterial biofilm studies. *Lab Chip* 10(16):2162-2169.

[21] Park J, Bansal T, Pinelis M, Maharbiz MM (2006) A microsystem for sensing and patterning oxidative microgradients during cell culture. *Lab Chip* 6(5):611-622.

[22] Vollmer AP, Probstein RF, Gilbert R, Thorsen T (2005) Development of an integrated microfluidic platform for dynamic oxygen sensing and delivery in a flowing medium. *Lab Chip* 5(10):1059-1066.

[23] Perez DG, Ferrell N, Castro NH, Hansford D (2010) Versatile methods for the fabrication of polyvinylidene fluoride microstructures. *Biomed. Microdevices* 12(6):1009-1017.

[24] Lee S, Bordatchev EV, Zeman MJF, (2008) Femtosecond laser micromachining of polyvinylidene fluoride (PVDF)based piezo films. *J. of Micromech. and Microeng.* 18(4):045011.

[25] Niklaus F, Enoksson P, KÃd'lvesten E, Stemme G (2001) Low-temperature full wafer adhesive bonding. *J. of Micromech. and Microeng.* 11(2):100-107.

[26] Pan CT, Yang H, Shen SC, Chou MC, Chou HP (2002) A low temperature wafer bonding technique using patternable materials. *J. of Micromech. and Microeng.* 12(5):611.

[27] Arayanarakool R, Le Gac S, van den Berg A (2010) Low-temperature, simple and fast integration technique of microfluidic chips by using a UV curable adhesive. *Lab Chip* 10(16):2115-2121.

[28] Kwon JW, Hongyu Y, Kim ES (2005) Film transfer and bonding techniques for covering single-chip ejector array with microchannels and reservoirs. *J. Microelectromech. Syst.* 14(6):1399-1408.

[29] Lee C, Yang EH, Saeidi SM, Khodadadi JM (2006) Fabrication, characterization, and computational modeling of a piezoelectrically actuated microvalve for liquid flow control. *J. Microelectromech. Syst.* 15(3):686-696.

[30] Niklaus F, Andersson H, Enoksson P, Stemme G (2001) Low temperature full wafer adhesive bonding of structured wafers. *Sensors and Actuators A: Physical* 92(1-3):235-241.

[31] Noh HS, Moon KS, Cannon A, Hesketh PJ, Wong CP (2004) Wafer bonding using microwave heating of parylene intermediate layers *J.of Micromech. and Microeng.* 14(4):625.

[32] Wu H, Huang B, Zare RN, (2005) Construction of microfluidic chips using polydimethylsiloxane for adhesive bonding. *Lab Chip* 5(12):1393-1398.

[33] van de Witte P, Dijkstra PJ, van den Berg JWA, Feijen J (1996) Phase separation processes in polymer solutions in relation to membrane formation. *J. Mem. Sci.* 117(1-2):1 - 31.

[34] Liu F, Hashim NA, Liu Y, and Abed MRM, Li K (2011) Progress in the production and modification of PVDF membranes. *J. Mem. Sci.* 375(1-2):1-27.

[35] Shih HC, Yeh YS, Yasuda H (1990) Morphology of microporous polyvinylidene fluoride membranes studied by gas permeation and scanning electron microscopy. *J. Mem. Sci.* 50(3):299-317.

[36] Bottino A, Camera-Roda G, Capannelli G, Munari S (1991) The formation of microporous poly(vinylidene difluoride) membranes by phase separation. *J. Mem. Sci.* 57(1):1-20.

[37] Sukitpaneenit P, Chung TS (2009) Molecular elucidation of morphology and mechanical properties of PVDF hollow fiber membranes from aspects of phase inversion, crystallization and rheology. *J. Mem. Sci.* 340(1-2):192-205.

[38] Vogelaar L, Lammertink RGH, Jonathan BN, Nijdam W, Versteeg B, Lydia AM, van Rijn CJM, Wessling M (2005) Phase separation micromolding: a new generic approach for microstructuring various materials. *Small* 1(6):645-655.

[39] Green DW (1984) *Perry's Chemical Engineers' Handbook*, (McGraw Hill).

[40] Blume I, Schwering PJW, Mulder MHV, Smolders CA (1991) Vapour sorption and permeation properties of poly(dimethylsiloxane) films. *J. Mem. Sci.* 61:85-97.

[41] Tsai PA, Peters AM, Pirat C, Wessling M, Lammertink RGH, Lohse D (2009) Quantifying effective slip length over micropatterned hydrophobic surfaces. *Phys. Fluids* 21(11):112002.

[42] Tsai PA, Lammertink RGH, Wessling M, Lohse D (2010) Evaporation-triggered wetting transition for water droplets upon hydrophobic microstructures. *Phys. Rev. Lett.* 104(4):116102.

[43] Bhushan B, Jung YC (2007) Wetting study of patterned surfaces for superhydrophobicity. *Ultramicroscopy* 107(10-11):1033-1041.

[44] Ajdari A, Lydéric B (2006) Giant amplification of interfacially driven transport by hydrodynamic slip: diffusio-osmosis and beyond. *Phys. Rev. Lett.* 96(18):186102.

[45] Beavers GS, Sparrow EM, Magnuson RA (1970) Experiments on coupled parallel flows in a channel and a bounding porous medium. *J. Basic Eng.* 92(4):843-848.

[46] Yeh HM, Cheng TW (1999) Analysis of the slip effect on the permeate flux in membrane ultrafiltration. *J. Mem. Sci.* 154(1):41-51.

3

Transport on Bubble Mattresses

In this chapter, numerical studies of momentum and mass transport on bubble mattress type geometries are presented. Bubble mattresses comprise periodic gas-liquid and solid-liquid interfaces. They resemble superhydrophobic hybrid substrates that are highly promising for hydrodynamic slippage such as topographically heterogeneous, micro-engineered substrates and porous membranes. In this study, bubble mattresses are established at the boundary of microchannels. A pressure-driven microflow passes perpendicularly aligned shear-free slippery microbubble surfaces established in between non-slippery solid microchannel walls. The effects of the surface porosity and the interface curvature of the microbubbles on the hydrodynamic slippage and interfacial mass transport are examined. The numerical results show a maximum effective slip length, corresponding to 11 % mass transfer enhancement with respect to a fully saturated non-slippery wall, when the protrusion angle θ of the microbubbles $\approx 10^o$. Simulations reveal a strong dependency of the effective slippage on the protrusion angles θ of the bubbles into the flow. Similarly, the interfacial mass transfer is shown to depend on the interface geometry of the bubble mattresses, *i.e.* microbubble protrusion angle and surface porosity.

This chapter is based on the publication Haase AS, Karatay E, Tsai PA, Lammertink RGH (2013) *Soft Matter*, doi: 10.1039/C3SM51408K

3.1 Introduction

One of the most exploited microfluidic laminar flow problem is hydrodynamic drag due to the increasing hydrodynamic flow resistances with decreasing channel dimensions in micro scale systems. [1–3] The classical no-slip boundary condition at smooth solid-fluid interfaces has been investigated intensively and often regarded valid down to nanometer length scales. [1] Slip length values - quantifying the slippage - of only few nanometers have been reported for smooth hydrophobic surfaces. [1, 3, 4] Whereas recent studies concluded that surface roughness or topographic structures that are specifically engineered on hydrophobic substrates lead to substantial apparent slippage. [5–8] These hydrophobic microstructures contain trapped air bubbles. The fluid flowing over such heterogeneous substrates contact periodic shear-free air surfaces and non-slippery solid walls and thereby effective partial slip conditions. Experimental and theoretical effective slip length values on the order of micrometers are reported for such hybrid substrates. [1, 3, 4] The effective slip length b_{eff} is considered as an hypothetical distance below the surface at which the no-slip boundary condition would be satisfied and commonly defined by Navier's slip condition [9]

$$u_x|_{(y=0)} = b_{eff} \left. \frac{du_x}{dy} \right|_{(y=0)} \tag{3.1}$$

Several theoretical and numerical studies have shown that the effective slippage on hybrid substrates depend on the orientation of the trapped air bubbles with respect to the flow direction and on the interface geometry of these bubbles. [10–14] The trapped air bubbles can be aligned longitudinally, transversely or obliquely to the flow direction. Previous theoretical studies reveal that the gas-liquid interface menisci can dramatically alter the effective slippage when the bubbles are aligned transverse to the flow direction. [12, 15, 16] Asymmetric slip profiles are reported for bubbles having convex and concave geometries. Furthermore, a transition from slippage state to friction state has been predicted for trapped bubbles transversely aligned to the flow direction. [15–17] A recent analytical

study by Davis et al. [15] considers two dimensional shear flow over a perpendicular array of bubbles with projected diameters of L_g. (Fig. 3.1) The dimensionless slip length $2b/L_g$ is shown to depend only on the bubble protrusion angle θ and surface porosity φ $(=L_g/L)$

$$\frac{2b}{L_g} = \pi\varphi \int_0^\infty A(s)ds$$

$$A(s) = \frac{s}{\sinh\left[2s(\pi-\varphi)\right] + s\,\sin 2\theta} \times \left[\cos 2\theta + \frac{s\,\sin 2\theta\,\cosh\left[s\pi\right] + \sinh\left[s(\pi-2\theta)\right]}{\sinh\left[s\pi\right]}\right] \tag{3.2}$$

The results of the analytical model in equation 3.2 presented in Ref. [15] reveal that the effective slip length is positive for negative θ and positive θ up to a critical protrusion angle θ_c (when $\theta < \theta_c$). Negative slip lengths are obtained when $\theta > \theta_c$, revealing a transition to frictional state for largely protruding bubbles obstructing the flow fields.

The interfacial transport of mass and heat is driven by convection-diffusion mechanism and explicitly coupled to the momentum transport over the partially slippery hybrid substrates. Therefore interfacial transport characteristics can be enhanced considerably in bubble mattress type geometries. It has been shown theoretically that even with slip lengths on the order of nanometers, interfacially driven transport of mass and heat can be enhanced up to two orders of magnitude. [8] Various studies have been performed addressing the influence of hydrodynamic slippage on interfacial transport in electro-osmotic flows [8, 18–20], in thin film evaporation in microchannels [21] and in mass transfer through permeable surfaces. [22–26]

These studies highlight the opportunity of controlling and amplifying the interfacial transport facilitated by partially slippery hybrid substrates containing trapped air bubbles. In this chapter, the effects of the gas-liquid interface geometry and the surface porosity on both momentum and mass transport characteristics are investigated numerically in detail for bubble mattress type configurations.

3.2 Numerical Simulations

The computational model of the bubble mattress is shown in Fig. 3.1. The non-periodic numerical model considers two dimensional steady laminar liquid flow and the mass transfer of species dissolving at the bubble surfaces in a channel. The bubble surfaces are rigid and spherical, with a small capillary number $Ca = \tau_w L_g/\sigma < 0.1$ where τ_w is the shear stress imposed by the liquid on the hybrid wall and σ is the interfacial tension of the air-water interface. [27]

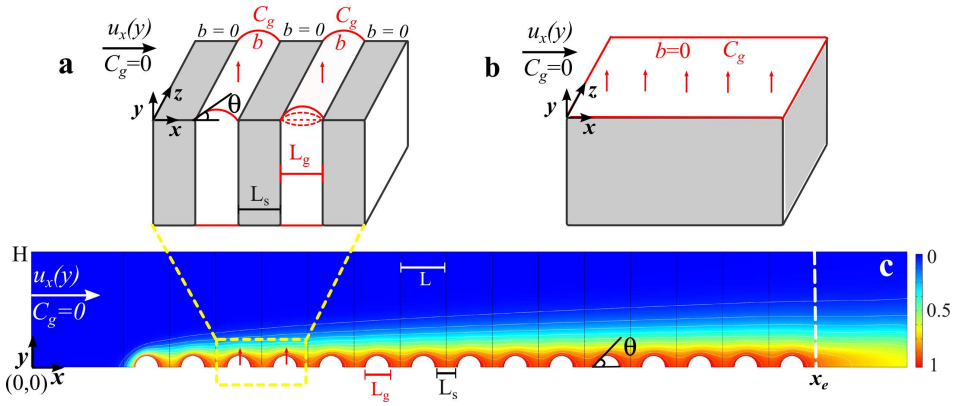

Figure 3.1: Microbubble mattress configuration. (a) Schematic representation of two bubble units with relevant boundary conditions. The curved red solid lines depict the bubble interfaces with protrusion angles θ aligned perpendicular to a microflow. The curved red dashed lines display the variations in θ. The bubble surfaces are slippery and they have a finite concentration of a species (C_0). L_g is the projected diameters of the bubbles that are rigid and pinned at the corners of non-slippery solid-liquid interfaces (L_s). Along L_s species concentrations are zero. (b) Schematic representation of reference microchannel bottom wall that is flat, non-slippery and with a concentration of species at C_0. In (a) and (b) the red arrows in y depict the direction of mass flux originated from the surface. (c) A representative numerical result of species concentration profile originating from the lower boundary, $y = 0$. Here, the white dashed line at $x = x_e$ shows the axial location where the mass and momentum fluxes and average bulk concentrations are evaluated.

The fluid is flowing in a microchannel with an height H of 100 μm.

The upper channel wall ($y = 100\mu$m) is a non-slippery wall and the lower channel wall ($y = 0$) is partially slippery including the bubble mattress. The fluid flow in the x-direction is pressure-driven by a fixed pressure gradient ΔP/Δx = 1800 Pa/m over the computational domain, where Δx = 680 μm. The bubble mattress consists of N bubble units with a total length of $NL = 600$ μm. Here L is the length of one periodic bubble unit ($L = L_g + L_s$). L_g is the projected bubble diameter and L_s is the length of solid-liquid interface. (Fig. 3.1a and c) To eliminate entrance and outlet effects, additional 40 μm is added both in the front and in the end of periodic bubble units. (Fig. 3.1c)

In the simulations, the bubble protrusion angle θ and the surface porosity φ is varied. The protrusion angles of the bubbles are parametrized by circular arc estimation for -90 $\leq \theta \leq$ 90. The surface porosity $\varphi = L_g/L$ is varied to be $\varphi = 1/3$, $\varphi = 1/2$ and $\varphi = 2/3$, keeping L_g constant at 20μm.

For the liquid flow over the bubble mattress, continuity equation and Navier-Stokes equations for incompressible and steady flow are solved.

$$\nabla . u = 0 \tag{3.3}$$

$$\rho u . \nabla u = -\nabla P + \mu \nabla^2 u \tag{3.4}$$

where ρ and μ are the liquid density and viscosity, respectively. P is the liquid pressure and u is the velocity vector. Pressure-driven flow fields are solved by applying $P = P_0$ at $x = x_o$ as inlet boundary condition and $P = P_1$ at $x = x_1$ as outlet boundary condition. It is assumed that the gas phase has negligible viscosity with respect to the liquid viscosity. Therefore, no-shear boundary conditions are applied at the bubble surfaces (i.e. $b = \infty$). No-slip boundary conditions are applied at the solid-liquid interfaces at $y =$ H and at $y = 0$ coinciding L_s ($b = 0$).

Mass transfer of species dissolving from the bubble surfaces to the liquid flowing in the microchannel is described by convection diffusion equation.

$$\nabla.(uc) = \nabla.(D\nabla c) \tag{3.5}$$

where c is the species concentration dissolved in the liquid phase and D is the diffusivity of the species in the liquid. Equation 3.5 is solved for concentration fields in the liquid microchannel. The inlet concentration is prescribed to be zero ($c = 0$ at $x = x_0$). At the outlet, the concentration is finite. ($\nabla c = 0$) Constant solute concentration boundary conditions are imposed on the gas/liquid interfaces. The concentrations at the solid-liquid interfaces are zero at $y =$ H and at $y = 0$ coinciding L_s ($c = 0$).

The governing equations (Eqns. 3.3-3.5) are solved using finite element methods. (Comsol Multiphysics v4.1) Flow fields and concentration profiles are computed sequentially in two steps. Meshing of the numerical models is performed automatically, where the element size is optimised for fluid dynamics with maximum and minimum element sizes of respectively 1.3 μm and 0.15 μm. Near boundaries, smaller element sizes have been used with maximum and minimum sizes of respectively 0.67 μm and 0.02 μm. The number of mesh elements are $\sim 1.5 \times 10^5$ in the computational domain for $L_g = 20$ μm and -90 $\leq \theta \leq$ 90.

3.2.1 Evaluation of Effective Slippage

The hydrodynamic slippage is quantified by effective slip lengths b_{eff}. The computed velocity fields in the simulations are used in calculating b_{eff}. The two-dimensional, steady, fully developed Stokes flow between parallel plates was analytically solved with a no-slip BC at the upper wall ($u = 0$ at $y =$ H) and Navier's slip boundary condition (eqn. 3.1) at the lower wall ($u = u_x|_{(y=0)}$). An expression for the velocity profile u_x incorporated with b_{eff} is derived.

$$u_x(y) = \frac{1}{2\mu}\frac{\Delta P}{\Delta x}(y^2 - Hy) + u_x|_{(y=0)}\left(1 - \frac{y}{H}\right) \tag{3.6}$$

The fluid flux ϕ is written using eqn. 3.6 as

$$\phi = < u_x(y) > = \frac{\int_0^H u_x(y)dy}{H} = -\frac{H^2}{12\mu}\frac{\Delta P}{\Delta x} + \frac{u_x|_{(y=0)}}{2} \tag{3.7}$$

The slip velocity is expressed by employing Navier's slip boundary condition

$$u_x|_{(y=0)} = b_{eff}\frac{du}{dy}\bigg|_{(y=0)} = -\frac{b_{eff}H}{2\mu}\frac{\Delta P}{\Delta x}\left(1 + \frac{b_{eff}}{H}\right)^{-1} \tag{3.8}$$

Substituting the expression for slip velocity (eqn. 3.8) in equation 3.7 and further rearranging yields the expression for b_{eff} in terms of pressure drop, fluid flux and physical constants.

$$b_{eff} = \frac{-\phi - \frac{H^2}{12\mu}\frac{\Delta P}{\Delta x}}{\frac{\phi}{H} + \frac{H}{3\mu}\frac{\Delta P}{\Delta x}} \tag{3.9}$$

It is important to note here that $\Delta P/\Delta x$ is the overall pressure drop across the channel length. The effective slip lengths are calculated at the middle of the channel length over 360 μm (along x over the middle ~ 9 bubble units). Therefore local pressure gradients $\partial P/\partial x$ are employed in equation 3.9 when calculating b_{eff}.

3.2.2 Evaluation of Mass Transfer Enhancements

To evaluate the mass transfer characteristics for fluid flow over a bubble mattress, mass transfer enhancements E are calculated with respect to a reference model depicted in Figure 3.1b. This reference model describes the mass transfer in a reference state chosen to be a two-dimensional fluid flow in a microchannel with identical dimensions with the microchannel embedded with the microbubbles. The reference microchannel walls are non-slippery walls ($b = 0$ at $y = 0$ and $y = \mathrm{H}$). The lower wall ($y = 0$) is saturated with the dissolving species ($c = c_0$ at $y = 0$ for all x).

The mass transfer enhancements are calculated by the ratio of the total mass fluxes obtained for the microchannel embedded with the microbubbles and the microchannel having smooth walls, at the same axial location $x = x_e$. The total mass flux is equivalent to the convective mass flux and described as

$$\psi|_{(x=x_e)} = \frac{\int_0^H u_x(y)c(x,y)dy}{H} = \phi < c > \tag{3.10}$$

The mass flux expression given in equation 3.10 equals the product of fluid flux ϕ and the mixing-cup average species concentration at x_e. Here ϕ and $< C >$ are given as

$$\phi|_{(x=x_e)} = \frac{\int_0^H u_x(y)dy}{H} \tag{3.11}$$

$$< c > |_{(x=x_e)} = \frac{\int_0^H u_x(y)c(x,y)dy}{\int_0^H u_x(y)dy} \tag{3.12}$$

Mass transfer flux enhancement E^ψ is calculated from the ratio of mass flux of the microchannel embedded with bubbles (ψ) and the microchannel with smooth walls (ψ_{ref}). Similarly, the fluid flux enhancement E^ϕ and the enhancement in the bulk concentration at $x = x_e$ (E^c) is calculated.

$$E^\psi = \frac{\psi}{\psi_{ref}} \tag{3.13a}$$

$$E^\phi = \frac{\phi}{\phi_{ref}} \tag{3.13b}$$

$$E^c = \frac{< c >}{< c >_{ref}} \tag{3.13c}$$

$$E^\psi = E^\phi \times E^c \tag{3.13d}$$

It is important to note that the mass flux enhancement is functions of fluid flux enhancement and flow-averaged concentration enhancement (Eqn. 3.13d). The contributions of E^{ϕ} and E^{c} to the mass transfer enhancement are evaluated separately in detail.

3.3 Results and Discussion

3.3.1 Momentum Transport

The extent of effective slippage affects the momentum transport and hence the fluid flux over the bubble mattress. In Figure 3.2 the dimensionless effective slip length $2b_{eff}/L_g$ profiles with respect to varying protrusion angles θ of the bubbles are presented for different surface porosities φ. The slip length profiles reveal qualitatively different trends between convex and concave gas bubbles. The slip length is positive for $\theta < 0$. whereas, both positive and negative slip is observed when $\theta > 0$. The profiles have two distinct regions, separated by a critical protrusion angle $\theta_c = 55^o$. For $\theta < \theta_c$, the slip length is positive, i.e. reduced hydrodynamic friction towards fluid flow. For $\theta > \theta_c$, slip lengths are negative, i.e. increased hydrodynamic friction towards fluid flow.

The detailed flow fields near bubble surfaces for bubble units with different θ are presented in Figure 3.3 for $\varphi = 0.5$. The flow profile for a negative θ = -65^o shows that the liquid inside the bubble pocket becomes stagnant. (Fig. 3.3a) Therefore, the liquid past recessing microbubbles flows over alternating liquid/stagnant-liquid and liquid/solid interfaces. As the friction at liquid surfaces is smaller than friction at solid surfaces, the effective slip length is positive for negative protrusion angles and b_{eff} profiles reveal a plateau when -90 $< \theta <$ -60.

Effective slip lengths are at maximum when -20 $< \theta <$ 30 for all φ. (Fig. 3.2) The detailed flow profile obtained for nearly flat bubbles (θ = 1^o) are shown in Figure 3.3b. The slippery gas-liquid interface results in a higher effective liquid velocity close to the lower wall. As the flat-like bubbles do not largely protrude into the liquid flow, the cross-sectional

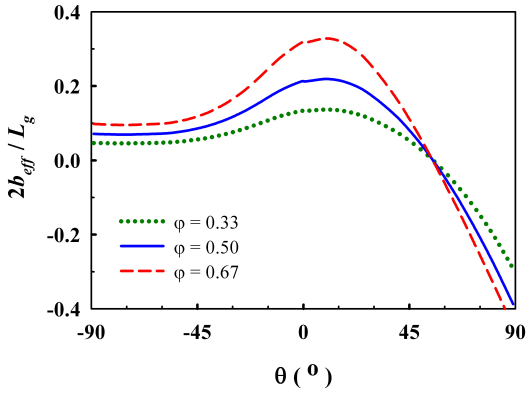

Figure 3.2: Dimensionless effective slip length $2b_{eff}/L_g$ profiles as functions of protrusion angles θ and surface porosities φ. The dashed line, ----, the solid line, ——, and the dotted line, ·····, represent the results for surface porosities $\varphi = 0.67$, $\varphi = 0.50$ and $\varphi = 0.33$, respectively.

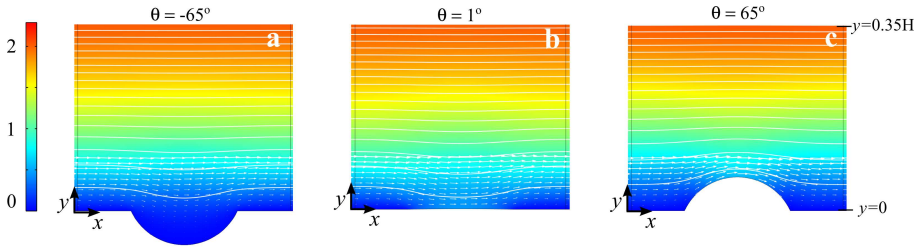

Figure 3.3: Numerical results of the pressure-driven flow over a micro-bubble unit at $\varphi = 0.5$ for varying protrusion angles. (a) θ = -65^o (b) $\theta = 1^o$ (c) $\theta = 65^o$. In (a-c) solid white lines show the flow streamlines. The arrow plots reveal the detailed velocity fields near bubble surfaces. The color surface plots show the velocity magnitudes.

area available for fluid flow is not significantly reduced. This minimizes $\partial P/\partial x$ and maximizes the fluid flux ϕ over the bubble mattress.

The effective slip lengths b_{eff} decreases for larger protrusion angles till $\theta = \theta_c$. When the critical protrusion angle $\theta_c = 55^o$ is reached, the slippage at gas-liquid interfaces is counteracted by the resistance induced by the geometric obstruction of the bubbles towards the flow. When $\theta > \theta_c$, the dissipation induced by the flow obstruction is dominant and negative slip

lengths b_{eff} are obtained, indicative of frictional state. Previous studies report critical protrusion angles in the range of 62^o to 69^o, slightly higher than 55^o. [15–17] However, these studies consider periodic Couette flow, while the results of non-periodic pressure-driven flow are obtained in this study. The slightly lower θ_c for pressure-driven flow can be attributed to different flow settings. It is worth mentioning that a critical protrusion angle of 62^o was obtained in the simulations performed for periodic Couette flow in this study for comparison purposes.

Figure 3.2 reveals the effect of surface porosity φ on the effective slip length. The trend of b_{eff} profiles remain qualitatively similar whereas larger b_{eff} values are obtained for larger φ. As the surface porosity increases, the shear-free fraction of the bubble mattress increases. Larger slippery gas-liquid interface lengths result in larger effective slip lengths.

The dilute limit model of Davis et al. [15] (Eqn. 3.2) predicts that the dimensionless slip length depends linearly on the surface porosity φ. Whereas this model underestimates the effective slip length for larger surface porosities ($\varphi > 0.35$). [12] Even though qualitatively similar b_{eff} profiles are predicted. [15] The numerical results obtained in this study reveal that the increase in porosity-normalized effective slip length $(2b_{eff}/L_g)/\varphi$ is larger for increasing φ when $\varphi > 0.35$. This nonlinear increase in effective slip may be explained by considering that for high surface porosities the solid-liquid interfaces becomes smaller. The liquid between the bubbles become stagnant. As a result, the liquid flows over a hybrid surface with an alternating pattern of liquid-gas and liquid/stagnant-liquid instead of liquid-gas and liquid-solid. As the friction on liquid surfaces is smaller than that of solid surfaces, the increase in b_{eff} is nonlinear with the increase in φ.

Finally, the numerical results for pressure-driven flow past transversely aligned microbubbles show that for a given porosity, the dimensionless slip length normalized by the projected length of the gas-liquid interface L_g is independent of the applied pressure gradient $\Delta P/\Delta x$, the periodic bubble unit length L and the number of bubble units N.

3.3.2 Interfacial Mass Transport

Figure 3.1 shows a representative concentration distribution of the dissolved species in the liquid flowing transverse to the microbubbles where

the mass transport is originated from ($y = 0$). Here, $\theta = 90^o$ and $\varphi = 0.5$. To investigate the interfacial mass transfer characteristics on a slippery bubble mattress, the ratio of the dissolved species fluxes obtained for the bubble mattress configuration and the non-slippery microchannel with a fully saturated flat boundary at $y = 0$ are calculated at $x = x_e$. (Fig. 3.1) This ratio is referred to as the species flux enhancement E^{ψ}. (eqn. 3.13a) For a given pressure gradient both the fluid flux and the mass flux evaluated at $x = x_e$ are constant for the reference microchannel. The pressure gradient for the bubble mattress has been chosen such that the solute concentration at the upper wall (y = H) is negligible. This ensures that the mass transfer rate is not affected by the accumulation of the dissolved species at the upper wall. As $E^{\psi} = E^{\phi} \times E^{c}$ (eqn. 3.13d), the fluid flux enhancement E^{ϕ} and the flow-averaged concentration enhancement E^{c} have been evaluated to identify the major sources contributing to the species flux enhancement.

The mass flux of dissolved species, fluid flux and flow-averaged concentration enhancement profiles for a bubble mattress with $L_g = 20$ μm are provided in Figure 3.4. The mass transfer enhancement profiles shown in Figure 3.4a reveal the dependency of the species flux enhancement E^{ψ} on the protrusion angles θ. For all surface porosities φ, E^{ψ} profiles are qualitatively similar. Three different regions are identified and depicted by the vertical straight solid lines in Figure 3.4. The different behavior of E^{ψ} in separate regions indicate the differences in dominating mass transfer mechanisms. The qualitative similarity of fluid flux enhancement E^{ϕ} profiles shown in Figure 3.4b to E^{ψ} profiles suggest that the transition of these different regions are mainly determined by E^{ϕ}. Region I is described when -90^o $\leq \theta \lesssim$ -30^o. Here for all φ, E^{ψ} is smaller than unity and $E^{\phi} \approx 1$. In region I, the rate of increase in E^{ψ} is linearly correlated with the increase in surface porosity φ. Region II is described when -30^o $\lesssim \theta \lesssim 55^o$. In this region, there is a nonlinear dependency of mass transfer enhancement E^{ψ} on both θ and φ. In addition for a large surface porosity $\varphi = 0.67$, the mass transfer is enhanced for all θ and E^{ψ} reaches a maximum at an optimal $\theta \approx 25^o$. Region III is described when $55^o \lesssim \theta \leq 90^o$. Here the rate of increase in E^{ψ} is either gradually increasing or constant. As decreasing E^{ϕ} and linearly increasing E^{c} are counteracting on each other for all φ and θ.

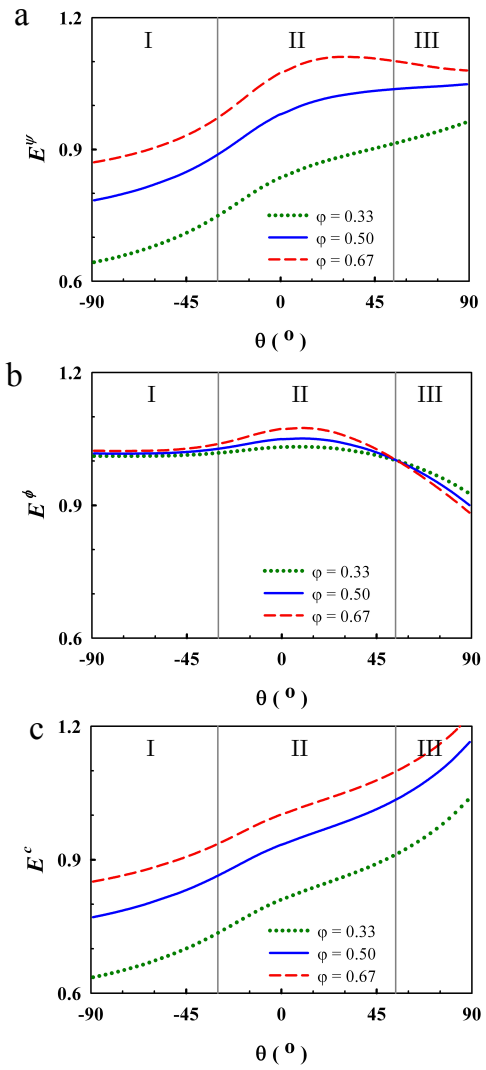

Figure 3.4: The effects of varying protrusion angles θ and surface porosities φ on the flux enhancements. (a) dissolved species mass flux enhancement E^{ψ} (b) fluid flux enhancement E^{ϕ} (c) enhancement of outlet bulk concentration E^{c}. Here $E^{\psi} = E^{\phi} \times E^{c}$. In (a-c) the dashed lines, ▬ ▬, the solid line, ▬, and the dotted lines, ▪▪▪, represent the results for surface porosities $\varphi = 0.67$, $\varphi = 0.50$ and $\varphi = 0.33$, respectively.

In region I, the mixing-cup concentrations calculated at $x = x_e$ for the bubble mattress is considerably lower than that for the reference microchannel for all θ and φ ($E^c < 1$). This reveals that the average concentration of dissolved species at the hybrid wall embedded with the microbubbles ($y = 0$) is lower compared to that of reference non-slippery saturated microchannel wall at $y = 0$. The species dissolved at the recessed microbubble surfaces diffuse through the stagnant liquid filling the bubble pockets to reach the convective bulk liquid flow. This additional vertical diffusion length brings a mass transfer resistance which decreases with increasing protrusion angles θ and thereby resulting in larger E^c and E^ψ. ($E^\phi \approx 1$)

The moderate protrusion angles in region II results in larger effective slip lengths compared to regions I and III. Therefore, the fluid flux enhancements E^ϕ are maximal in the second region for all φ. The large effective wall slip enhances mass uptake as the convective fluid flow in the axial direction x is enhanced. The slippery curved bubble interfaces result in also finite y-components of the velocity vectors near the bubble surfaces, which induces additional mass transport in y direction. Besides for larger protrusion angles θ, the bubbles protrude more into the liquid flow and thereby dissolved species at the bubble surfaces are exposed to larger velocities. (larger E^c for larger θ) The enhanced momentum transport in both x- and y-direction results in considerable increase in mass transfer enhancements E^ψ. It is important to note here that for large surface porosities $\varphi > 0.5$, the mass transfer is enhanced for all θ in the second region ($E^\psi > 1$). The rate of increase in E^ψ increases up to $\theta = 25^o$ revealing a maximum mass transfer enhancement of 11% for $\varphi = 0.67$. The decrease in the rate of increase in E^ψ when $\theta > 25^o$ indicates that the bubbles start to act as obstacles to the flow when $\theta > 10^o$. As E^ϕ starts to decrease at $\theta = 10^o$.

The effective slip lengths are negative for the protrusion angles in region III (Fig. 3.2) and thereby $E^\phi < 1$ (Fig. 3.4b). Whereas the amount of the dissolved species near the bubble mattress increases with increasing θ due to both increasing bubble area equivalent to the interfacial mass transfer area and increasing bubble protrusion depth. The latter situation entails that the dissolved species at largely protruding bubble surfaces encounter faster flowing liquid lamina. Moreover, the wavy fluid flow just

above the bubble mattress enhances convective transport in the y-direction (Fig. 3.3c). Hence the solute flux enhancement E^{ψ} keeps increasing for $\varphi < 0.5$ or approaches a plateau value for $\varphi > 0.5$, even though the frictional state when $\theta > 55^{o}$.

Figure 3.4 shows that E^{ψ} depends nonlinearly on the surface porosity φ. This reflects the nonlinear correlation of both E^{ϕ} and E^{c} with φ. The dependency of E^{ϕ} on the surface porosity is similar to the previously discussed correlation between effective slip length b_{eff} and φ. The nonlinear dependency of E^{c} on φ can be explained in two folds. First, the average concentration above the bubble mattress is low due to a smaller solute exchange area for the bubble mattress compared to that of reference microchannel wall. The interfacial mass transfer area increases for increasing φ. Second, for low φ, the fluid velocity just above the bubble mattress is small, since $b_{eff} \sim \varphi$. Considering lower porosities, upon an increase in φ both effects cause an increase in the flow-averaged concentration $< c >$ more than the proportional increase in φ. Whereas for larger surface porosities, the solute concentration near the hybrid wall embedded with the microbubbles approaches a full saturation wall due to larger slip velocities inducing near surface convection, minimizing the concentration variations along the periodic gas-liquid and solid-liquid interface lengths.

The numerical results shown in Figure 3.4 reveal the strong coupling of momentum and mass transport in a microchannel embedded with transversely aligned microbubbles with respect to a pressure-driven microflow. The detailed analysis of mass transfer enhancements compared to a reference microchannel having smooth non-slippery walls and a fully saturated wall clearly show the dependency of interfacial mass transport originated from the microbubble surfaces on the protrusion angles θ and the surface porosity φ.

3.4 Conclusions

The influence of the interface geometry of a partially slippery bubble mattress on momentum and interfacial mass transport are numerically studied. Simulations for two-dimensional steady pressure-driven flow over a bubble mattress show the dependency of effective slippage on bubble protrusion

angle θ and surface porosity φ, consistent with previously published results for Couette flow.

Interfacial mass transfer characteristics on bubble mattress type geometries are examined. The mass fluxes of dissolved species at the bubble surfaces are obtained and compared to that of a flat saturated non-slippery wall. The results revealed three distinct regions for varying protrusion angles. Mass transport is diffusion limited when -90^o $\leq \theta \lesssim$ -30^o. The interfacial transport of dissolved species are enhanced by promoted hydrodynamic slippage when -30^o $\lesssim \theta \lesssim$ 55^o. Though a frictional state when $\theta > \theta_c = 55^o$, the bubble interface geometry, *i.e.* larger area and protrusion, enhances the mass transport for 55^o $\lesssim \theta \leq$ 90^o. Maximum flux enhancements are obtained for moderate positive protrusion angles. (Region II) The mass transfer enhancements up to 11% are obtained for microbubbles with $L_g = 20$ μm when $\varphi = 0.67$. Larger enhancements can be obtained for larger bubbles, higher surface porosities, and increased fluid flows.

The numerical results presented in this chapter reveal that the fluid flow throughput and the mass flux of species dissolving at the transversely aligned microbubble surfaces can be tailored simultaneously. The proposed bubble mattress type geometries are highly promising in both micro and macro scale gas-liquid processes.

Bibliography

[1] Lauga E, Brenner MP, Stone HA (2007) in *Handbook of Experimental Fluid Dynamics*, eds Tropea C, Yarin A, Foss JF (Springer, New York), chap.19.

[2] Stone HA, Stroock AD, Ajdari A (2004) Engineering Flows in Small Devices: Microfluidics Toward a Lab-on-a-Chip *Annu. Rev. Fluid Mech.* 36:381-411.

[3] Rothstein JP (2010) Slip on superhydrophobic surfaces. *Annu. Rev. Fluid Mech.* 42:89-109.

[4] Vinogradova OI, Belyaev AV (2011) Wetting, roughness and flow boundary conditions. *J. Phys.: Condens. Matter* 23:184104.

[5] Tsai PA, Peters AM, Pirat C, Wessling M, Lammertink RGH, Lohse D (2009) Quantifying effective slip length over micropatterned hydrophobic surfaces. *Phys. Fluids* 21 (11) : 112002.

[6] Tsai PA, Lammertink RGH, Wessling M, Lohse D (2010) Evaporation-triggered wetting transition for water droplets upon hydrophobic microstructures. *Phys. Rev. Lett.* 104 (4) : 116102.

[7] Bhushan B, Jung YC (2007) Wetting study of patterned surfaces for superhydrophobicity. *Ultramicroscopy* 107 (10-11) : 1033-1041.

[8] Ajdari A,Lydéric B (2006) Giant amplification of interfacially driven transport by hydrodynamic slip: diffusio-osmosis and beyond. *Phys. Rev. Lett.* 96 (18) : 186102.

[9] Navier CLMH (1823) Mémoire sur les lois du mouvement des fluids *Mem. Acad. Sci. Inst. Fr.* 6 : 389-416.

[10] Teo CJ, Khoo BC (2010) Flow past superhydrophobic surfaces containing longitudinal grooves: effects of interface curvature. *Micro-Nanofluidics* 9:499-511.

[11] Hyväluoma J, Kunert C, Harting J (2011) Simulations of slip flow on nanobubble-laden surfaces. *J. Phys: Cond. Matter.* 23:184106.

[12] Ng C, Wang CY (2011) Effective slip for Stokes flow over a surface patterned with two- or three-dimensional protrusions. *Fluid Dyn. Res.* 43:065504.

[13] Schmieschek S, Belyaev AV, Harting J, Vinogradova OI (2012) Tensorial slip of superhydrophobic channels. *Phys. Rev. E* 85:016324.

[14] Bocquet L, Barrat J-L (2007) Flow boundary conditions from nano- to micro-scales. *Soft Matter* 3:685-693.

[15] Davis AMJ, Lauga E (2009) Geometric transition in friction for flow over a bubble mattress. *Phys. Fluids* 21:011701.

[16] Hyväluoma J, Harting J (2008) Slip Flow Over Structured Surfaces with Entrapped Microbubbles. *Phys. Rev. Lett.* 100:246001.

[17] Steinberger A, Cottin-Bizonne C, Kleimann P, Charlaix E (2007) High firction on a bubble mattress. *Nature Mater.* 6:665-668.

[18] Joly L, Ybert C, Trizac E, Bocquet L (2004) Hydrodynamics within the electric double layer on slipping surfaces. *Phys. Rev. Lett.* 93(25):257805

[19] Squires TM (2008) Electrokinetic flows over inhomogeneously slipping surfaces. *Phys. Fluids* 20(9):092105.

[20] Zhao H (2010) Electro-osmotic flow over a charged superhydrophobic surface. *Phys. Rev. E* 81:066314.

[21] Biswal L, Som S, Chakraborty S (2011) Thin film evaporation in microchannels with interfacial slip. *Microfluidics and Nanofluidics* 10:155-163.

[22] Beavers GS, Joseph DD (1967) Boundary conditions at a naturally permeable wall. *J.Fluid Mech.* 30:197-207.

[23] Chellam S, Wiesner M, Dawson C (1992) Slip at a Uniformly Porous Boundary - Effect on Fluid Flow and Mass Transfer. *J. Eng. Math.* 26:481-492.

[24] Ramon G, Agnon Y, Dosoretz C (2009) Heat transfer in vacuum membrane distillation: Effect of velocity slip. *J. Mem. Sci.* 331:117-125.

[25] Karatay E, Lammertink RGH (2012) Oxygenation by a superhydrophobic slip G/L contactor. *Lab Chip* 12:2922-2929.

[26] Jani JM, Wessling M, Lammertink RGH (2012) A microgrooved membrane based gas-liquid contactor. *Microfluidics Nanofluidics* 13:499-509

[27] Gao P, Feng JJ (2009) Enhanced slip on a patterned substrate due to depinning of contact line. *Phys. Fluids* 21:102102

4

Control of Slippage with Tunable Bubble Mattresses

TAILORING the hydrodynamic boundary condition is essential for both applied and fundamental aspects of drag reduction. Hydrodynamic friction on superhydrophobic substrates providing gas-liquid interfaces can potentially be optimized by controlling the interface geometry. Therefore, establishing stable and optimal interfaces is crucial but rather challenging. Here novel superhydrophobic microfluidic devices that allow the presence of stable and controllable microbubbles at the boundary of the microchannels are presented. The effect of micro-bubble geometry on the slippage is examined experimentally and numerically at high resolution. The effective slip length is obtained for a wide range of protrusion angles θ of the micro-bubbles into the flow using a micro-particle image velocimetry technique. The numerical results reveal a maximum effective slip length, corresponding to a 23 % drag reduction at an optimal $\theta \approx 10°$. In agreement with the simulation results, the measurements correspond up to 21 % drag reduction when θ is in the range of -2° to 12°. The experimental and numerical results reveal a decrease in slip length with increasing protrusion angles when $\theta \gtrsim 10°$. Such microfluidic devices with tunable slippage are essential for the amplified interfacial transport of fluids and particles.

This chapter is based on the publication Karatay E, Haase AS, Visser CW, Sun C, Lohse D, Tsai PA, Lammertink RGH (2013) *PNAS*, 110(21):8422-8426.

4.1 Introduction

Despite more than two decades of intense research on hydrodynamic slippage on substrates with various physicochemical properties [1–4], tuning the hydrodynamic slippage remains a challenge, especially for microfluidic laminar flow. The slip length - quantifying the slippage - ranges from a few nanometers for flat hydrophobic substrates to several micrometers for superhydrophobic substrates with hybrid (liquid-gas and liquid-solid) interfaces [4]. Hydrophobic microstructures containing trapped gas bubbles have been shown to be advantageous for drag reduction [5–11]. Their orientation with respect to the flow direction [12–16] and the geometry of gas-liquid menisci [11–14, 17] have been demonstrated to affect the slippage. In particular, micro-scale bubbles transverse to the flow direction can alter the flow resistance depending on the protrusion of the bubbles into the flow. Moreover, transition from slippage to friction has been predicted for trapped bubbles perpendicular to the flow in theoretical [14, 18] and numerical studies [12, 13, 19, 20]. The presence of such a critical protrusion angle highlights the feasibility of manipulating the flow resistance via bubble geometry. One recent experimental study suggests that for flow over a hydrophobic surface with trapped passive micro-bubbles, there is a transition from an enhanced slippage state to the frictional state at a large protrusion angle, in an estimated range of 30^o to 60^o [20]. However, there has been no experimental investigation of flow past a hydrophobic surface with transversely embedded micro-bubbles for a wide range of protrusion angles at high resolution. In this chapter, integrated microfluidic devices that permit the presence of stable and controllable micro-bubbles at the boundary of hydrophobic microchannels are reported. The effect of geometry of the micro-bubbles transverse to a pressure-driven flow on the effective slippage is examined in detail.

4.2 Experimental

4.2.1 Microfluidic Device

Figure 4.1a-c show the microfluidic devices consisting of two main microchannels for separate gas and water flow, connected by an array of

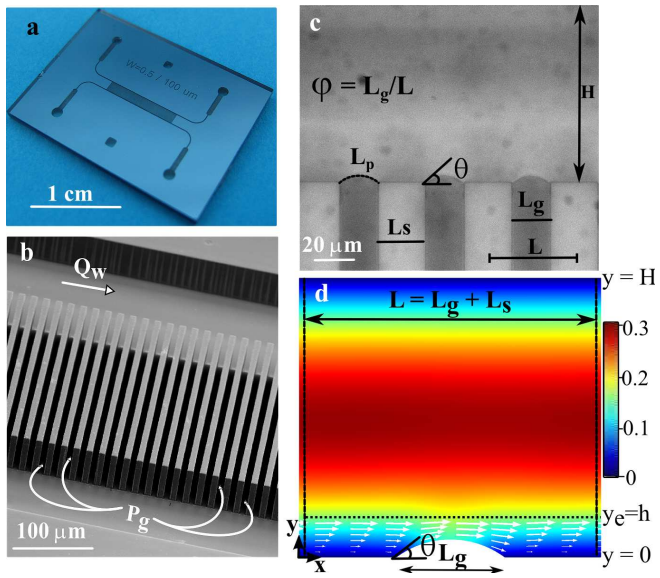

Figure 4.1: Controllable microfluidic bubble mattress and computational bubble unit cell. (a) Optical image of the microfluidic device with integrated gas and liquid channels. (b) Scanning electron microscopy image of a representative microfluidic device, showing two main microchannels for gas (P_g) and liquid (Q_w) streams connected by gas-filled side channels. (c) Bright-field microscopy image of bubbles protruding 35 ± 3.3^o into the liquid microchannel with a height of H. Here, the shear free fraction, φ, is defined as $L_g/L = L_g/(L_s + L_g)$, where L_g is the width of the gas gap, and L_s is the width of the solid boundary. (d) Numerical results of the pressure-driven flow over a micro-bubble unit using the same experimental parameters. The color bar refers to the velocity, which is given in m/s. Here $\varphi = 0.38$ and $Q_w = 45$ μl/min.

side channels in between. Silicon microchannels were fabricated by photolithography followed by a deep reactive ion etching process. The microchannels were sealed by anodic bonding to glass. The width of the main microchannels, H, is 50 μm. The width of the gas-filled side channels L_g was kept constant at 20 μm and the length of the liquid-solid interface L_s was varied (30 μm and 20 μm, respectively). The periodic bubble unit length is given as $L = L_g + L_s$. The shear-free fraction (surface porosity) is defined as $\varphi = L_g/L$ (Fig. 4.1c). The ratio of the bubble unit cell length

L to the channel hydraulic radius $R_h = 33.3$ μm is $\delta = L/R_h$. The effective slip length was quantified for different shear-free fractions φ (~0.38 and ~0.54) and spatial periods normalized by the hydraulic radius, $\delta = L/R_h$ (= 1.5 and = 1.2). The protrusion angles of the micro-bubbles were varied over a wide range (-2^o to 43^o) with small gas pressure changes applied (0.29 to 0.34 bar) for a liquid flow rate of 45 μl/min. The experiments were performed at a sufficiently small Capillary number, $Ca = \tau_w/(\sigma/L_g) \approx 5{\times}10^{-3}$, and Weber number, $We = (\rho < u_x >^2 L_g)/\sigma \approx 6{\times}10^{-3}$, to ensure symmetric micro-bubbles pinned at the sharp corners of the side channels. Here τ_w is the shear stress imposed by the liquid on the hybrid wall and σ is the interfacial tension of the air-water interface.

4.2.2 μPIV Experiments

Steady, laminar velocity profiles at the focal plane in the middle of the microchannel depth were measured using a micro-particle image velocimetry (μPIV) technique, as described in Ref. [11]. Milli-Q water seeded with 1 μm diameter fluorescent particles was used as the working fluid. A dual cavity Nd:YAG laser at 532 nm was used for channel illumination. Image pairs with a delay time of 7 μs between two exposures were recorded using a double-shutter PCO Sensicam camera with a resolution of 1376 × 1040 pixels × 12 bit. To enhance particle visibility and the signal-to-noise ratio of the correlation map, image pre-processing was performed before cross-correlation. Averaged mean intensity images were calculated and subtracted from the image pairs. The particle image density was artificially increased by using a consecutive sum of five images in a row to increase the resolution of the final vector field. The interrogation view of the μPIV images was ~222 μm × ~167 μm. A multi-grid ensemble correlation averaging method was employed for 195 image pairs. When processing the data, the interrogation window size was decreased in steps to a size of 32 × 16 pixels (~ 5.2 μm × 2.6 μm) to achieve a high spatial resolution for the detailed velocity profiles. The experimental data have high signal-to-noise ratios. Therefore, no smoothing needed to be applied to the velocity fields. For each measurement, bright-field images were acquired to determine the protrusion angle and to define the locations of the bubbles and walls on the raw μPIV images.

4.2.3 Calculation of Effective Slip Length

In addition to the experimental studies, the effective slip length was also numerically calculated. A two-dimensional finite element method (Comsol Multiphysics v4.1) similar to that described in Chapter 2 of this thesis is used in solving the Navier-Stokes equations for a steady pressure-driven flow of water in a microchannel consisting of 15 successive bubble units at the bottom surface. 2-bubble unit cell length was required for the entrance/outlet effects and developing flow effects. The bubbles are pinned and approximated as rigid circular arcs calculated by the projected diameter of bubble, L_g, and the protrusion angle θ. The bubble interface curvature is parameterized by the protrusion angle θ. A perfect slip boundary condition for the bubble surfaces and no-slip boundary condition for solid walls was assumed. The upper solid wall is a non-slipping wall at a distance $y = H$. Pressure-driven flow was produced by applying a laminar flow with a mean velocity of 0.2 m/s as the inlet condition. The effective slip length for all θ is calculated at an evaluation line, $y_e = 6.5$ μm, due to the protrusion depth of bubbles in the y-direction into the channel. The evaluation line at height y_e is sufficiently above the bubble surfaces for all θ. The effective slip length is calculated based on Navier's slip boundary condition.

$$u_x|_{(y=0)} = b_{eff} \left. \frac{du_x}{dy} \right|_{(y=0)} \tag{4.1}$$

The ratio of the velocity $u_x(y_e)$ to the tangential shear rate at y_e, du_x/dy, is integrated along x over the middle 11 bubble units, and y_e is subtracted from the resultant value to obtain b_{eff}.

4.2.4 Calculation of Effective Friction Factor

To obtain the Fanning friction factor C_f, a two-dimensional, steady, fully developed Stokes flow between parallel plates was analytically solved using the no-slip boundary condition at the upper plate, $y = H$, and the full-slip boundary condition at the bottom plate, $y = 0$. Due to the protrusion depth of bubbles in the y-direction, the effective hydrodynamic boundary

position depends on y. The effective slip length b_{eff} is incorporated using a linear approximation of velocity in the close proximity of the solid wall, $y = y_e$, yielding the following relation between the slip velocity at $y = 0$ and the velocity at $y = y_e$.

$$u_x(y = 0) = u_x(y = y_e)\frac{b_{eff}}{b_{eff} + y_e} \tag{4.2}$$

Thereby, $u_x(y = y_e)$ can be expressed as $(b_{eff} + y_e)(du_x/dy)|_{(y=0)}$, and the pressure drop can be expressed in terms of b_{eff}

$$\Delta P = \frac{-12\mu < u_x > (b_{eff} + H)}{H^2(4b_{eff} + H)} \tag{4.3}$$

Here ΔP (Pa/m) is the pressure gradient, μ is the dynamic viscosity of the liquid, and $< u_x >$ is the mean velocity. For a fully developed, steady laminar flow, the shear stress is given as $\tau_w = R_h \Delta P/2$. The definition of the Fanning friction factor $C_f = \tau_w/(0.5\rho < u_x >^2)$ [22] then immediately yields

$$C_f = \frac{R_h \Delta P}{\rho < u_x >^2} \tag{4.4}$$

Here, ρ is the liquid density. Using the experimental and numerical results, ΔP is calculated from equation 4.3 to obtain the friction factors for pressure-driven flow of water past micro-bubbles in the presented microfluidic devices using equation 4.4. It is worth noting that for the case of a straight rectangular duct ($b_{eff} = 0$), equation 4.3 reduces to plane Poiseuille flow $\Delta P = (-12\mu < u_x >)/H^2$, which can be further employed in equation 4.4 to derive $C_f = (12\mu R_h)/(\rho < u_x > H^2)$. For a smooth rectangular duct with an aspect ratio of 2, corresponding to the microchannels embedded with the microbubbles, $R_h = 2H/3$, yielding $C_f = 10.67/Re$ for a smooth, non-slippery rectangular duct. Hydrodynamic drag reductions can be calculated for different protrusion angles in comparison to non-slippery microchannels.

4.3 Results and Discussion

The designed and fabricated microfluidic devices consist of two main parallel microchannels for separate liquid and gas streams, connected by an array of side channels in between (see Fig. 4.1). To prevent the side channels from wetting, the original hydrophilic silicon microchannels are hydrophobized based on silane chemistry using perfluorinated octyltrichlorosilane [21]. Due to the hydrophobicity of the surface and the sufficiently large applied gas pressure P_g, the bridging side-channels are filled with gas. The control of the gas pressure results in tunable protrusion angles θ of the micro-bubbles and will compensate for gas dissolution into the fluid (Fig. 4.1b-c). Establishing stable and controllable bubbles is crucial in this study, which currently are attained by active control of gas pressure. In contrast, trapped passive bubbles are unstable as shown in previous studies [6, 11]. The shape and the stability of the interface are determined by capillary forces and the pressure difference between the gas and liquid phases [8].

This fluidic configuration allows for easy and precise control of the gas-liquid interface curvature. It also enables visualization of both the interface geometry and flow field near the bubble surfaces by direct velocity measurements of a steady, laminar flow past the micro-bubbles using microparticle image velocimetry (μPIV) [23].

The effect of the interface shape on slippage is also studied numerically by solving for the pressure-driven flow of water for the flow settings utilized in the experiments with a computational domain representing the experimental geometric parameters (Fig. 4.1d). Shear-free boundary conditions are applied along the gas protrusions, whereas no-slip boundary conditions are imposed on the solid walls. Figure 4.1d represents the computed flow field for $\theta \approx 35^o$ over a bubble unit with length L, consisting of one no-slip (solid-liquid) and one shear-free (gas-liquid) boundary condition.

4.3.1 Measured Velocity Profiles

In Figures 4.2-4.4, the flow velocity profiles measured in the middle of the microchannel depth by μPIV are presented, providing direct quantification of effective slippage for varying geometric parameters: the protrusion

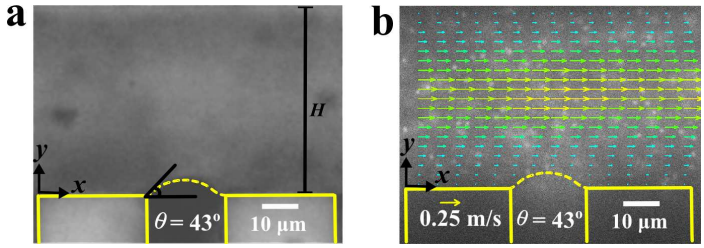

Figure 4.2: Experimental microbubble units. (a) Bright-field image of a bubble unit with a protrusion angle of $\theta = 43\pm6^o$. (b) Velocity field measurement for bubbles at $\theta = 43\pm6^o$ superimposed on its raw μPIV image. In (a-b) the dashed lines represent the bubble curvature and the solid lines represent the no-slip solid walls.

angle, θ and the shear-free fraction, φ. In Fig. 4.2a, a representative bright field image of a bubble unit with a protrusion angle of $\theta \approx 43^o$ is presented. Fig. 4.2b represents the velocity field for $\theta \approx 43^o$ protruding curved gas-liquid menisci, superimposed on a correspondent raw μPIV image. The bubble position and bubble curvature are depicted by dashed lines (Fig. 4.2a-b). The curvature of the bubbles is calculated by circular arc estimation. The bubbles are stable and symmetric during the experiments due to sufficiently low Capillary and Weber numbers ($Ca \approx 5{\times}10^{-3}$, $We \approx 6{\times}10^{-3}$). The bubbles' protrusion angles were accurately measured from the corresponding bright field images with ImageJ analysis. The error bars were calculated from the standard deviation of θ for each bubble.

The locations and profiles of four successive bubbles, having protrusion angles of 43^o, are represented in Fig. 4.3a. The curved gas-liquid interfaces protrude approximately 3.7 μm into the microchannel in the y-direction. A series of detailed velocity profiles, $u_x(y)$, at different channel heights, y, are presented in Fig. 4.3b. The presence of the micro-bubbles has a strong effect on the detailed velocity field. Near the wall, the variation of velocity field reflects the local variation of the hydrodynamic boundary condition. Even at $y = 0.15H$ ($y = 7.6$ μm), the effect of the bubbles on the flow field is still observed. Large protruding bubbles, as in this case ($\theta \approx 43^o$), can act as obstacles to the flow. Indeed, a slight deceleration of the flow is observed in front of the bubbles. Right behind the bubble, the loss in velocity is recovered and higher velocities are achieved. The overall average

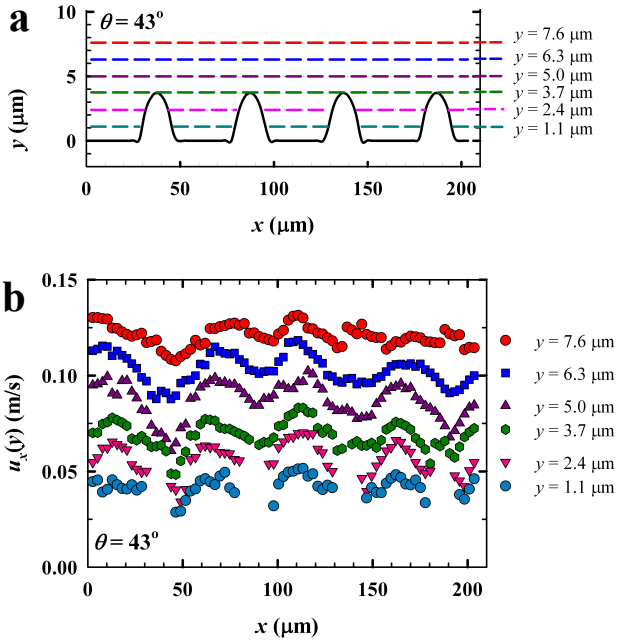

Figure 4.3: Detailed velocity profiles measured by μPIV. (a) The liquid-gas interfaces showing the bubbles having protrusion angles of $\theta = 43\pm6^o$. The curvature of the bubbles is calculated by circular arc estimation. The colored dashed lines indicate the vertical positions of the velocity measurements presented in b. (b) Detailed streamwise velocity profiles, $u_x(y)$, at different channel heights y, indicated by the corresponding dashed lines in a.

velocity in this case is still higher than that for non-slippery walls. These observations are consistent with the numerical findings of Hyväluoma et al. [13]

Fig. 4.4a presents the experimental and numerical velocity profiles obtained by the streamwise average of the local velocity profiles of the experiment shown in Fig. 4.4b. The measured and computed velocity profiles agree very well. The average velocity profiles near the hybrid wall are presented in Fig. 4.4b for the same experiment with $\theta = 43\pm6^o$ and for another experiment with $\theta = 21\pm3^o$. Near the hydrophobic surface embedded with curved gas-liquid interfaces, the velocity profiles exhibit a linear relation

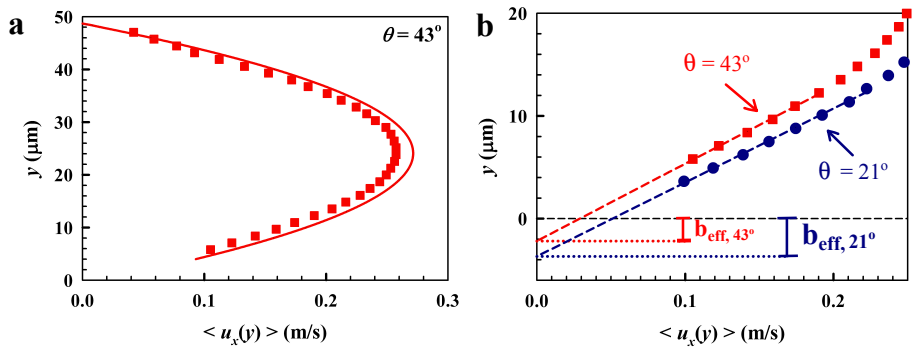

Figure 4.4: Average velocity profiles measured by μPIV. (a) Average velocity profile for $\theta = 43\pm6^o$ (experimental, ■, and numerical, ▬,). (b) Experimental average velocity profiles for $\theta = 43\pm6^o$ at a shear-free fraction $\varphi = 0.38$ (■) and $\theta = 21\pm3^o$ at a shear-free fraction $\varphi = 0.54$ (•), near the wall with attached bubbles. The dashed lines represent the linear fits for the b_{eff} evaluations.

between $< u_x(y) >$ and y. The effective slip length, b_{eff}, based on the average velocity profiles is calculated using Navier's slip boundary condition [4]: $u_x(y = 0) = b_{eff}(du_x/dy)|_{(y=0)}$. To obtain du_x/dy, a least-squares linear fitting was performed for the data below $y \approx 10$ μm. The effective slip length calculation is graphically represented in Fig. 4.4b. The effective slip length for bubbles protruding 43^o is smaller than that of 21^o. Though slight deceleration of the flow is observed in front of 43^o protruding bubbles (Fig. 4.4b), the effective slip length is found to be 1.8 ± 0.1 μm for this θ, showing that 43^o protruding bubbles still contribute to enhanced slippage. The numerical effective slip lengths were evaluated using the same approach with the local velocity gradients being calculated at $y = 6.5$ μm.

4.3.2 Comparison of b_{eff} with the analytical asymptotic solutions

To further verify the employed methods, the experimental and numerical results are compared with the analytical asymptotic solutions of the slip length for Stokes flow past periodically alternating, flat (protrusion angle $\theta = 0^o$) shear-free and no-slip regions transverse to the flow. [5] Three

distinct asymptotic limits for b_{eff} are considered, as suggested in Ref [5].

$$AL1: \quad b_{AL1} \sim \frac{\varphi}{4} R_h \qquad \varphi \ll 1, \qquad \delta\, fixed \tag{4.5a}$$

$$AL2: \quad b_{AL2} \sim \frac{\delta}{2\pi} ln(sec(\varphi \frac{\pi}{2})) R_h \qquad \delta \to 0, \qquad \varphi\, fixed \tag{4.5b}$$

$$AL3: \quad b_{AL3} \sim \frac{\varphi}{4(1-\varphi)} R_h \qquad \delta \to \infty, \qquad \varphi\, fixed \tag{4.5c}$$

where R_h is the hydraulic radius, and $\delta = L/R_h$. The first asymptotic limit (equation 4.5a) describes the limit at which the bubble fraction goes to zero for a given ratio of bubble unit length to hydraulic radius. The second (equation 4.5b) and the third (equation 4.5c) asymptotes describe the limits at which δ goes to zero and infinity, respectively, for a given φ.

Table 4.1: Comparison of effective slip length results with the asymptotic results of Ref. [5]. All slip length values are in μm. The last three columns refer to the values obtained from the asymptotic expressions given in equations 4.5a-4.5c.

φ	δ	b_{eff}		b_{AL1}	b_{AL2}	b_{AL3}
		μPIV	num.			
0.38	1.5	3.9±0.3	3.5	3.2	1.5	5.1
0.54	1.2	4.7±0.5	4.9	4.5	2.6	9.8

In Table 4.1, the numerical b_{eff} results obtained at $\theta = 0^o$ and the experimental b_{eff} results measured at $\theta = 1.2 \pm 0.3^o$ and $\theta = -1.9 \pm 0.5^o$ for $\varphi = 0.38$ and 0.54, respectively, are compared with the predictions resulting from equations 4.5a-4.5c. Indeed, the effective slip length results obtained both from the μPIV measurements and the numerical simulations agree well with the asymptotic prediction of the analytical solution, equation 4.5a. The slight discrepancy can be explained by the asymptotic limit of small φ for a constant δ of b_{AL1}. The asymptotic solutions b_{AL2} and b_{AL3} refer to the minimum and maximum slip length for the asymptotic extremes in δ. Table 4.1 indicates that for all φ, $b_{AL2} < b_{eff} < b_{AL3}$,

which further validates the consistency of the experimental and numerical effective slip length results evaluated for an intermediate δ. Both the experimental and numerical results of b_{eff} at $\theta \approx 0$ agree very well with the predictions of the analytical asymptotes of the ratio of shear-free fraction.

4.3.3 Dependence of Hydrodynamic Slippage on Bubble Geometry

In Figure 4.5, the first measurements of effective slip lengths for a wide range of protrusion angles θ are presented and compared with the numerical results. The measurements clearly demonstrate the dependence of the effective slip length on both θ and φ. When the fraction of the surface covered by bubbles is $\varphi = 0.54$, a maximum effective slip length of 4.8±0.1 μm was measured at $\theta = 12\pm2^o$. In addition, the experimental results reveal a decrease in the effective slip length with increasing protrusion angles when $\theta \gtrsim 12^o$. A similar trend was observed for $\varphi = 0.38$. For larger protrusion angles, $\theta \gtrsim 10^o$, the measured effective slip length decreases with increasing protrusion angle, implying an increasing flow resistance due to larger protrusions. There is good quantitative agreement with the numerical results.

The simulations reveal an asymmetry in the effective slip length between positive and negative protrusion angles, affirming previous reports. [13, 14, 18–20] Consistent with the experimental results, the numerical b_{eff} increases with increasing protrusion angle to a maximum value at $\theta = 11^o$ and subsequently decreases with further increases in θ for all φ. A peak position of b_{eff} was also encountered at a similar $\theta \approx 10^o$ in the theoretical solutions provided in Refs. [14, 18] and highlighted as an optimum angle in Ref. [14]. The effective slip length becomes zero at a critical protrusion angle, θ_c, above which the micro-bubbles exhibit negative slip length, revealing a transition from slippage to extra friction. The simulations yield $\theta_c \approx 62^o$ and $\theta_c \approx 68^o$ for $\varphi = 0.54$ and $\varphi = 0.38$, respectively, which are quantitatively consistent with the results of previous theoretical and numerical studies. [13, 14, 18–20]

The numerical data indicate that for θ beyond the value $\theta = 11^o$ giving maximal slip length, higher bubble fractions (here $\varphi = 0.54$) follow a steeper decrease in the effective slip length than lower ones (here $\varphi =$

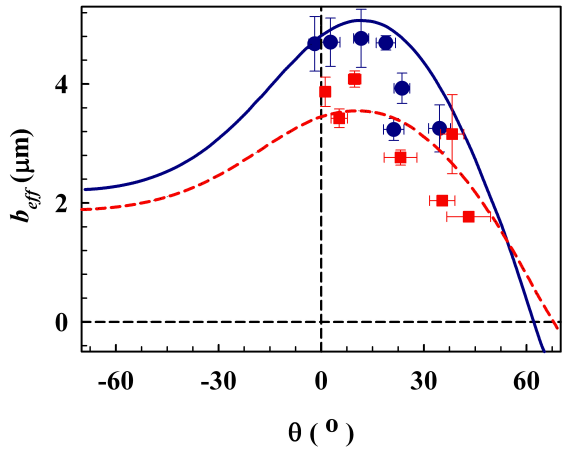

Figure 4.5: Experimental and numerical effective slip length b_{eff} as a function of the protrusion angle θ for $\varphi = 0.54$ and $\varphi = 0.38$. Here the solid line (▬) and the circles (●) indicate the numerical and experimental results for $\varphi = 0.54$. The dashed line (▬ ▬) and the squares (■) indicate the numerical and experimental results for $\varphi = 0.38$.

0.38). b_{eff} is smaller for $\varphi = 0.54$ (with a smaller $\theta_c \approx 62^o$) than for $\varphi = 0.38$ when $\theta \gtrsim 52^o$ (Fig. 4.5). The increase in protrusion angle alters the flow cross-sectional area. When the typical length scales of the system are comparable with the scale of bubble units, the change in the flow cross-sectional area and the interface curvature have an effect on the velocity field. These observations are consistent with the previous studies, suggesting the significant role of confinement effects on slippage over gas-liquid interfaces longitudinal to flow direction. [11, 12]

These findings suggest that the confinement effects and the gas-liquid interface geometry of the micro-bubbles have a strong effect on the effective slip length. Furthermore, the experimental results imply the possibility of engineering hydrodynamic slippage/drag by controlling the shape of the gas-liquid meniscus via external means.

To highlight the capability of tailoring the effective boundary condition in the presented microfluidic devices, the experimental and numerical data are recast in terms of the Fanning friction factors C_f. The pressure drop along the microchannel length is calculated using the expression in terms of

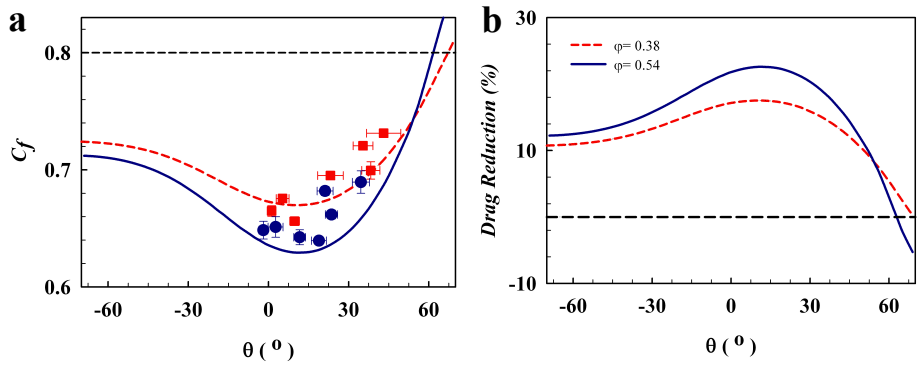

Figure 4.6: Experimental and numerical effective friction factor C_f and numerical drag reduction as a function of the protrusion angle θ. (a) Experimental and numerical C_f results for $\varphi = 0.54$ and $\varphi = 0.38$. (b) Numerical drag reduction results for $\varphi = 0.54$ and $\varphi = 0.38$. In (a) the circles (•) and the squares (■) indicate the experimental results for $\varphi = 0.54$ and $\varphi = 0.38$, respectively. In (a-b) the solid lines (——) and the dashed lines (– – –) represent the simulation results for $\varphi = 0.54$ and $\varphi = 0.38$, respectively. The horizontal black dashed lines represent the no-slip condition ($b = 0$ and $C_f = 0.8$).

b_{eff} (eqn. 4.3). The calculated ΔP values from equation 4.3 are employed in equation 4.4 to evaluate the friction factors for pressure-driven flow of water past micro-bubbles in the presented microfluidic devices. Figure 4.6a presents the effective friction factor values for varying protrusion angles of micro-bubbles for $\varphi = 0.38$ and $\varphi = 0.54$.

The friction factor is a direct measure of the pressure loss due to hydrodynamic drag. The effective friction factors of the micro-bubble mattress should be less than those of a rectangular duct with no-slip walls for $\theta < \theta_c$. The analytical model reduces to $C_f = 10.67/Re$ for a straight rectangular channel ($b_{eff} = 0$) with a width-to-height aspect ratio of 2, corresponding to the microchannels embedded with microbubbles. The analytical C_f value for $Re \approx 13$, as in the μPIV experiments and numerical simulations, is calculated as 0.8 for a non-slippery microchannel. This analytical friction coefficient, depicted by the dashed line in Fig. 4.6a, is larger than the friction coefficients of the hydrophobic microchannels with embedded micro-bubbles for $\theta < \theta_c$. At a critical $\theta = \theta_c$, the numerical results of

C_f are equal to the analytical friction factor (C_f = 0.8) for no-slip walls. When $\theta > \theta_c$, a higher friction factor appears, revealing a transition from slippage to extra friction. Fig. 4.6a emphasizes the significant effect of the interface menisci curvature on the hydrodynamic slippage.

Figure 4.6b shows the extent of drag reduction that can be tuned by controlling the shape of the gas-liquid menisci curvature. Here the black dash line represents a microchannel with non-slippery walls (b_{eff} = 0 and C_f = 0). The numerical results show when $\theta \approx 11^o$, 18 % and 23 % drag reductions are achieved for $\varphi = 0.38$ and $\varphi = 0.54$, respectively, compared with the flow in a non-slippery microchannel at the same flow rate. In good agreement with the numerical results, experimental drag reductions of 19 % and 21 % are obtained for $\varphi = 0.38$ and $\varphi = 0.54$, respectively, when θ is in the range of -2° to 12°.

4.4 Conclusions

In conclusion, a novel hydrophobic microfluidic device is presented allowing for the manipulation of flow resistance. The proposed design of the microfluidic device allows for the formation of stable and controllable micro-bubbles that are perpendicular to the pressure-driven flow in the microchannels. The experimental measurements, which cover a wide range of protrusion angles, reveal a strong dependence of the effective hydrodynamic slip on the gas-liquid interface curvature. The experimental results confirm the numerical simulations for effective slip length and the effective friction factor. The presented microfluidic device allows for the tuning of the convective flow throughput and, hence, the control of flow resistance. This active control is of paramount importance for microfluidic applications aiming to amplify the transport of fluids and particles at interfaces, which is driven by convection-diffusion mechanism. [24]

Bibliography

[1] Tretheway DC, Meinhart CD (2002) Apparent fluid slip at hydrophobic microchannel walls. *Phys. Fluids* 14(3):L9.

[2] Joseph P, Tabeling P (2005) Direct measurement of the apparent slip length. *Phys. Rev. E* 71:035303.

[3] Choi C-H, Westin KJA, Kenneth SB (2003) Apparent slip flows in hydrophilic and hydrophobic microchannels. *Phys. Fluids* 15(10):2897-2902.

[4] Lauga E, Brenner MP, Stone HA (2007) in *Handbook of Experimental Fluid Dynamics*, eds Tropea C, Yarin A, Foss JF (Springer, New York), chap.19.

[5] Lauga E, Stone HA (2003) Effective slip in pressure-driven Stokes flow. *J. Fluid Mech.* 489:55-77.

[6] Byun D, Kim J, Ko HS, Park HC (2008) Direct measurement of slip flows in superhydrophobic microchannels with transverse grooves. *Phys. Fluids* 20:113601.

[7] Choi C-H, Kim CJ (2006) Large slip of aqueous liquid flow over a nanoengineered superhydrophobic surface. *Phys. Rev. Lett.* 96(6):066001.

[8] Rothstein JP (2010) Slip on superhydrophobic surfaces. *Annu. Rev. Fluid Mech.* 42:89-109.

[9] Ou J, Perot B, Rothstein JP (2004) Laminar drag reduction in microchannels using ultrahydrophobic surfaces. *Phys. Fluids* 16(12):4635-4643.

[10] Ou J, Rothstein JP (2005) Direct velocity measurements of the flow past drag-reducing ultrahydrophobic surfaces. *Phys. Fluids* 17:103606.

[11] Tsai P, et al. (2009) Quantifying effective slip length over micropatterned hydrophobic surfaces. *Phys. Fluids* 21:112002.

[12] Teo CJ, Khoo BC (2010) Flow past superhydrophobic surfaces containing longitudinal grooves: effects of interface curvature. *Micro-Nanofluidics* 9:499-511.

[13] Hyväluoma J, Kunert C, Harting J (2011) Simulations of slip flow on nanobubble-laden surfaces. *J. Phys: Cond. Matter.* 23:184106.

[14] Ng C, Wang CY (2011) Effective slip for Stokes flow over a surface patterned with two- or three-dimensional protrusions. *Fluid Dyn. Res.* 43:065504.

[15] Schmieschek S, Belyaev AV, Harting J, Vinogradova OI (2012) Tensorial slip of superhydrophobic channels. *Phys. Rev. E* 85:016324.

[16] Bocquet L, Barrat J-L (2007) Flow boundary conditions from nano- to micro-scales. *Soft Matter* 3:685-693.

[17] Chen H, Li J, Chen D (2006) Study of drag forces on a designed surface in bubbly water lubrication using electrolysis. *J. Fluids Eng.* 128:1383-1389.

[18] Davis AMJ, Lauga E (2009) Geometric transition in friction for flow over a bubble mattress. *Phys. Fluids* 21:011701.

[19] Hyväluoma J, Harting J (2008) Slip Flow Over Structured Surfaces with Entrapped Microbubbles. *Phys. Rev. Lett.* 100:246001.

[20] Steinberger A, Cottin-Bizonne C, Kleimann P, Charlaix E (2007) High firction on a bubble mattress. *Nature Mater.* 6:665-668.

[21] Maboudian R, Ashurs WR, Carraro C (2000) Self-assembled monolayers as anti-stiction coatings for MEMS: characteristics and recent developments. *Sens. & Actuat. A: Phys.* 82:219-223.

[22] Cengel Y (2007) *Heat and Mass Transfer: A Practical Approach*, (Mc Graw Hill, New York).

[23] Raffel M, Willert C, Wereley S, Kompenhans J (2007) *Particle Image Velocimetry*, (Springer, Berlin Heidelberg).

[24] Bocquet L, Lauga E (2011) A smooth future? *Nature Mater.* 10:334-337.

5

Rate of Gas Absorption on a Slippery Bubble Mattress

Absorption of a pure gas into a liquid in laminar flow past a superhydrophobic surface including transversely embedded micro-bubbles is studied. The mass transfer of gas absorption at stable gas/liquid interfaces with controllable interface curvatures for short contacting times are experimentally measured and numerically estimated. The gas absorption is studied experimentally by in-situ measurements of dissolved oxygen concentration profiles in aqueous solutions flowing over the oxygen bubbles by fluorescent lifetime imaging microscopy. The dynamics of interfacial mass transfer of dissolved oxygen are analyzed numerically considering (i) kinetic equilibrium conditions at bubble surfaces that is conventionally described by Henry's Law and (ii) non-equilibrium conditions at bubble surfaces using Statistical Rate Theory (SRT). The measurements show that kinetic equilibrium is not established for short contact times. Mass transfer into liquid flow past micro-bubbles can be well described by the simulations performed at non-equilibrium conditions for short exposure times (~ 180 μs), deviating from the commonly accepted Henry's Law.

This chapter is based on the submitted manuscript Karatay E, Tsai PA, Lammertink RGH (2013)

5.1 Introduction

Gassing/degassing of liquids is of interest in various research fields and applications. Absorption/desorption kinetics at gas-liquid interfaces is of interest in numerous applications ranging from the multiphase chemical reactors to biotechnology in both macro- and micro-scale. [1–3] Traditional gas-liquid contacting equipment such as distillation columns, packed towers, tray/plate columns and bubble columns suggest a direct contact of gas-liquid, and phase equilibrium-based absorption/desorption processes at these interfaces. The mass transfer characteristics of such processes are studied extensively and the mass transfer resistances are reported to be determined by the transport of gaseous and dissolved species in the free gas and liquid phases, respectively. [1, 4, 5] The resistance of gas dissolution at the gas-liquid interface is commonly not considered due to fast equilibrium at the phase-boundary. Under equilibrium conditions, the concentrations in both gas and liquid phases at the gas-liquid boundary are proportional to their partial pressures. The concentration of the dissolved gas is at its maximum (i.e., saturation) value, which is commonly described by Henry's Law. [6]

Besides the conventional gas-liquid contacting equipment, the utilization of porous hydrophobic membranes in gas-liquid contacting have substantially increased due to several advantages including their fixed interfacial area used for the stabilization of the gas-liquid interfaces. [7–10] Mass transfer characteristics of gas absorption/desorption in membrane contactors have been widely studied. [7, 10–15] The overall mass transfer process is reported to consist of four consecutive steps; (i) transport from bulk gas phase to the outer surface of the membrane, (ii) diffusion through the membrane, (iii) dissolution of gas into liquid, and (iv) liquid phase transport. In these studies, overall mass transfer coefficients are investigated. Analytical and experimental mass transfer correlations are obtained for developing/fully-developed boundary layers using analogous heat transfer solutions of Graetz-Lévèque type. [14, 15] The mass transfer resistance of the liquid phase, in relation to operating parameters, and the mass transfer resistance of the membrane, in relation to the wetting phenomena, have been investigated in detail. [12, 13, 15] The mass transfer resistances in the gas phase and at the gas-liquid surfaces are commonly

neglected due to the fast gas phase diffusion and the assumption of equilibrium at the gas-liquid boundaries. The overall mass transfer correlations are of practical importance in design implications in membrane gas-liquid contacting.

The gas dissolution at the phase boundary has been reported to induce a major mass transfer resistance in gas absorption/desorption processes and investigated in many theoretical studies. [16–25] The surface resistances have been studied for both phase-equilibrium and non-equilibrium conditions. The stagnant film theory [18], Higbie's penetration theory [19] and the film-penetration theory [20] are among the widely used interface models at equilibrium conditions. The dynamics of non-equilibrium interface transport have also been investigated in previous analytical and theoretical studies based on kinetic and thermodynamic considerations. [22, 24] The mass transfer resistance of gas dissolution at the gas-liquid interfaces have been reported as the rate limiting step in gas absorption/desorption processes for short contacting times. [22, 25, 57] The non-equilibrium based interface models have been employed in various experimental studies investigating the evaporation of suspended droplets, the gas bubble evolution in liquids and gas adsorption/desorption kinetics on catalytic systems. [25–30]

Recent studies show that hydrophobic substrates containing passive / active gas bubbles present hydrodynamic slippage [31, 32, 37] as the liquid flows over those shear-free bubble surfaces. Effective slip lengths - quantifying the slippage - in the micrometer range are obtained for laminar flow past superhydrophobic hybrid (slippery liquid-gas and non-slippery liquid-solid) substrates in both experimental and theoretical studies. [31–39] Such fluidic platforms with slippery interfaces have been shown to enhance liquid convection and have been suggested to increase the interfacial mass transport rates. [32, 38, 40] In a recent theoretical study [41], enhancements of up to two orders of magnitude in interfacially driven transport phenomena are predicted on slippery surfaces. These studies highlight the room for investigation of interfacial gas transport at bubble surfaces trapped within hydrophobic microstructures for a better understanding of interfacial mass transfer characteristics on partially slippery surfaces as such provided by bubble mattress-like geometries. In the previous chapter, a superhydrophobic microfluidic device was presented that

allows for the formation of stable and active - gas pressure controlled - micro-bubbles at the boundary of microchannels. The experimental and numerical results shown in Chapter 4 of this thesis reveal the dependency of hydrodynamic slippage on the micro-bubble protrusion angle θ and surface porosity in the presented bubble mattress geometry. [32] To the best of our knowledge, the mass transfer characteristics of gas dissolution from microbubbles to a pressure-driven laminar flow past slippery hydrophobic substrates embedded with microbubbles have not been investigated so far.

Here, the oxygen absorption into a water stream in pressure-driven flow past a superhydrophobic surface with transversely embedded oxygen gas micro-bubbles is examined experimentally and numerically. The previously presented microfluidic devices [32] that allow for tunable gas phase pressure, bubble geometry, and liquid phase flow are used. The detailed spatial dissolved oxygen gas concentration profiles in the aqueous phase are measured with frequency-domain fluorescence lifetime imaging microscopy (FLIM). The oxygen sensitive molecular probe, ruthenium tris(2,2'-dipyridyl) dichloride hexahydrate (RTDP) is used to quantify the local dissolved oxygen gradients within the microchannels under flow conditions. The dynamics of interfacial mass transfer of dissolved oxygen in the liquid side microchannel embedded with curved oxygen microbubbles are studied at kinetic equilibrium state and at non-equilibrium state using Statistical Rate Theory (SRT).

5.2 Experimental Methods

5.2.1 Microfluidic Setup

Figure 5.1a shows a representative scanning microscopy image of silicon-glass based microfluidic devices. The microfluidic devices consist of two main parallel microchannels for separate aqueous solution and oxygen gas streams, connected by an array of side channels. [32] Silicon microchannels were fabricated by standard photolithography followed by a deep reactive ion etching process. The microchannels were sealed by anodic bonding to glass. To prevent the wetting of the connecting side channels, the original hydrophilic silicon microchannels were hydrophobized. The protocol described in Ref. [42] were adopted for the hydrophobization via ultraviolet

(UV) light illumination of silicone oil. The width of the main microchannels H was varied (50 μm or 100 μm). The width of the gas-filled side channels L_g was kept constant at 20 μm and the length of the liquid-solid interface L_s was varied (20 μm or 30 μm). The periodic bubble unit length is defined as $L = L_g + L_s$. Therefore, the periodic bubble unit length L was either 40 μm or 50 μm for different L_s. The surface porosity (shear-free fraction) is described to be $\varphi = L_g/L$, and varied to be 0.38 or 0.54 for different L_s. (see Fig. 5.1). The depth of the microchannels were 100 μm. The hydraulic radius of the microchannels were either $R_h = 33.3$ μm or $R_h = 50$ μm.

The flow rate of the liquid side was controlled by a syringe pump (HARVARD Apparatus PHD 2000) and the pressure of the oxygen gas stream was controlled by a pressure controller (Bronkhorst, EL-PRESS, P-602C). The side-channels were filled with oxygen gas due to the hydrophobicity of the microchannel walls and sufficiently large applied gas pressure P_g. The protrusion angles θ of the oxygen micro-bubbles into the aqueous stream were controlled by the active control of applied oxygen gas pressure. The protrusion angles of the oxygen micro-bubbles were varied in a range from 2^o to 45^o by changing the applied gas pressure ($\sim$ 0.6 to $\sim$ 1.2 bar) for varying liquid flow rates from 9 μl/min to 45 μl/min. During the measurements the micro-bubbles were stable and symmetrically pinned at the sharp corners of the side channels.

5.2.2 FLIM Experiments

The local dissolved oxygen concentrations in the liquid side channels were quantified by using a Ru-based oxygen sensitive luminescent dye, ruthenium tris(2,2'-dipyridyl) dichloride hexahydrate (RTDP) (Sigma Aldrich). Frequency domain fluorescent lifetime imaging microscopy (FD-FLIM) technique was employed to measure the lifetime gradients of RTDP aqueous solutions in the liquid phase microchannel embedded with oxygen gas micro-bubbles transversely aligned to the pressure-driven liquid flow. [45, 46] For the FLIM experiments a LIFA-X system (Lambert Instruments) was used on a Zeiss Axio Observer inverted microscope attached with a modulated LED light source and an intensified CCD camera (LI2CAM) in gated mode. During the measurements, intensifier MCP voltage was

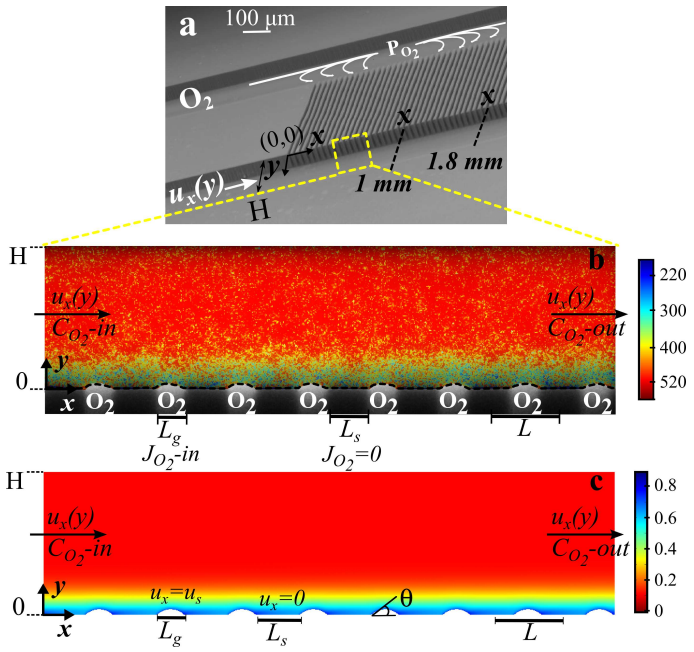

Figure 5.1: Microfluidic bubble mattress and oxygen dissolution at bubble surfaces. (a) Scanning electron microscopy image of the microfluidic device showing two main microchannels for oxygen gas (P_{O_2}) and water ($u_x(y)$) streams connected by oxygen-filled side channels. (b) Lifetime field resolved by FLIM superimposed on the bright-field microscopy image of the same experiment showing bubbles protruding $43^o \pm 2^o$ into the water side microchannel with a height of $H = 100$ μm. Here, the bubble profiles are calculated by circular arc estimation and depicted by the dashed line. (c) Numerical results of the dissolved oxygen concentration in the water side microchannel solved with the identical operating settings in (b). Here, L_g is the width of the oxygen-filled side channel($L_g = 20$ μm), and L_s is the width of the solid boundary($L_s = 32.6$ μm). The color bars refer to the lifetime of RTDP aqueous solution which is given in ns (b) and the oxygen concentration which is given in mol/m^3 in (c). In (b-c) surface porosity $\varphi = 0.38$ and $Q_w = 45\mu$l/min.

kept at 650 V. The optical sensing was carried out at a fixed modulation frequency of 100 kHz. 10 μM fluorescein (Sigma Aldrich) solution was used as a reference flourophore to test any instrumentation phase shift at

the operating frequency. Fluorescein is suitable as a reference phase shift flourophore due to its short lifetime $\tau < 6$ ns compared to RTDP (~ 600 ns). The data acquired was analyzed with LI-FLIM software package to resolve the lifetime fields.

400 μM aqueous solutions of RTDP were prepared. Lifetimes of the RTDP were measured in oxygen-free (N_2 saturated), aerated and oxygen-saturated aqueous solutions both on standard laminated microscopy slides and on the bubble mattresses. The solutions were saturated with a certain gas by simply bubbling that gas through the solution for sufficiently long times. The dissolved oxygen content of the solutions were confirmed by a fiber optic oxygen sensor (FIBOX 3, PreSens). For these standard measurements on the microfluidic platform, the microbubbles were established by nitrogen, air and oxygen gases for corresponding oxygen-free, aerated and oxygen-saturated aqueous solutions flowing past those transversely aligned microbubbles.

During the mass transfer experiments, oxygen gas microbubbles were established at the boundary of the microchannels. (Fig. 5.1b and 5.3) If otherwise not stated, deoxygenated RTDP aqueous solution was the running liquid flowing past the transversely aligned oxygen bubbles. The experiments were performed at room temperature without temperature regulation.

5.3 Numerical Simulations

5.3.1 Governing Equations

The mass transfer characteristics of oxygen gas dissolution at the surfaces of curved oxygen microbubbles aligned perpendicular to a pressure-driven microfluidic laminar flow is numerically studied. The coupled mass and momentum transport on the presented bubble mattress geometry are solved (Comsol Multiphysics v4.3). The computational domain represents the experimental geometric parameters (Fig. 5.1c). The velocity and concentration profiles in the liquid side microchannels are calculated with the same experimental operating settings. During the simulations, the gas side transport is not considered as the effects of mass transfer limitations

in the gas phase and the effects of oxygen depletion during gas dissolution vanishes due to the active supply of pure oxygen gas in our experiments.

The Navier-Stokes equations and the conservation of species equation (convection-diffusion) are solved for a steady pressure-driven flow of water in a microchannel consisting of 60 successive bubble units at the bottom surface ($y = 0$). In order to eliminate any developing flow effects and entrance/outlet effects, an entrance and outlet section of 2-bubble unit cell length was included in the front and end of the bubble mattress. The bubbles are rigid, non-deformed and pinned at the corners of side channels, as in the experiments. The bubble profiles are approximated as circular arcs. The bubble interface curvature was parametrized by the protrusion angle θ. (Fig. 5.1c)

The pressure-driven laminar flow was produced by applying a mean velocity as the inlet condition. The inlet mean velocities were varied in the range of 0.04 to 0.2 m/s, consistent with the experiments. Shear-free boundary conditions (*i.e.* perfect slip) were applied on the bubble surfaces and no-slip boundary conditions for the solid microchannel walls (at the bottom wall along each L_s at $y = 0$ and the upper wall at $y = \mathrm{H}$).

The steady-state conservation of species equation (5.1) was solved for the dissolved oxygen transport. The oxygen dissolves at the microbubble surfaces. The dissolved oxygen profiles in the liquid side microchannel are determined by convection-diffusion mechanism. The convective velocity (u) was obtained from the Navier-Stokes equations.

$$\nabla.(uC_{O_2}) = \nabla.(D\nabla C_{O_2}) \tag{5.1}$$

Here D is the diffusion coefficient of oxygen in water ($= 2.67 \times 10^{-9}$ m^2/s at 25 ^oC [25]). C_{O_2} is the dissolved oxygen concentration in water. The inlet boundary condition to the microchannel was set at a constant concentration value. If otherwise not stated, the inlet concentration is $C_{O_2}|_{(x=0)} = 0$, representing deoxygenated solutions in the experiments. No-flux boundary conditions ($\partial C_{O_2}/\partial y = 0$) were applied at the solid microchannel walls (at each L_s at $y = 0$ and the upper wall at $y = \mathrm{H}$) as the silicon microchannel walls are not permeable to oxygen.

The mass transfer boundary conditions at the bubble surfaces represent the gas dissolution mechanism at the gas-liquid interface that determines the rate of gas absorption by the liquid. Two different boundary conditions along the gas protrusions were examined as described below. (Fig. 5.2)

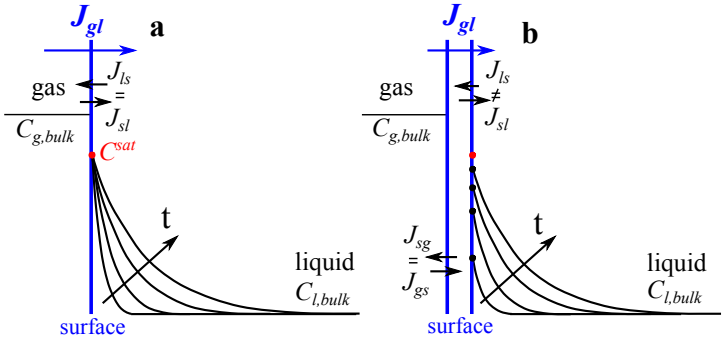

Figure 5.2: Schematic illustration of the applied boundary conditions and the effects of interface resistances on the concentration profiles in the presence of liquid flow (a) The phase equilibrium state where the interface liquid concentration is fixed at the saturation value given by Henry's Law (•) The time (t) evolution results in increasing boundary layer thicknesses. (b) The non-equilibrium state where the interface liquid concentrations (•) are determined by the instantaneous exchange rates of absorped and desorped molecules at the surface liquid boundary (s-l). The time (t) evolution results in increasing boundary layer thicknesses and increasing interface concentrations approaching saturation value. In (a-b) the mass transfer resistances in the gas phase are neglected.

5.3.2 Mass Transfer Boundary Conditions

The mass transfer resistance across a gas-liquid interface is investigated in many previous theoretical studies. [16–25] The surface resistances are commonly described at phase-equilibrium conditions. Higbie's penetration theory [19] and the two film-penetration theory [20] are among the well-known mathematical models. It is important to note that these theories consider equilibrium conditions at the interface. The net exchange rate of absorbed and desorbed species at the surface determines the amount of the accumulated species at the interface and thereby the interface concentration. Under equilibrium conditions, the amount of accumulated species

is at a maximum value given by the solubility limit. (Fig. 5.2a) For gas dissolution under phase-equilibrium conditions, the liquid interface concentration is described by Henry's Law. [6]

The mass transfer resistance at the interfaces has been investigated also for dynamical non-equilibrium conditions in previous theoretical and analytical studies using kinetic and thermodynamic approaches. [22–25] In kinetic interface models, the net exchange rate at the interface is described by Hertz-Knudsen equation where mass accommodation (condensation) coefficients are used as fitting parameters, estimating the fraction of molecules transfered to the liquid phase upon collisions on the surface. [22, 23]

Besides the kinetic approaches, a statistical rate theory (SRT) is suggested to predict the instantaneous rate of interfacial molecular transport. [24, 25] In SRT the gas-liquid boundary is described to consist of two interfaces; gas-surface interface and surface-liquid interface. (Fig. 5.2b) The molecular distributions in each phase (bulk gas, surface, and bulk liquid) are related to thermodynamic properties using Boltzmann definition of entropy. The transition probability of molecules from one phase to an other is derived via a first order perturbation analysis of Schrödinger equation. The calculated transition probability of gaseous species from the bulk gas phase to the bulk liquid phase has been used in approximating the instantaneous non-equilibrium exchange rate of absorbed and desorbed molecules at the surfaces. For long contacting times, the SRT predicts equilibrium exchange rates and equilibrium interface concentrations at the saturation value. [57] The SRT has been employed in various experimental studies [25–30] as the dynamical surface transport is described in terms of only physical and thermodynamic properties of the system without fitting parameters.

The theoretical models [16–25] for interfaces indicate that on convection enhanced hybrid substrates with induced hydrodynamic slippage, the mass transfer resistance of gas dissolution at the phase boundary can become the rate limiting step at short contacting times of liquid with bubbles. Therefore in the numerical simulations, the dynamics of interfacial mass transfer at curved oxygen microbubbles are studied considering (i) phase-equilibrium state (Fig. 5.2a) and (ii) non-equilibrium state (Fig. 5.2b). The mass transfer resistance at the interfaces is presumed to be a function

of temperature, local pressures, the axial location along the microchannel (x), and the interface concentrations of both gas and liquid phases. To best describe such dynamical mass transfer resistances at the bubble surfaces, a non-equilibrium based statistical rate theory [25] was adopted to the presented bubble mattresses. Non-equilibrium exchange rates at the gas-liquid interfaces can be estimated by using the local thermodynamic properties at the bubble surfaces with the aid of SRT.

Firstly, the saturation concentration of oxygen in water is applied as boundary conditions at the bubble surfaces in the phase-equilibrium based simulations. (Fig. 5.2a) At equilibrium conditions, the saturation value of the dissolved oxygen concentration at the interface ${C_{O_2}}^i$ is proportional to its partial pressure P_{O_2} and described by Henry's Law [6]

$$ {C_{O_2}}^i = {C_{O_2}}^{sat} = \frac{P_{O_2}}{K_H} \tag{5.2} $$

where K_H is the Henry's law constant given as $K_H = 7.7 \times 10^7$ Pa.l/mol at 25 ^oC [1] and ${C_{O_2}}^{sat}$ is the saturation concentration of oxygen in water. For pure oxygen bubbles, the dissolved oxygen concentration at the interface is calculated to be ${C_{O_2}}^i = {C_{O_2}}^{sat} = 1.3$ mol/m^3 at 1 atm and 25 ^oC.

Secondly, the rate of molecular transport between the surface phase and the bulk liquid phase is predicted by SRT and applied as flux boundary conditions along the gas protrusions (coinciding each L_g at $y = 0$) in the non-equilibrium based simulations, . According to SRT, this instantaneous molecular rate of transport between the phases is described as

$$ {J_{O_2}}^s = K_{sl} \left(\frac{{C_{O_2}}^{sat}}{{C_{O_2}}^i} - \frac{{C_{O_2}}^i}{{C_{O_2}}^{sat}} \right) \tag{5.3} $$

where ${C_{O_2}}^{sat}$ is the fixed equilibrium concentration of the dissolved oxygen, hence the solubility at the given temperature and pressure. ${C_{O_2}}^i$ is the interface concentration of oxygen in the liquid phase. At the bubble surface, concentration is a function of axial x location and to some extent

the bubble protrusion depth into liquid in y direction. K_{sl} $(moles/m^2 s)$ is the equilibrium oxygen exchange rate between bubble surface and the liquid phase and has a constant value for a system with given thermodynamic properties.

$$K_{sl} = \frac{{P_w}^g {C_w}^l {P_{O_2}}^g \pi r^3}{K_{H'}\sqrt{2\pi m k T}} \tag{5.4}$$

where ${P_w}^g$ is the partial pressure of water in the gaseous phase, which is the vapor pressure of the flowing water. ${P_{O_2}}^g$ is the partial pressure of oxygen in the gaseous phase and can be written as ${P_{O_2}}^g = P - {P_w}^g$ where P is the total pressure at the bubble surface. ${C_w}^l$ is the concentration of water in the liquid phase, which is 55.2 M at the experimental conditions. Here, r and m are the radius and molecular mass of oxygen gas molecule, k is the Boltzmann constant, and T is the temperature. $K_{H'}$ is the pressure-based Henry's law constant, given as 4.85×10^9 Pa at 25 ^oC. [1]

Without any fitting parameters, the expressions given in equations 5.3 are implemented as boundary conditions defining the oxygen flux at the bubble surfaces to study. It is important to note here that for longer contacting times, the interface concentration approaches the saturation value (${C_{O_2}}^i \rightarrow {C_{O_2}}^{sat}$), the rate of transport between phases (${J_{O_2}}^s$) vanishes, which is indicative of equilibrium conditions, *i.e.* a constant concentration, at the bubble surface.

5.4 Results and Discussion

5.4.1 FLIM Measurements

Oxygen is reported elsewhere [43] to be an effective collisional dynamic quencher of RTDP and its effect on RTDP fluorescence decay is described by the Stern-Volmer equation (5.5)

$$\frac{I_o}{I} = \frac{\tau_o}{\tau} = 1 + K_q C_{O_2} \tag{5.5}$$

where I_o and τ_o are the fluorescent intensity and the lifetime of unquenched RTDP at oxygen-free conditions, respectively. I and τ are the fluorescent intensity and the lifetime of RTDP for an arbitrary oxygen concentration of the solution. K_q is the Stern-Volmer constant. In previous studies, the fluorescence intensity and lifetime of RTDP was calibrated as a function oxygen concentration and linear relations were reported in agreement with the Stern-Volmer relation. [2, 44–48, 50] K_q values were reported in the range of 2.1 to 2.7 $\times 10^{-3}$ $\mu \mathrm{M}^{-1}$. [44–46] In most of these studies, the oxygen concentrations were in the physiologically attractive range from oxygen-free to air saturated solutions. The linear response of RTDP consistent with Stern-Volmer equation was also shown in the entire range of oxygen up to oxygen saturation concentration. [49, 50] In this study, based on the standard measurements for oxygen-free, aerated and oxygen-saturated aqueous solutions, the experimental K_q is calculated to be 1.9 $\times 10^{-3}$ $\mu \mathrm{M}^{-1}$, consistent with the literature findings. [44–46]

5.5 Rate of O_2 Absorption

During the mass transfer experiments, oxygen gas microbubbles were established at the boundary of the microchannels. (Fig. 5.1b and 5.3) The lifetime of RTDP across the liquid side microchannel height ($0 \leq y \leq \mathrm{H}$) was measured at different axial locations x. (Fig. 5.1b and 5.3) The bubble interface profiles and locations were experimentally determined by locating the minimum lifetime data measured near the hybrid wall. The bubble profiles were also calculated by circular arc estimation and depicted by the dashed lines in Figures 5.1b and 5.3. The good agreement between the measured and the calculated interface profiles was further confirmed by superimposing the measured lifetime fields on the bright field microscopy reference images acquired. (Fig. 5.1b) Figures 5.3a-c show the successive lifetime fields measured with FLIM at different axial locations along the same microchannel embedded with microbubbles $\theta = 43^o \pm 2^o$. Figure 5.3 reveals that the diffusion layer thickness of oxygen increases as the water flows further downstream in the microchannel. In Figure 5.3c, the diffusion layer is ~ 23 % of the microchannel height H, and does not spread

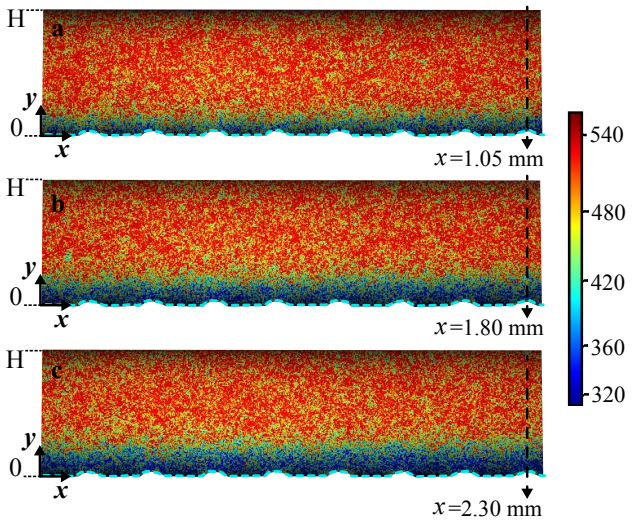

Figure 5.3: Successive lifetime fields in axial position x. Quantitative visualization of increasing boundary layer thickness along downstream flow with Q_w = 45μl/min at (a) 0.7 $\lesssim$ x $\lesssim$ 1.1 (b) 1.4 $\lesssim$ x $\lesssim$ 1.8 (c) 1.9 $\lesssim$ x $\lesssim$ 2.3. Here θ = $43^o \pm 2^o$ and φ = 0.38 In (a-c) the flow direction is from left to right. The color bar refers to the lifetime, which is given in nanoseconds.

further into the microchannel due to a relatively large Reynolds number $Re = 7.5$.

From the lifetime fields as shown in Figure 5.3, the dissolved oxygen concentration gradients were obtained by correlating the lifetime data by equation (5.5). When processing the data, no filtering or smoothing was applied to the measured lifetime fields. Due to the scattering of the experimental lifetime data, the obtained oxygen concentration values were averaged over the bubble surfaces. (over ~ 30 pixels in x, equivalent to L_g) The presented results are the average of independent experiments performed at the same operating fluidic settings. The statistical error bars are calculated from these reproducibility experiments.

The SRT based simulations performed at the same experimental settings (Fig. 5.1c) reveal an oxygen diffusion thickness of ~ 25 μm from the hybrid wall ($y = 0$) across the channel height in y direction, in a good agreement with the experiment shown in Fig. 5.1b and 5.3c.

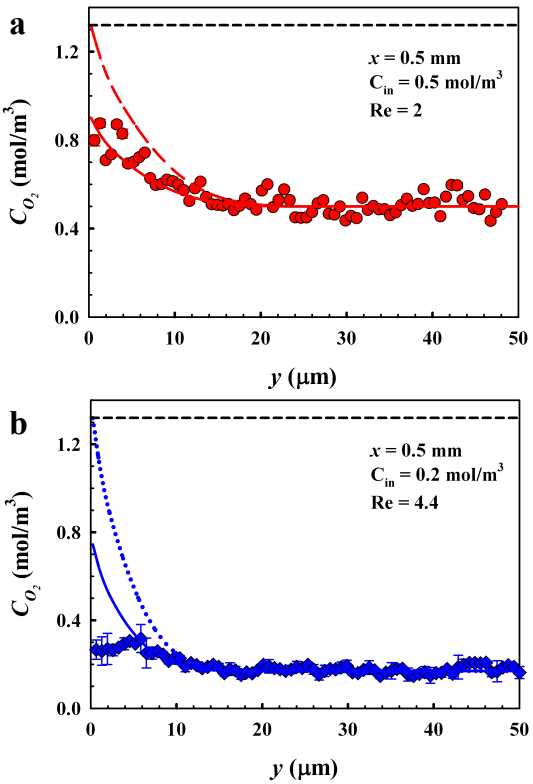

Figure 5.4: Experimental and numerical local dissolved oxygen profiles (a) For $Re = 2.2$ when the inlet oxygen concentration is 0.5 mol/m^3 (b) For $Re = 4$ when the inlet oxygen concentration is 0.2 mol/m^3. In (a-b), symbols represent the experimental results obtained by FLIM, the color solid lines represent the numerical results solved with SRT, the color dashed lines represent the numerical results solved using Henry's law. Here the microchannel height H = 50 μm, $\theta = 2^o \pm 1^o$ and $\varphi = 0.54$. The black dashed lines depict the equilibrium saturation value of oxygen in water.

Figure 5.4 shows the dissolved oxygen concentration gradients across the microchannel height, with respect to y direction normal to the bubble surfaces ($y = 0$). The experimental and numerical results are obtained at $x = 0.5$ mm for $Re = 2$ (Fig. 5.4a) and $Re = 4.4$(Fig. 5.4b). The inlet O_2 concentrations are 0.5 and 0.2 mol/m^3 in Fig. 5.4a-b, respectively. The

experimental results are compared with numerical results obtained for phase-equilibrium based and SRT-based gas absorption. In Figure 5.4a when $Re = 2$, the experimental diffusion layer thickness is ~ 18 μm, consistent with the numerical results. In Fig. 5.4a, the bubbles are nearly flat ($\theta = 2^o \pm 1^o$) and surface porosity φ is 0.54. At the bubble interface (y ~ 0.3 μm), the oxygen concentration is measured to be ~ 0.9 mol/m^3, consistent with the SRT boundary condition numerical results. Whereas the interface O_2 concentration predicted by phase-equilibrium based simulations converges to the saturation value 1.3 mol/m^3 as imposed by the Henry's law. The experimental oxygen concentration profile shown in Fig. 5.4b when $Re = 4.4$ also reveals a slower oxygen transport compared to that of computed for phase-equilibrium state at the bubble surfaces. The experiments are in good agreement with SRT based simulations when $y \gtrsim 4$ μm. However there is a sharp discrepancy between the measurements and both numerical results in the proximity of the bubble interfaces. The standard errors calculated close to the bubble surface is also larger compared to the remainder of the microchannel. The discrepancy in the measured and calculated values when $y \lesssim 4$ μm is still larger than the standard error margins. The deviation can be related to the systematic error in the FLIM measurements close to the gas-liquid interfaces.

In the FLIM measurements, the normalized fluorescence lifetime signal decreases from 1 (oxygen-free state) to ~ 0.3 (oxygen-saturated state), providing a signal level of ~ 0.7 in the entire oxygen concentration range. The noise level was measured as ~ 0.1, hence a signal to noise ratio of ~ 7. RTDP is reported to have a mono-exponential fluorescence decay in time [46, 50], thereby the Stern-Volmer equation can be used in correlating the lifetime data to oxygen concentrations. In FLIM, the lifetime data calculated by the phase shift or the amplitude demodulation of emitted signal does not differ for luminescent dyes with a mono-exponential decay in time. [43] Whereas, deviations were also reported for long lifetime probes as Ru-based complexes. [51] In the presented experiments, a difference between the phase shift τ_p and the demodulation τ_m lifetimes on the average of ~ 7 % is measured. Reduced signal-to-noise ratios and larger differences between τ_p and τ_m near microchannel walls and bubble interfaces were observed. These deviations can be attributed to optical distortions and reflection effects near interfaces [52–54], and the complex

quenching mechanisms of luminescent dyes. [51]

In one recent experimental work [54], the dissolved oxygen concentration fields were measured near air bubble surfaces in a stagnant liquid phase and optical distortions accompanied with reflection effects near the bubble surfaces were reported. The deviations near the bubble surfaces do not interfere with the results presented here as the experimental data obtained in the proximity of bubble interfaces $y \lesssim 10$ % of the microchannel height are not considered. Under flow conditions, oxygen mass transfer near bubble surfaces are encountered in turbulent regimes in laser-induced fluorescence studies where the same kind of optical distortion effects are reported. [52, 53, 55] Under laminar flow conditions, the mass transfer characteristics of gas dissolution from microbubbles with induced hydrodynamic slippage have not been studied so far.

Figures 5.5a-c represent the local oxygen concentration gradients obtained from the lifetime fields shown in Figures 5.3a-c which are successive measurements at different axial x positions in the microchannel during the same experiment. The local profiles are obtained at x positions coinciding the bubble surfaces that are indicated with dashed arrows in Fig. 5.3. Here the deoxygenated RTDP aqueous solution flows at a Reynolds number $Re = 7.5$. The oxygen concentration gradients are much steeper compared to those revealed for smaller Reynolds numbers in Fig. 5.4a-b. The trend of the experimental and numerical oxygen profiles are determined by convection-diffusion mechanism. Accordingly, a maximum concentration value is revealed near bubble surfaces, the oxygen concentrations within the boundary layer decrease and reach the constant inlet concentration value above the boundary layer thickness ($C_{O_{2-in}} = 0$). As can be clearly seen in Figures 5.5a and c, the effect of the microbubbles on the concentration profiles is damped when $y \gtrsim 25$ μm at $x = 1.05$ mm and when $y \gtrsim 35$ μm at $x = 2.30$ mm. Beyond the boundary layers, the oxygen concentration drops to the inlet bulk concentration value. These findings are consistent with previous studies [45, 49] reporting the local oxygen gradients resolved by in-situ FLIM measurements. In these studies, oxygen diffuses from an oxygen enriched liquid phase to an oxygen-free liquid phase, revealing a convection-diffusion type mass transfer characteristics as in this study.

The bubble interface position is $y \sim 3.8$ μm in Fig. 5.5 due to a large

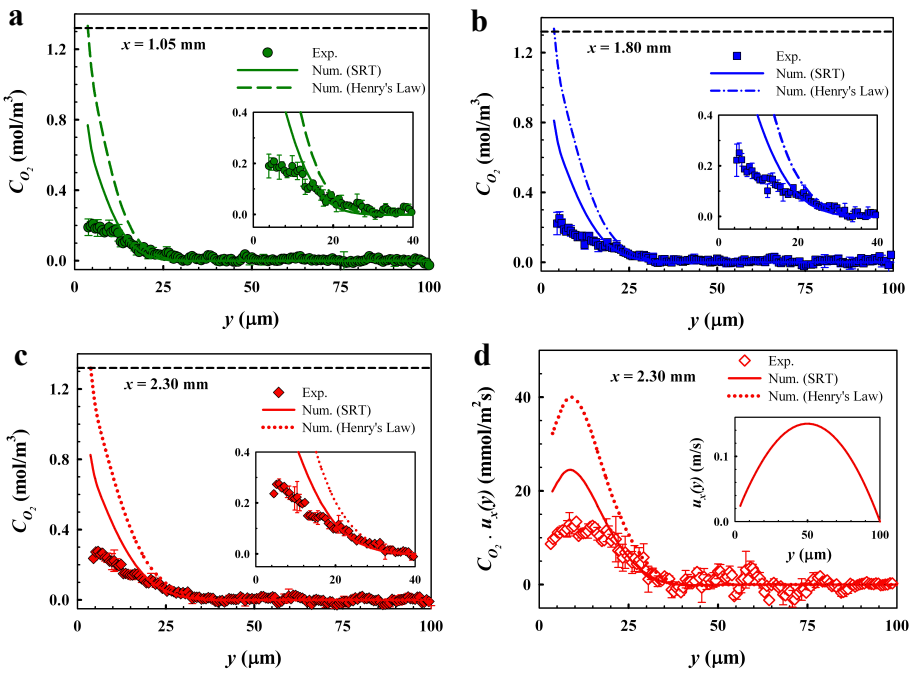

Figure 5.5: Successive local dissolved oxygen profiles at different axial x positions and local convective oxygen flux Local O_2 profile at $x = 1.05$ mm (a) at $x = 1.80$ mm (b) at $x = 2.30$ mm (c) Local convective J_{O_2} profile at $x = 2.30$ mm. The inset shows the parabolic velocity profile for the results in (a-c) obtained by simulations. In (a-d) symbols represent the experimental results obtained by FLIM, the color solid lines represent the numerical results solved with SRT, the color dashed lines represent the numerical results solved using Henry's law. Here the microchannel height H = 100 μm, $\theta = 43^o \pm 2^o$, $\varphi = 0.38$, $Re = 7.5$. The black dashed lines depict the equilibrium saturation value of oxygen in water.

protrusion angle $\theta = 43^o \pm 2^o$ of the bubbles into water stream. The FLIM measurements in Fig. 5.5 reveal very low concentrations near bubble interfaces when $y \lesssim 10$ μm, similar to those shown in Fig. 5.4 with even slightly larger discrepancies from the numerical results. Considering the oxygen concentration data when ~ 10 μm $\leq y \leq$ H, the measured oxygen concentration profiles are in a good agreement with the simulations performed with an incorporated mass transfer resistance at the gas-liquid interfaces

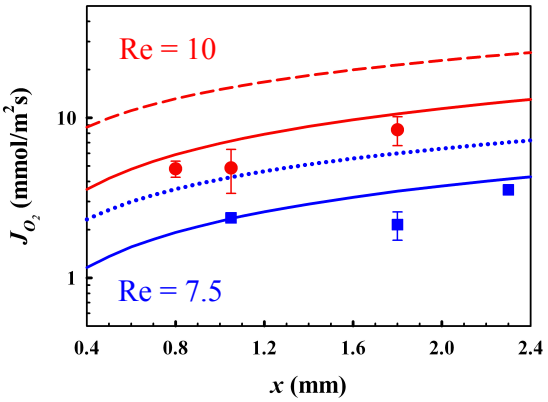

Figure 5.6: O_2 fluxes J_{O_2} as functions of axial x positions and Re obtained by FLIM measurements and numerical calculations. Red filled circles (•), the red solid line (———), and the red dashed line (- - -) indicate the experimental, the SRT-based numerical and equilibrium-based numerical results, respectively, for $Re = 10$ and $\theta = 35^o \pm 3^o$. Blue filled squares (■), the blue solid line (———) and the blue dotted line (.....) indicate the experimental, the SRT-based numerical and equilibrium-based numerical results, respectively, for $Re = 7.5$ and $\theta = 43^o \pm 2^o$. In (a) and (b) $\varphi = 0.38$.

by the aid of SRT. Whereas, the numerical results computed for a constant interface concentration at the solubility limit of oxygen in water predict steeper profiles and faster gas absorption than in the measurements. Due to a relatively large $Re = 7.5$, the water residence time within the hold-up volume of the microchannel embedded with the bubbles is as small as 96 ms. The inset in Figure 5.5d shows the numerical parabolic velocity profile in these set of experiments, revealing a slip velocity ~ 25 mm/s, consistent with the results shown in the previous chapters. [32] This slip velocity induces a very short contact time of water stream passing a single bubble interface. The exposure time of a slippery bubble surface to water is calculated to be ~ 830 μs. These short exposure times are insufficient for a gas-liquid phase equilibrium. These findings are indicative of an additional mass transfer resistance induced by the gas dissolution at the bubble surfaces at short exposure times on convection enhanced bubble mattress type geometries.

To further highlight the presented results indicative of interfacial mass transfer resistances, the local instantaneous convective flux distribution is presented in Fig. 5.5d. The concentration profile shown in Fig. 5.5c and its coupled velocity profile is multiplied to calculate the local flux. The local flux near the bubble surfaces have low values up to $y \approx 8$ μm due to the low local velocity in this region even though the dissolved oxygen concentrations are at their maximum values. The flux then increases to a peak value when 8 μm $\lesssim y \lesssim$ 11 μm. Above $y \approx 11$ μm, the local flux decreases with a slope mainly determined by the decrease in C_{O_2} to the zero bulk concentration towards the end of the diffusion layer thickness $y \approx 35$ μm. The differences in the experimental and numerical slopes are mainly attributed to concentration profiles, as the coupling velocity profile is unique at the given settings. Here the differences in the fluxes obtained by the measurements and phase-equilibrium based simulations are more pronounced.

The O_2 fluxes are determined by integration of the local flux profiles. Figure 5.6 reveals the O_2 fluxes obtained from the measurements, the simulations performed at phase equilibrium conditions on the bubble surfaces and the simulations incorporating an interfacial mass transfer resistance via SRT. The total convective fluxes are mainly determined by the area under the local flux curves when 11 μm $\lesssim y \lesssim$ 35 μm. In this region of interest, the experimental values are not hampered by the systematic error in the measurements. ($y \lesssim 0.1$H) The experimental oxygen fluxes revealed in Fig. 5.6 are in a good quantitative agreement with the ones computed by considering an additional gas dissolution resistance via the aid of SRT. The flux values calculated with the assumption of spontaneous phase-equilibrium state are higher, as in this case the interface dissolved oxygen concentration is at the maximum saturation value. The phase equilibrium flux obtained at $x = 1.05$ mm for $Re = 7.5$ is $\sim$ 1.8 times higher than the ones obtained from the measurements and the SRT-based numerics. Figure 5.6 reveals also the oxygen fluxes obtained at $Re = 10$. The differences are more pronounced for a higher Reynolds number $Re = 10$. The phase equilibrium flux obtained at $x = 1.05$ mm is $\sim$ 2.2 times higher than those obtained from the measurements and the SRT-based numerics. An increase in Re from 7.5 to 10, results in a decrease in water residence time within the hold-up volume of bubble mattress from 96 ms to 48 ms with

an increase in mean velocity. Furthermore for a higher Reynolds number $Re = 10$, the slip velocity at the hybrid wall ($y = 3$ μm for $\theta = 35^o \pm 3^o$) has a much higher value ~ 112 mm/s, thereby a much shorter exposure time ~ 180 μs of a slippery bubble surface to water stream compared to the exposure time ~ 830 μs for $Re = 7.5$. (Fig. 5.6) These findings show such exposure times lead to larger deviations from the equilibrium state between gas and liquid phases.

The experimental and gas dissolution resistance incorporated-numerical O_2 fluxes obtained at $x = 1.05$ mm for $Re = 7.5$ and $Re = 10$ are compared. The experimental flux value for $Re = 10$ is ~ 2.3 folds higher than that for $Re = 7.5$. In a good agreement with the measurements, the simulations predict ~ 3 folds higher flux value for $Re = 10$ compared to $Re = 7.5$. (Fig. 5.6) This slight increase in Reynolds number result in a larger decrease in exposure times due to a larger slip velocity near bubble surface, and thereby a decrease in the dissolved oxygen concentration at the interface. Nevertheless, this enhanced hydrodynamics result in enhanced convection, therefore an enhanced convective mass flux, as tripled in this case. Consistent with the literature findings [10, 38, 41, 56], the results presented here clearly demonstrate that the hydrodynamic slippage amplifies the interfacial mass transport on hybrid substrates consisting of liquid-solid and liquid-gas interfaces as such can be found in porous media and bubble mattress like geometries, even at very short contacting times.

5.6 Conclusions

The interfacial mass transport accompanied with hydrodynamic slippage at gas-liquid interfaces is studied in microfluidic devices allowing for the establishment of stable and controllable microbubbles at the boundary of microchannels dedicated for pressure-driven flow in a perpendicular direction. The fluidic configuration in these microfluidic devices allow for the investigation of gas absorption dynamics at curved gas-liquid interfaces. The local oxygen concentration fields resolved by FLIM measurements at short exposure times on the order of microseconds reveal slower gas absorption rates compared to those predicted by phase-equilibrium based simulations. Whereas the experimental results are in a good agreement with the numerical results obtained from the simulations considering an

additional mass transfer resistance during gas dissolution. The results presented here indicate that the equilibrium state may not be established at short contacting times. The obtained results also reveal that even at such short exposure times, the hydrodynamic slippage enhances the total mass flux driven by amplified flow throughput on bubble mattresses.

Bibliography

[1] Green DW (1984) *Perry's Chemical Engineers' Handbook*, (McGraw Hill).

[2] Adler M, Erickstad M, Gutierrez E, Groisman A (2012) Studies of bacterial aerotaxis in a microfluidic device. *Lab Chip* 12(22):4835-4847.

[3] Ungerböck B, Pohar A, Mayr T, Plazl I (2013) Online oxygen measurements inside a microreactor with modeling of transport phenomena. *Microfluid. Nanofluid.* 14(3-4):565-574.

[4] Geankoplis CJ (2003) *Transport Processes and Separation Process Principles*, (Prentice Hall).

[5] Gaddis ES (1999) Mass transfer in gas-liquid contactors. *Chem. Eng. Process.* 38(4-6):503-510.

[6] Henry W (1803) Experiments on the Quantity of Gases Absorbed by Water, at Different Temperatures, and under Different Pressures. *Philos. Trans. of the Royal Soc. London* 93:29-42 & 274-276.

[7] Karoor S, Sirkar KK (1993) Gas absorption studies in microporous hollow fibre membrane modules. *Ind. Eng. Chem. Res.* 32:674-684.

[8] de Jong J, Verheijden PW, Lammertink RGH, Wessling M (2008) Generation of local concentration gradients by gas-liquid contacting. *Anal. Chem.* 80(9):3190-3197.

[9] de Jong J, Lammertink RGH, Wessling M (2006) Membranes and microfluidics: a review. *Lab Chip* 6(9):1125-1139.

[10] Karatay E, Lammertink RGH (2012) Oxygenation by a superhydrophobic slip G/L contactor. *Lab Chip* 12:2922-2929.

[11] Ho WSW, Sirkar KK (1992) *Membrane Handbook, Volume 1, Ch. 46*, (Chapman and Hall).

[12] Mavroudi M, Kaldis SP, Sakellaropoulos GP (2006) A study of mass transfer resistance in membrane gas-liquid contacting processes. *J. Mem. Sci.* 272(1-2):103-115.

[13] Zhang HY, Wang R, Liang DT, Tay JH (2008) Theoretical and experimental studies of membrane wetting in the membrane gas-liquid contacting process for CO_2 absorption. *J. Mem. Sci.* 308(1-2):162-170.

[14] Dindore VY, Brilman DWF, Versteeg GF (2005) Modelling of cross-flow membrane contactors: physical mass transfer processes. *J. Mem. Sci.* 251(1-2):209-222.

[15] Kreulen H, Smolders CA, Versteeg GF, van Swaaij WPM (1993) Microporous hollow fibre membrane modules as gas-liquid contactors. Part 1. Physical mass transfer processes. *J. Mem. Sci.* 78:197-216.

[16] van Elk EP, Borman PC, Kuipers JAM, Versteeg GF (2000) Modelling of gasliquid reactors: Implementation of the penetration model in dynamic modelling of gas-liquid processes with the presence of a liquid bulk. *Chem. Eng. J.* 76(3):223-237.

[17] van Elk EP, Knaap MC, Versteeg GF (2007) Application of the Penetration Theory for Gas-Liquid Mass Transfer Without Liquid Bulk: Differences with Systems with a Bulk. *Chem. Eng. Res. Des.* 85(4):516-524.

[18] Whitman WG (1923) Preliminary experimental confirmation of the two film theory of gas absorption. *Chem. Metall. Eng.* 29:146-148.

[19] Higbie R (1935) The rate of absorption of a pure gas into a still liquid during short periods of exposure. *Trans. Am. Inst. Chem. Eng.* 35:36-60.

[20] Toor HL, Marchello JM (1958) Film penetration model for mass transfer and heat transfer. *AIChE* 4:97-101.

[21] Danckwerts PV (1951) Significance of liquid film coefficients in gas absorption. *Ind. Eng. Chem.* 43:1460-1467.

[22] Huthwelker T, Peter T (1996) Analytical description of gas transport across an interface with coupled diffusion in two phases. *J. Chem. Phys.* 105:1661-1667.

[23] Monchick L, Blackmore R (1988) A variation calculation of the rate of evaporation of small droplets. *J. Aerosol Sci.* 19(3):273-286.

[24] Ward CA, Findlay RD, Rizk M (1982) Statistical rate theory of interfacial transport. I. Theoretical development. *J. Chem. Phys.* 76(11):5599-5605.

[25] Ward CA, Rizk M, Tucker AS (1982) Statistical rate theory of interfacial transport. II. Rate of isothermal bubble evolution in a liquid-gas solution. *J. Chem. Phys.* 76(11):5606-5614.

[26] Rahimi P, Ward CA (2004) Effect of pressure on the rate of evaporation from capillaries: statistical rate theory approach. *Int. J. Heat Mass Tran.* 47:877âĂŞ886.

[27] Holyst et al. (2013) Evaporation of freely suspended single droplets: experimental, theoretical and computational simulations. *Rep. Prog. Phys.* 76:034601.

[28] Rahimi P, Ward CA (2005) Kinetics of Evaporation: Statistical Rate Theory Approach. *Int. J. Thermodynamics* 8(1):1-14.

[29] Badam VK, Kumar V, Durst F, Danov K (2007) Experimental and theoretical investigations on interfacial temperature jumps during evaporation. *Exp. Thermal Fluid Sci.* 32:276-292.

[30] Elliott JAW, Ward CA (1997) Statistical rate theory description of beam-dosing adsorption kinetics. *J. Chem. Phys.* 106(13):5667-5676.

[31] Tsai P et al. (2009) Quantifying effective slip length over micropatterned hydrophobic surfaces. *Phys. Fluids* 21:112002.

[32] Karatay E et al. (2013) Control of slippage with tunable bubble mattresses. *Proc. Natl. Acad. Sci. USA* 110(21):8422-8426.

[33] Byun D, Kim J, Ko HS, Park HC (2008) Direct measurement of slip flows in superhydrophobic microchannels with transverse grooves. *Phys. Fluids* 20:113601.

[34] Teo CJ, Khoo BC (2010) Flow past superhydrophobic surfaces containing longitudinal grooves: effects of interface curvature. *Micro-Nanofluidics* 9:499-511.

[35] Ng C, Wang CY (2011) Effective slip for Stokes flow over a surface patterned with two- or three-dimensional protrusions. *Fluid Dyn. Res.* 43:065504.

[36] Schmieschek S, Belyaev AV, Harting J, Vinogradova OI (2012) Tensorial slip of superhydrophobic channels. *Phys. Rev. E* 85:016324.

[37] Steinberger A, Cottin-Bizonne C, Kleimann P, Charlaix E (2007) High firction on a bubble mattress. *Nature Mater.* 6:665-668.

[38] Bocquet L, Barrat J-L (2007) Flow boundary conditions from nano- to micro-scales. *Soft Matter* 3:685-693.

[39] Hyväluoma J, Harting J (2008) Slip Flow Over Structured Surfaces with Entrapped Microbubbles. *Phys. Rev. Lett.* 100:246001.

[40] Bocquet L, Lauga E (2011) A smooth future? *Nature Mater.* 10:334-337.

[41] Ajdari A, Lydéric B (2006) Giant amplification of interfacially driven transport by hydrodynamic slip: diffusio-osmosis and beyond. *Phys. Rev. Lett.* 96(18):186102.

[42] Arayanarakool R, Shui L, van den Berg A, Eijkel JCT (2011) A new method of UV-patternable hydrophobization of micro- and nanofluidic networks. *Lab Chip* 11(24):4260-4266.

[43] Berezin M, Achilefu S (2010) Fluorescence Lifetime Measurements and Biological Imaging. *Chem. Rev.* 110(5):2641-2684.

[44] Polinkovsky M, Gutierrez E, Levchenko A, Groisman A (2009) Fine temporal control of the medium gas content and acidity and on-chip generation of series of oxygen concentrations for cell cultures. *Lab Chip* 9(8):1073-1084.

[45] Abbyad P et al. (2010) Sickling of red blood cells through rapid oxygen exchange in microfluidic drops. *Lab Chip* 10(19):2505-2512.

[46] Gerritsen HC, Sanders R, Draaijer A, Ince C, Levine YK (1997) Fluorescence lifetime imaging of oxygen in living cells. *J. Fluoresc.* 7(1):11-15.

[47] Mehta G et al. (2007) Quantitative measurement and control of oxygen levels in microfluidic poly(dimethylsiloxane) bioreactors during cell culture. *Biomed. Microdevices* 9:123-134.

[48] Sud D, Zhong W, Beer DG, Mycek M-A (2006) Time-resolved optical imaging provides a molecular snapshot of altered metabolic function in living human cancer cell models. *Optics Express* 14(10):4412-4426.

[49] Chen J, Kim HD, Kim KC (2013) Measurement of dissolved oxygen diffusion coefficient in a microchannel using UV-LED induced fluorescence method. *Microfluid. Nanofluid.* 14:541-550.

[50] Morris KJ et al. (2007) Luminescence Lifetime Standards for the Nanosecond to Microsecond Range and Oxygen Quenching of Ruthenium(II) Complexes. *Anal. Chem.* 79:9310-9314.

[51] Choi H et al. (2012) 3D-resolved fluorescence and phosphorescence lifetime imaging using temporal focusing widefield two-photon excitation. *Optics Express* 20(24):26219-26235.

[52] Walker JW, Peirson WL (2008) Measurement of gas transfer across wind-forced wavy airâĂŞwater interfaces using laser-induced fluorescence. *Exp. Fluids* 44:249-259.

[53] Woodrow PT, Duke SR (2001) Laser-Induced Fluorescence Studies of Oxygen Transfer Across Unsheared Flat and Wavy Air-Water Interfaces. *Ind. Eng. Chem. Res.* 40:1985-1995.

[54] Roy S, Duke SR (2000) Laser induced fluorescence measurements of dissolved oxygen concentration fields near air bubble surfaces. *Rev. Sci. Instrum.* 71(9):3494-3501.

[55] Jirka GH, Herlina H, Niepelt A (2010) Gas transfer at the air-water interface: experiments with different turbulence forcing mechanisms. *Exp. Fluids* 49:319-327.

[56] Yeh HM, Cheng TW (1999) Analysis of the slip effect on the permeate flux in membrane ultrafiltration. *J. Memb. Sci.* 154(1):41-51.

[57] Ward CA (1977) The rate of gas absorption at a liquid interface. *J. Chem. Phys.* 67(1):229-235.

6

Ion Selective Membranes in Microfluidics

The integration of ion selective interfaces with tunable ionic properties and controllable geometries into microfluidic devices is of paramount importance for various applications aiming at charge based separations, ranging from the conventional electrodialysis in micro-scale to the new electrokinetic separations based on ion concentration polarization at intensive currents. Implementing ion selective substrates having high ion exchange capacity in precisely defined microchannels is rather challenging. In this study, hydrogel based perm-selective anion exchange membranes are locally fabricated in confined microchannels by selective photo-induced methods. The effects of membrane chemistry on the swelling and charge properties are investigated in detail to obtain optimal membrane formulation for microfluidic preparation. The developed methodology allows for the in-situ fabrication of tailored hydrogel based membranes in highly confined microchannel geometries. The local ion transport across the in-situ prepared anion exchange membranes were studied via passive diffusion experiments and under external DC bias. The obtained experimental findings indicate the perm-selectivity of the in-situ prepared microfluidic membranes that is of primary importance in many charged based separations.

6.1 Introduction

Integration of optimal ion selective interfaces in microfluidics is highly essential for both applied and fundamental aspects of ion concentration polarization (ICP) which is a significant fundamental phenomenon encountered in many electro-chemical processes. [1, 2] In micro scale systems, a large number of applications such as electrodialysis [3], water desalination [4], high-focusing of proteins and (biological) sample preconcentration [5–8] require charge selective boundaries and operate under ICP principle. The performances of these processes are bound to the formation of concentration gradients which can potentially be controlled via the charge selective boundaries.

Ion exchange membranes (IEM) have been extensively studied and widely used in electrically driven membrane processes such as electrodialysis. [9, 10] Ion exchange membranes are electrically conductive, ion selective, nanoporous membranes where charged chemical groups are attached to the polymer backbone of the membrane material. These fixed charge groups partially or completely exclude ions of the same charge from the membrane. This implies that an anion exchange membrane with fixed positive groups excludes positive ions but is freely permeable to negatively charged ions. A wide variety of ion exchange membrane chemistries has been developed and tailored for specific applications and equipment used. [9, 10] Ion exchange membranes are well-established and commercialized for charge based separations in macro-scale.

Integrating IEMs in microfluidic devices is quite advantageous for charge based separations due to their versatility, robustness and larger ion exchange area compared to that of micro/nanochannel interfaces. Few recent experimental studies [3, 11, 12] have suggested integrating IEM to micro-devices for charged based separations. In the suggested micro-devices [3, 11, 12], separate components of the device (lab-on-chip substrates and IEM) are assembled together such that the IEMs are sandwiched in between microchannels. This methodology allows for the use of well-characterized IEMs in microfluidics, whereas fluid leakage is often problematic in sandwich type configurations. [3]

Another method to integrate IEMs in microfluidics is by fabrication of the IEMs inside the microfluidic devices from the base solutions of the

membrane materials. The ion exchange polymeric membranes are typically prepared from the base solutions of electrically conductive polymers by solvent evaporation. [9, 10] This method requires thermal treatment and has been used in a recent experimental study in microfluidics. [4] The PDMS nanochannels were filled with Nafion solution, a commercial polymeric ion exchange membrane material that was thermally cured. Besides thermal treatment, another highly promising IEM preparation method in microfluidic devices is photo-treatment. IEMs can be prepared by photo-polymerization of ultra violet (UV) light sensitive charged monomer solutions in microchannels, and by further photo-crosslinking of these polymers. [13–15] Fabrication of IEMs by photo-treatment is a simple and cheap method allowing for integrating versatile, tailor-made, robust ion selective interfaces in microfluidic devices with precisely defined interface geometries that can be easily patterned locally by selective UV illumination. However, in-situ photo-polymerization of ion selective membranes in confined microchannels has not been investigated so far. Electrically conductive photo-polymerized films of charged monomers have been investigated in micro scale devices in several applications such as salt bridge electrodes [8, 16–18], microfluidic based diodes [19], transistors [20], microscale pH regulation [6], and high focusing of proteins [13, 21].

In this chapter, the in-situ photo-induced fabrication of ion selective membranes that are locally photo-patterned in the microchannels by selective UV irradiation is presented. The membrane preparation parameters concerning both the chemical composition of the base membrane material and the fabrication protocols in the microfluidic devices are studied in detail for obtaining tunable and controllable ion selective interfaces.

6.2 Experimental Methods

6.2.1 Membrane Preparation

Materials

The positively charged monomer, diallyldimethylammonium chloride (DADMAC), was purchased as 65 w % aqueous solution. (Sigma-Aldrich) Polyethylene glycol (PEG), 2-hydroxyethyl methacrylate (HEMA) and 1-vinyl-2-pyrrolidinone (NVP) were used as the uncharged monomers in the

membrane formulations. (Sigma-Aldrich) For all types of membranes produced, Irgacure 2959 (BASF) and N,N'-methylenebisacrylamide (NbisA) were used as photoinitiator and crosslinking agent, respectively. All the chemicals are used as purchased without any further purification. The solvent of all types of membranes produced was Milli-Q grade deionized water and aqueous NaCl solutions were used as electrolyte solutions at different ionic strengths.

Membrane Preparation Methodology

All the membranes presented were prepared by free radical initiated photopolymerization of the monomers in the base membrane solutions resulting in linear polymer chains and further photo-crosslinking of these polymer chains by the aid of the crosslinking agent.

Pure DADMAC and binary component membranes were produced from the base membrane solutions of pure DADMAC and blends of DADMAC/uncharged monomer, respectively. Table 6.1 shows the composition of binary component blend membranes. The base membrane solutions were prepared sequentially by (i) dissolution of the monomers in water at room temperature, (ii) addition of the photoinitiator Irgacure 2959 and magnetic stirring at 50^o for ~ 1 hour, (iii) addition of the crosslinker NbisA and magnetic stirring until a clear solution is obtained. The membrane solutions were protected from light, and used immediately without storing.

The same homogeneous membrane solutions were used to fabricate batch membranes and microfluidic membranes. The batch membranes were dropcast in petri dishes with casting thickness of ~ 2.3 mm. These films were illuminated by a UV light source having a light intensity of 30 Watt/cm^2 at 365 nm for 100 seconds. (Dr. Gröbel UV-Point Source HP-120) After the UV irradiation, the films were stored in Milli-Q water or NaCl solutions at different ionic strengths for equilibration.

6.2.2 Characterization of Membranes

The chemical compositions of the membranes were confirmed by Attenuated Total Reflectance Fourier Transform Spectroscopy (ATR-FTIR, Bruker

Table 6.1: The compositions of the prepared membranes labelled as DADMAC[a]/NVP[b](x/y) NbisA[c] z%, where x/y is the molar ratio of DADMAC/NVP and z is the molar percentage of NbisA with respect to total moles of the monomer(s). In all compositions, the photoinitiator Irgacure 2959 is 2 w % of the total mass of the solution.

Sample	DADMAC[a] mol%	NVP[b] mol%	NbisA[c] z mol%
DADMAC/NVP(1/0) NbisA z%	100	0	3.2/5
DADMAC/NVP(3/1) NbisA z%	75	25	3.2/5/10
DADMAC/NVP(1/1) NbisA z%	50	50	3.2/5/10
DADMAC/NVP(1/3) NbisA z%	25	75	3.2/5/10/13
DADMAC/NVP(0/1) NbisA z%	0	100	3.2/5/10/13

[a] positively charged monomer

[b] uncharged monomer

[c] crosslinking agent

Alpha-P). The swelling behavior of the fabricated membranes was studied by controlled swelling experiments in different ionic strength aqueous solutions. The sample mass was obtained immediately after the UV illumination (m_{UV}), after 24 hours of equilibration in the excess amount of aqueous solutions (m_{s}), and after 48 hours of drying at room temperature in a vacuum oven (m_{dry}). Based on these measurements, the swelling degree (SD), the apparent swelling degree ($\mathrm{SD}^{\mathrm{app}}$) and the gel ratio values were obtained. The swelling degree and the apparent swelling degree are defined as

$$\mathrm{SD}(\%) = \frac{m_{\mathrm{s}} - m_{\mathrm{dry}}}{m_{\mathrm{dry}}} \cdot 100\% \tag{6.1}$$

$$\mathrm{SD}^{\mathrm{app}}(\%) = \frac{m_{\mathrm{s}} - m_{\mathrm{UV}}}{m_{\mathrm{UV}}} \cdot 100\% \tag{6.2}$$

The gel ratio (GR), which is a typical measure of the chemical conversion, is calculated by

$$\mathrm{GR} = \frac{m_{\mathrm{UV}} - m_{\mathrm{H_2O}} - m_{\mathrm{photo}} - m_{\mathrm{dry}}}{m_{\mathrm{dry}}} \tag{6.3}$$

where $m_{\mathrm{H_2O}}$ and m_{photo} are the mass of the water and photoiniator in the base membrane solutions.

6.2.3 Microfluidic Setup

Microfluidic Devices

Silicon microchannels were fabricated by photolithography followed by deep reactive ion etching process. An electrical insulation layer of ~ 600 nm thick silicon dioxide was grown by thermal oxidation on the silicon substrates including the etched microchannels to prevent the electrical short via the semiconductor silicon. The silicon dioxide coated microchannels were sealed by glass substrates containing metal deposited microelectrodes by anodic bonding. The electrodes were fabricated by standard photolithography followed by metal sputtering of first titanium as as an adhesion layer and then platinum as the inert electrode material and finally metal lift-off in acetone under ultrasound.

In-situ Membrane Preparation

The membranes were fabricated on the region of interest in the microfluidic devices using the same base membrane solution used for batch membrane preparation. The microchannels were filled with the base solution by a syringe pump. The UV irradiation required for photo-polymerization and photo-crosslinking was supplied from the glass side of the micro-devices. (Dr. Gröbel UV-Point Source HP-120) The fiber optic cable was attached ~ 5 cm above the micro-devices. A patterned photo-mask was used in the selective irradiation of the region of interest with UV light. Figure 6.1 represents the procedure for selective UV illumination by photo-masking. The photo-mask is chromium coated and only a bare glass region is transparent to UV light, coinciding the dedicated microchannel for membrane preparation when aligned in the chip holder. (Fig. 6.1c) The photo-mask is aligned and the membrane solution in the dedicated area is exposed to

UV light for 100 s. The unexposed residual monomer solutions were removed by flowing Milli-Q water through the main fluidic microchannels by a syringe pump. After the cleaning step, the Milli-Q water was replaced by 1 mM NaCl solution and the ion selective membrane integrated micro-device was equilibrated with 1 mM NaCl solution and stored for further use.

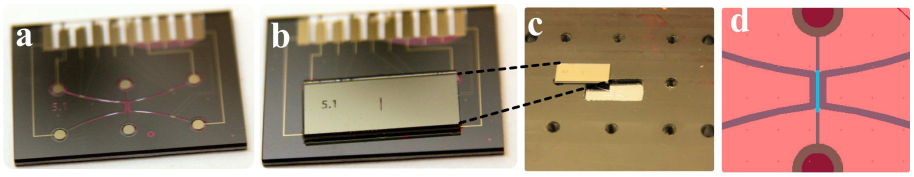

Figure 6.1: Selective UV irradiation procedure by photo-masking. (a) Optical image of a representative microfluidic device. Here the glass side is top. (b) Aligning the photo-mask and the microfluidic device. (c) The base part of the chip holder, where the glass side of the micro-device can be seen in the middle region used for optical access. (d) A schematic representation of photo-masked device, where the chromium coated part and the transparent glass part of the mask is depicted in red and blue colors, representatively.

Electronic Setup and Impedance Measurements

Integrated electrode contact pads were fabricated on the microfluidic devices for electrical connections. Spring-loaded connection pins assembled in the Delrin chip holder were used to connect both the conductivity measurement electrodes and the voltage delivery electrodes to a printed circuit board (PCB) attached on the chip holder cap. (TCO†) The PCB contains deposited metal wires for electrical connections to (i) a power supply unit for supplying a potential gradient across the membrane (Et System electronic GmbH LAB/SL120 MOD/AI) and (ii) an impedance analyzer unit for conductivity detection.

On each microfluidic device, three pairs of conductivity measurement electrodes were fabricated for measuring the resistances of the electrolyte solutions in different microchannels (feed and permeate side) and at different locations in a microchannel before and after contacting with the ion

† Techno Centrum voor Onderwijs en Onderzoek, University of Twente

selective membrane. For each conductivity measurement electrode pair, the number of electrode fingers N is 11. The width of the electrode fingers $w = 10$ μm and the length of the electrode fingers $L = 400$ μm. The spacing between the interdigitated finger electrodes $s = 5$ μm. (Fig. 6.2a) As the optimal ratio $s/w \sim 0.5$ is reported elsewhere [22] for interdigitated electrodes as a rule of thumb.

Impedance measurements were performed by an in-house built impedance analyzer in constant voltage mode. (TCO) A function generator (Agilent/HP 33120A) providing a sinusoidal input signal of varying amplitude is connected by a shielded cable to the impedance magnitude and phase detector. The frequency of the applied sinusoidal signal f was varied in the range of 1 kHz to 10 MHz. An AC excitation voltage of 200 mV was applied and the current through the electrolyte resistance was measured. The impedance measurements were not performed by DC bias to prevent faradaic reaction effects. The current signal from the electrolyte was converted to voltage and amplified 10× in a trans-impedance amplifier. The amplifiers were built on the PCB attached on the chip holder cap to minimize noise and parasitic capacitance. As there are three pairs of conductivity measurement electrodes on each microfluidic device, three separate amplifiers were built on the PCB with identical electronic settings. The electronic calibration of the impedance analyzer was performed with open/short circuit voltages as well by known resistances. The detailed block diagrams schematically representing the electronic circuit designs of the impedance analyzer are provided in Appendix A.

The calibration of the impedance analyzer for each conductivity electrode pair was performed for various ionic strength NaCl solutions to obtain a correlation between the measured resistances Z and the known conductivity σ of the solutions. The measured resistances Z were further correlated to NaCl concentrations C. Figure 6.2b-c show the obtained Bode plots for a conductivity measurement electrode pair on a side-channel design microfluidic device for various ionic strength NaCl solutions. The impedance Z is frequency f dependent on planar finger type conductivity electrodes. [22, 23] The electrical characteristics of such conductivity cells are typically described by simplified equivalent electrical circuit models including the resistance of the electrolyte solution R_{el}, the capacitances formed by the electrical double layers C_{DL} and the cell capacitance

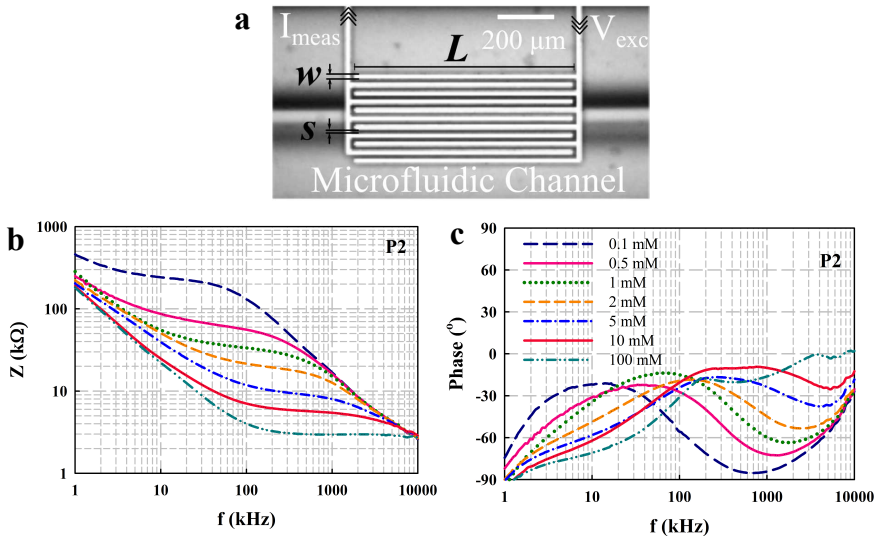

Figure 6.2: Impedance Measurements. (a) Optical microscopy image of a conductivity measurement electrode pair. Here, $w = 10$ μm, $s = 5$ μm and $L = 400$ μm. The applied excitation voltage V_{exc} and the measured current response I_{meas} are depicted by arrows. (b) Impedance magnitude measurements as a function of frequency for various ionic strength NaCl solutions. (c) Impedance phase measurements as a function of frequency for various ionic strength NaCl solutions, of the same measurements shown in (b).

C_{cell}. [22, 23] Figure 6.2b reveals three distinct regions on the measured impedance profiles as a function of frequency. The nonlinear region obtained at low frequency values is determined by double layer capacitances C_{DL}. The second linear plateau region represents the resistance of the electrolyte solution obtained at optimal frequency ranges for conductivity measurements where the measured phase values approach 0^o, confirming the resistive behavior in this region. (Fig. 6.2c) The third region obtained at high frequency values is mainly determined by cell capacitance C_{cell}. [22]

The measurements as shown in Figures 6.2b-c were performed for each conductivity detection electrode pair to obtain calibration curves correlating salt concentration to measured impedance values. The experimental

cell constants were obtained. The cell constant K_{cell} is a parameter of interest relating the electrical conductivity of the solution G (S/cm) and the measured conductance σ (S), *i.e.* measured impedance Z (Ω)

$$G = \mathrm{K}_{cell} \cdot \sigma \tag{6.4}$$

The cell constant K_{cell} is determined by the geometry of the conductivity measurement electrodes and can be calculated. The details of cell constant K_{cell} calculations and comparisons with the experimentally obtained values are provided in Appendix A.

In-situ Ion Transport Measurements

Passive and active ion transport across the fabricated membranes was studied under no DC bias and applied DC potential across the membrane, respectively.

Diffusion experiments were conducted by filling one of the main fluidic microchannels by a concentrated aqueous NaCl solution (C_o^c = 10 mM) and a dilute aqueous NaCl solution (C_o^d = 0.1 mM). The local ion concentrations were obtained by conductivity measurements as a function of time.

DC voltage was delivered from the dedicated disk shape micro-electrodes (Fig. 6.10-6.11) and the current response was measured by a multimeter. (Keithley 2000)

For visualizing the dynamic change of local salt concentration gradients upon varying external DC potential, the change in fluorescent intensity of the anionic fluorophore Bodipy 564 (Invitrogen) was recorded at 1-8 frames per second with a CCD camera (LaVision) on an inverted microscope (Carl-Zeiss). For these experiments, the electrolyte solution was 1 mM NaCl solution seeded with 0.01 mM Bopidy.

Local Flow Fields Visualization

The flow of negatively charged 1 μm fluorescent particles seeded in 1.0 mM NaCl aqueous solutions was tracked under externally applied DC bias. The particle loading was 0.05 w/v%. A dual-cavity laser with a wavelength of 527 nm was used for excitation of the fluorescent particles. (LaVision) Images were recorded at 1-8 frames per second with a CCD camera (LaVision) on an inverted microscope (Carl-Zeiss) with a resolution of 1376 × 1040 pixels × 12 bit. To enhance particle visibility and the signal-to-noise ratio, image pre-processing was performed. Averaged mean intensity images were calculated and subtracted from the images.

6.3 Results and Discussion

6.3.1 Membrane Formulation and Characterization

In the presented study, the chemical compositions of the membrane materials are formulated to obtain ion selective membranes with controllable charge properties in microchannels by photo-induced fabrication methods. Photo-polymerization by selective UV irradiation of charged monomers is highly promising for integrating versatile tailor-made ion exchange membranes with precisely defined interface geometries in microfluidic devices. For electrodialysis, the charge stability of the photo-polymerized ion exchange membrane in a wide pH range is of paramount importance. In this study, diallyldimethylammonium chloride (DADMAC) has been chosen as the base charged monomer among various candidates due to pH independent charge stability, photo-sensitivity, and solubility in water. [6, 8, 16, 17, 20] These properties suggest that DADMAC is a suitable charged monomer to obtain ion selective interfaces in microfluidics.

Figure 6.3 shows the free radical initiated photo-polymerization reaction scheme of DADMAC monomer. The photo-fragmentation of the photo-initiator Irgacure 2959 yields free radicals. [24] (Fig. 6.4a) The released radicals attack the DADMAC monomers and the linear chain polymerization is initiated. (Fig. 6.4b)

Linear poly(DADMAC) chains formed by photo-polymerization reacts further with the crosslinker agent NbisA under UV light. (Fig. 6.4)

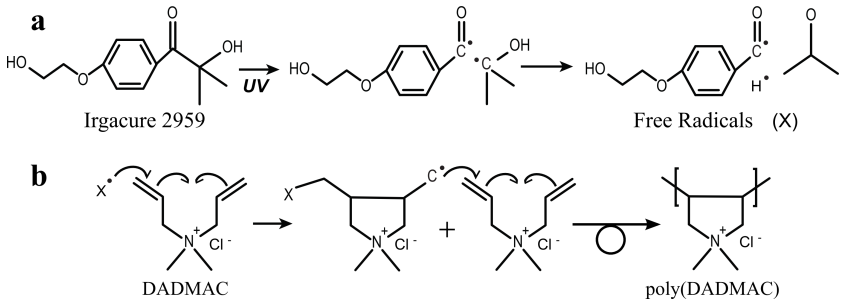

Figure 6.3: Photo-polymerization of DADMAC. (a) Photo-fragmentation of the photo-initiator and the released radicals (b) The initiation and propagation of photo-polymerization of DADMAC.

The linear polymer chains are connected by NbisA. Figure 6.4 shows a schematic of the resultant crosslinked polymer network when the NbisA is 3.2 mol % of the DADMAC monomers. Here, the positive charge of the DADMAC monomer results in a high charge density of 7.77 M, as shown in Figure 6.4 by the red color representing positive charges.

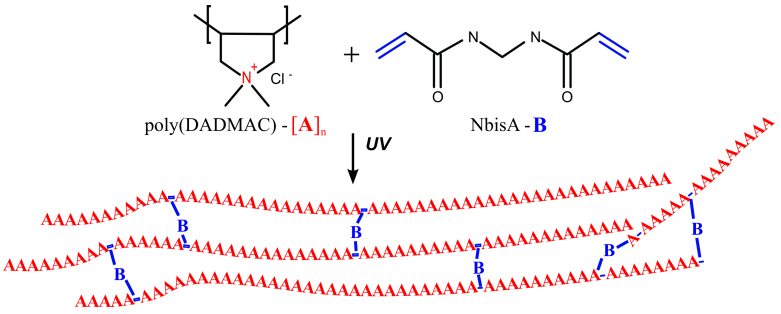

Figure 6.4: Photo-crosslinking of poly(DADMAC). The schematic represents the crosslinked polymer network with a charge density of 7.77 M, when the loading of NbisA is 3.2 mol % of the DADMAC monomers. Here the red A's depict the charged monomers. The blue B's and lines depict the crosslinker and the crosslinking bonds.

Previous experimental studies have suggested DADMAC hydrogels as super-adsorbents with a favorable swelling behavior due to their high charge density. [25] To fabricate charged DADMAC based ion exchange

membranes with controllable interfaces in highly confined microchannels, the swelling behavior of the developed membranes need to be tailored. The equilibrium swelling theory states that the primary variables determining the swelling are the ion content of the polymer matrix, the crosslinking density and the solvent interaction parameter. [26] As water is the solvent used in the membrane fabrication and the electrolytes, the solvent interaction parameters are constant for the presented membranes. Whereas, the ionic content and the crosslinker density of the polymer matrix are varied.

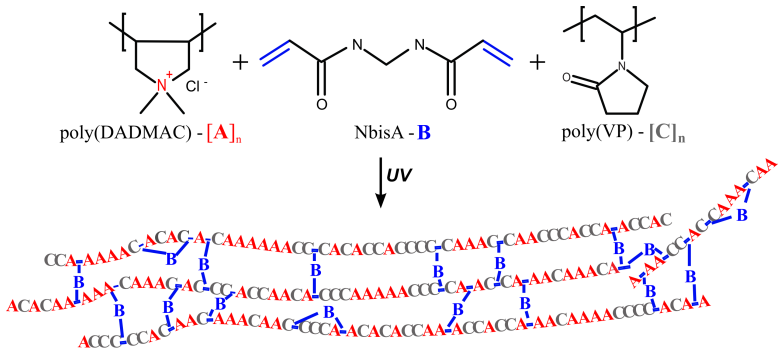

Figure 6.5: Photo-crosslinking of poly(DADMAC) and p(VP) The schematic represents the crosslinked polymer network prepared from the membrane solution with the composition DADMAC/NVP(1/1) NbisA 10 %. Here the red A's and grey C's depict the charged and uncharged monomers. The blue B's and lines depict the crosslinker and the crosslinking bonds.

The charge density of the polymer network is decreased by blending the charged DADMAC monomer with uncharged monomers. NVP was chosen as the uncharged monomer to be incorporated in the network. As the initial tests revealed that the most efficient uncharged monomer in decreasing the swelling was NVP compared to polyethylene glycol (PEG) and 2-hydroxyethyl methacrylate (HEMA).

Similar to DADMAC, the uncharged NVP monomer linearly polymerizes by free radical polymerization under UV light (Fig. 6.4) and further crosslinks via NbisA. Figure 6.5 shows a representative illustration for the photo-crosslinking of the copolymers prepared from the monomer solutions with equal molar ratios. The high charge density of DADMAC is now diluted with NVP. Furthermore, increase in crosslinking density

has been reported to increase the rigidity of the polymer reducing the swelling degree. [27, 28] The crosslinking density of the polymer network of the blend membranes presented in Figure 6.5 is higher compared to that of pure DADMAC membranes (Fig. 6.4) due to an increased crosslinker NbisA loading from 3.2 to 10 mol %.

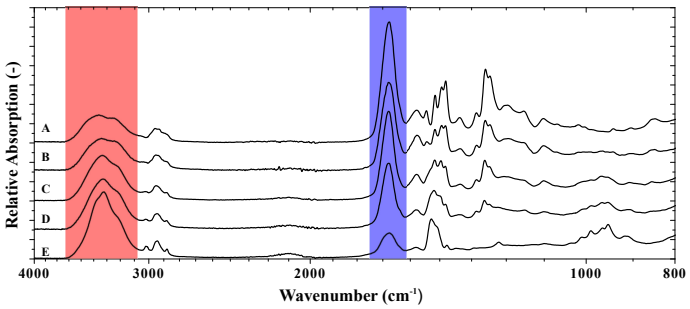

Figure 6.6: ATR-FTIR spectra of binary component membranes with different compositions. The molar ratio of DADMAc to NVP has varied. The compositions of the samples are (A) DADMAC/NVP(1/0), (B) DADMAC/NVP(3/1), (C) DADMAC/NVP(1/1), (D) DADMAC/NVP(1/3) and (E) DADMAC/NVP(0/1), where the NbisA loading = 3.2 mol %.

ATR-FTIR was performed on pure DADMAC and DADMAC/NVP copolymer based membranes to validate the photo-polymerization and photo-crosslinking reactions. Figure 6.6 show the ATR-FTIR spectra of membranes prepared from membrane solutions with varying DADMAC to NVP molar ratio at a crosslinker loading of 3.2 mol %. The increasing peak magnitude at ~ 3358 cm^{-1} for decreasing DADMAC/NVP ratios is indicative of NVP and reveal the relative decrease in DADMAC content due to the dilution with increasing amount of NVP. Similarly the increase in NVP can be seen in the decreasing peak magnitude at ~ 1640 cm^{-1} which is indicative of DADMAC.

The effect of increasing NbisA loading on the FTIR spectra is shown in Figure 6.7. The highlighted peak location is indicative of NbisA and its magnitude slightly increases as the amount of NbisA increases from 3.2% to 13%.

The ATR-FTIR spectra shown in Figures 6.6 and 6.7 verify the existence of all three components in the membrane network. Besides, the

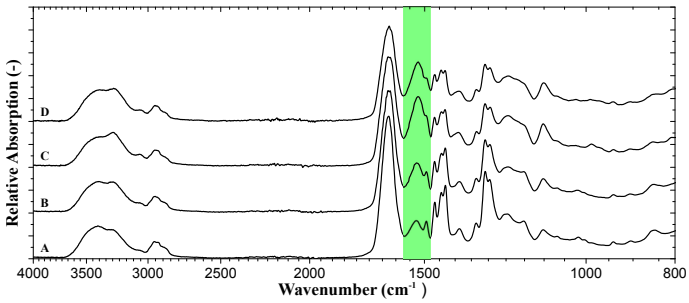

Figure 6.7: ATR-FTIR spectra for different crosslinking densities. The crosslinker NbisA loading has varied as (A) 3.2 mol %, (B) 5 mol %, (C) 10 mol %, (D) 13 mol % in a pure NVP based membrane.

variation in the composition of the compounds in the membrane casting solution reflects proportional to the variation in the resultant membranes.

6.3.2 Swelling Behavior of Batch Membranes

One of the most important characteristic of hydrogels is their ability to swell to large extents when put in contact with a thermodynamically compatible solvent. [25] For microfluidic applications as in this study, controlling the geometry of the hydrogels in the microchannels is crucial and thereby it is imperative to study and characterize the swelling behavior to control the volume changes of hydrogels. The swelling of ionic gels have been described in various theories such as rubber-elasticity theory, equilibrium swelling theory and Flory-Huggins mixing theory [26, 29] and in many experimental studies [25, 30].

Important parameters determining the structure and properties of swollen ionic hydrogels are described by a Flory swelling model based on thermodynamics of polymer solutions. When the equilibrium between the hydrogel and the solvent is established, the chemical potentials inside and outside of the polymer network are equal. The osmotic pressure of the hydrogel π_{sw} is the sum of three contributions [26]

$$\pi_{sw} = \pi_{mix} + \pi_{elas} + \pi_{ion} = 0 \tag{6.5}$$

where π_{mix} is due to the polymer-solvent interaction, π_{elas} is the elastic contribution and π_{ion} is due to the osmotic pressure of the ions in the gel phase. These contributions are given as [25, 26]

$$\pi_{\text{mix}} = -\frac{RT}{V_1}\left[\ln(1-\phi_2) + \phi_2 + \chi\phi_2^2\right] \tag{6.6}$$

$$\pi_{\text{elas}} = -C_c N RT\left[\left(\frac{\phi_2}{\phi_{20}}\right)^{1/3} - \frac{1}{2}\left(\frac{\phi_2}{\phi_{20}}\right)\right] \tag{6.7}$$

$$\pi_{\text{ion}} = RT\sum\left(C_{\text{gel}}\gamma_{\text{gel}} - C_w\gamma_w\right) \tag{6.8}$$

where R is gas constant, T is temperature, V_1 is molar volume of the solvent, ϕ_2 is volume fraction of the crosslinked polymer in swollen state, χ is the Flory parameter, C_c is crosslinker concentration, N is crosslinker efficiency, ϕ_{20} is volume fraction of dry gel, C_{gel} is the concentration of ions in the polymer network, C_w is the concentration of ions in the water, and γ_{gel} and γ_w are the activity coefficients of the corresponding ions.

It is important to note here that π_{mix} is a measure for the tendency of the polymer to dissolve in the solvent. (Eqn. 6.6) π_{mix} is typically negligible for highly charged polymers like the DADMAC based membranes in this study. (Fig. 6.4) π_{elas} is related to the strength of the elastic restoring forces which is dependent on the interconnectivity of the polymer network and thereby the crosslinking density. (Eqn. 6.7) π_{ion} is the contribution of the osmotic pressure due to the differences in ion concentration between the hydrogel and the solvent. (Eqn. 6.7) Therefore, the equilibrium swelling theory reveal that the key parameters controlling the volume transition in DADMAC based hydrogels are the ion content of the polymer matrix, the crosslinking density and the ionic strength of the electrolyte solutions. The effects of these parameters on the swelling of the batch DADMAC membranes are experimentally studied by varying the crosslinker NbisA loading and the charge density of the polymer network. (Fig. 6.8)

Figure 6.8a show the swelling degree of the binary component DADMAC/NVP membranes as a function of the crosslinker NbisA loading in the range of 3.2 to 13 mol % for different blend ratios. In agreement with Flory swelling theory (Eqn. 6.7), increasing crosslinker concentration

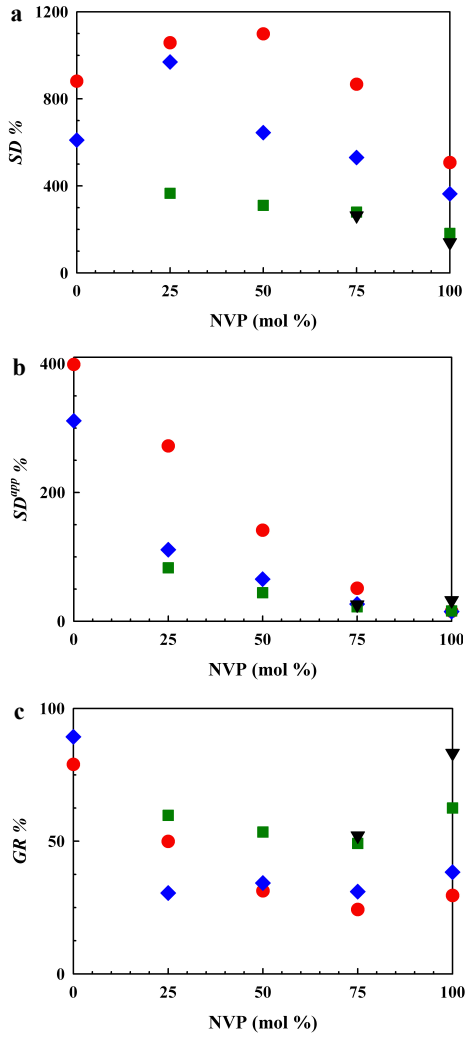

Figure 6.8: Effects of the membrane composition on swelling for varying crosslinker and uncharged monomer contents. (a) The swelling degree (b) The apparent swelling degree (c) The gel ratio as a function of NVP composition in the membrane solution for varying crosslinker NbisA loading. In (a-c) the filled circles (●), filled diamonds (◆), filled squares (■), and filled triangles (▼) represents the experimental data for NbisA loadings 3.2, 5, 10, and 13 mol %, respectively. At low NVP loadings, the crosslinker NbisA concentration was limited by solubility. Here, the equilibrating solvent is deionized water.

results in reduced swelling degrees due to increased crosslinker densities. The obtained results imply that the elastic forces (π_{elas}) are reduced by increasing the crosslinker concentration, consistent with the experimental findings of a recent study. [25]

The decrease in swelling degree with increasing amounts of NVP in the membrane solution above a certain threshold value is revealed in Figure 6.8a. A major driving force for swelling π_{ion} is reduced by blending of the charged DADMAC with the uncharged NVP. At higher NVP ratios the π_{mix} becomes dominant over π_{ion}, giving the swelling degree a threshold value for a zero charge density. Whereas at lower ratios of NVP, the swelling degree slightly increases initially compared to pure DADMAC membranes when NbisA loading is 3.2 and 5 mol %. (Fig. 6.8a) This deviation from equilibrium swelling theory for low NVP loadings is related to a decreased crosslinker efficiency N. Figure 6.8c shows the gel ratio GR, which is a typical measure for the yield of photo-induced reactions, for varying blend ratios and crosslinker loadings. Increasing NVP ratios result in decreasing gel ratio profiles, implying shorter polymer chain lengths and as well lower crosslinking density, in particular when the crosslinker loading is low. (NbisA 3.2 and 5 mol %)

The swelling degree (SD) as shown in Figure 6.8a represents the volume change of the swollen hydrogel compared to the dry volume of the gel. Whereas for ion exchange purposes, the absorbed water within the hydrogel network is crucial for ion transport. Both the batch membranes and the microfluidic membranes are always in wet phase during the preparation and later during the charge transport experiments. An apparent swelling degree $\text{SD}^{\text{app}}(\%) = (m_{\text{s}} - m_{\text{UV}})/m_{\text{UV}} \cdot 100\%$ is defined , representing the volume change of the swollen hydrogel compared to the volume of initially wet hydrogel after the UV illumination and before the equilibration in the solvent. (Eqn. 6.2) SD^{app} is a practical key parameter compared to SD and GR, in particular for microfluidic applications giving the additional volume expansion in the microchannels. Figure 6.8b shows the SD^{app} measurements for varying blending ratios and crosslinker loadings. A considerable decrease in apparent swelling degree is obtained by increasing the uncharged monomer NVP and the crosslinker NbisA content in the membrane formulation. SD^{app} is decreased to ~ 20 % for DADMAC/NVP (1/3) NbisA (13%) membranes from ~ 400 % for pure

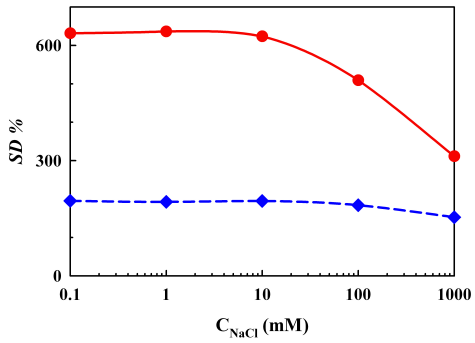

Figure 6.9: The effect of ionic strength of the electrolyte solutions on the swelling. The filled circles (●) and the filled diamonds (◆) represents the experimental data for pure DADMAC NbisA (5%) membranes and DADMAC/NVP (1/3) NbisA (13%) membranes, respectively. The equilibrating solutions are aqueous NaCl solutions.

DADMAC NbisA (3.2%) membranes. The experimental results reveal that the composition of DADMAC/NVP(1/3) NbisA 13% membrane solutions yields membranes with the lowest (apparent)swelling degree and a relative high gel ratio. Based on these experimental findings, this composition is selected for microfluidic fabrication of ion selective membranes.

Figure 6.9 shows the swelling behavior of DADMAC/NVP(1/3) NbisA 13% membranes equilibrated with various ionic strength salt solutions compared to pure DADMAC NbisA (5%) membranes. The SD of both materials is constant until the concentration of the salt solution is 10 mM after which it starts to decrease. The decrease in SD is related to a decrease in osmotic pressure difference between the membrane network and the surrounding salt solution π_{ion}, consistent with the equilibrium swelling theory. (Eqn. 6.8) The decrease in swelling degree for an increase in salt solution concentration from 0.1 mM to 1M is ~ 28 % for DADMAC/NVP(1/3) NbisA 13% membranes whereas ~ 104 % for pure DADMAC NbisA (5%) membranes. The results shown in Figure 6.9 further validates the applicability of the developed binary component membranes in microfluidics with a wide range of ionic strength solutions as operating electrolytes.

6.3.3 Microfluidic Ion Exchange Membranes

Microfluidic Devices

The layout of a representative microfluidic device is shown in Figure 6.10. The electrodes, fluidic connections and dedicated membrane region is depicted on the aligned cleanroom fabrication mask drawings for silicon and glass wafers. (Fig. 6.10a) A representative SEM image of the silicon microchannels fabricated with this design is shown in Figure 6.10b.

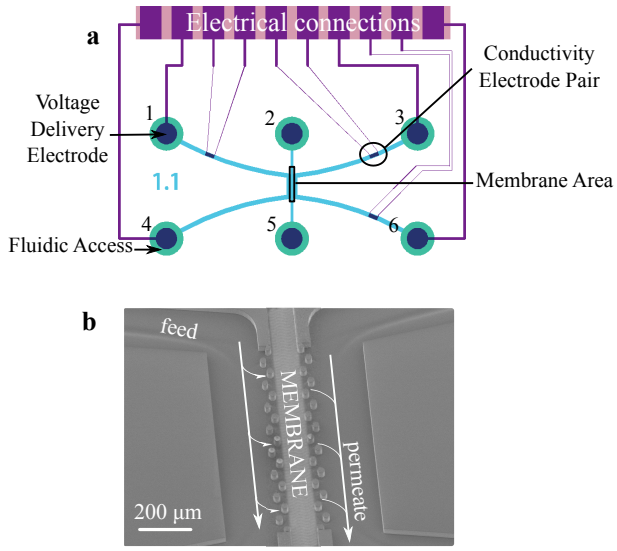

Figure 6.10: The layout of the microfluidic chips. (a) A voltage delivery disk shape electrode, conductivity electrode pair, and a fluidic access via-hole are indicated by arrows. Here, the microchannel in the middle is dedicated for membrane fabrication. (b) A representative SEM image of a microfluidic device with the design shown in (a). The dedicated membrane area in the middle channel is highlighted. The flowing feed and permeate electrolyte solutions are indicated by arrows.

Figure 6.11 show three different designs allowing for three kinds of membrane geometries. The first design is a 3-channel design, where an ion selective membrane can be fabricated in the middle channel in between two main fluidic microchannels. (Fig. 6.10b) The second design is an x-shape design, where the two main channels are connected by an opening,

where a free standing membrane can be fabricated. The final design is a side-channel design, where side-channels were fabricated in between the two main microchannels. The ion selective membranes are fabricated in these side-channels where the silicon posts suggest mechanical support to the membranes.

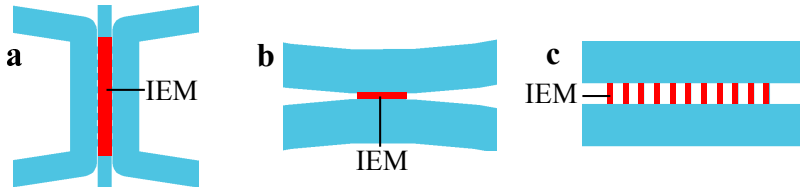

Figure 6.11: Different types of microfluidic devices fabricated, suggesting different membrane geometries (a) Three channel design, where the middle microchannel dedicated for membrane is confined by microstructures, here microposts. (b) x-shape design, where the main fluidic microchannels are connected by a gap dedicated for membrane. (c) Side-channels design, where the main fluidic microchannels are connected by side channels dedicated for membranes. In (a-c) the ion exchange membrane IEM area is highlighted by red color.

In-situ Fabrication of IEMs

The developed membrane compositions with tunable swelling properties are used as the base membrane solutions for the membrane fabrication in the microfluidic devices by selective photo-poylmerization and crosslinking. The stationary membrane solution filled in the microchannels are locally illuminated with UV light by the aid of a photo-mask (Figs. 6.10-6.1). Once the photo-induced reactions are complete, the microchannels are flowed with deionized water.

Figures 6.12a-d show optical microscopy images captured at each step of the in-situ fabrication of pure DADMAC NbisA 3.2% membranes in a side-channel microfluidic design. The photo-mask is aligned such that the illuminated region coincides the connecting side-channels. (Fig. 6.12b) Figure 6.12a show the non-polymerized monomer solution in the main microchannels and the polymerized solution in the bridging channels which

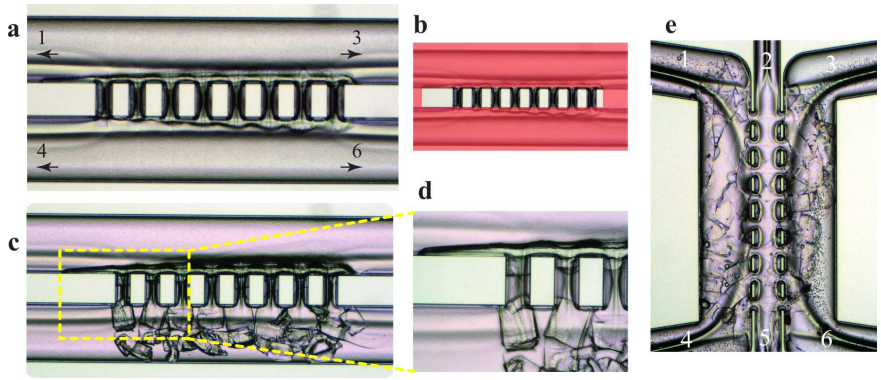

Figure 6.12: In-situ fabrication of pure DADMAC membranes. Optical microscopy images of a side-channel design micro-device (a) directly after UV illumination where the main microchannels are filled with unexposed monomer solution and the bridging channels include the polymerized hydrogel. The fluidic inlet and outlets are indicated with arrows as (1,4) and (3,6), respectively. (b) The photo-masked device allowing only for the open area to be UV exposed. (c) The swelling of hydrogel during cleaning step. (d) A zoom-in image of (c) showing the ruptured hydrogel form the side channels. (e) Optical microscopy image of a swollen pure DADMAC hydrogel in a three channel design. In (a-e) NbisA is 3.2 %.

is slightly over-polymerized towards the main channels. Once the deionized water is pumped through the microchannels to remove the residual monomer solution, the pure DADMAC membrane fabricated in the side-channels swell. (Fig. 6.12b) As can be seen in Fig. 6.12b obtained at a higher magnification, the swollen hydrogel is ruptured from the highly confined side-channels due to the stresses associated with the large extent of swelling.

Figure 6.12d shows an optical image taken after the water cleaning step in a three-channel microfluidic design where the hydrogel is initially prepared in the middle channel. In this design, the membrane is confined with micro-posts and the constraining stresses are less compared to the side-channel design. The hyrogel experiences various wrinkling and buckling conformations upon swelling, blocking the whole microfluidic device. These findings verify that controlling the volume conformations of hydrogels fabricated in microchannels is highly crucial.

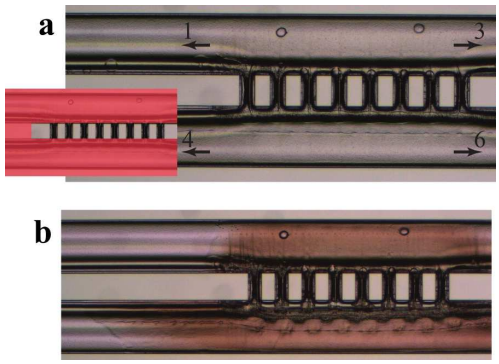

Figure 6.13: Selective UV exposure of stationary DADMAC/NVP(1/3) NbisA 13% solutions. Optical micrpscopy images a side-channel design (a) directly after UV illumination when the photo-mask, shown in the inset, is removed. (b) during water cleaning. Here the extended brown area is over-polymerized, blocking the microchannels.

The tailored membranes with a solution composition of DADMAC/NVP (1/3) NbisA 13% are prepared with the same methodology. Figure 6.13a shows an optical image captured directly after the UV illumination. The main fluidic channels are filled with unexposed monomer solution and the side channels are filled with selectively exposed polymerized solution, as shown in the inset. Here the interface between these two phases is not sharp compared to that in Figure 6.12a, implying a severe over-polymerization towards the mainchannels. Indeed the brown area shown in Figure 6.12b extending towards the upper boundary of the top channel and the lower boundary of bottom channel is a polymerized region blocking the fluidic channels. Such an over-polymerization can occur due to several reasons. First the higher reactivity of DADMAC/NVP(1/3) NbisA 13% solution compared to pure DADMAC NbisA 3.2%. The lower gel ratio of the binary component membrane actually implied a lower reactivity compared to pure DADMAC. Another reason can be the diffusion of free-radicals produced in the UV exposed region during the illumination time. The free-radicals with diffusion coefficients $\sim 5{\times}10^{-10}$ m^2/s in water [31] can diffuse several hundred micrometers through the stationary unexposed monomer solution in the main microchannels.

In order to minimize the diffusion effect of the free-radicals, a mild

convective flow was applied during the in-situ fabrication. Figure 6.14a revels the membrane produced from DADMAC/NVP(1/3) NbisA 13% solution in a three-channel design device by (i) photo-masking (the inset of Fig. 6.14a), (ii) filling the channels from inlets 1, 2 and 3 with a flow rate of 20 μl/min, (iii) decreasing the flow rate in the main microchannels 1-4 and 3-6, and stopping the flow in the microchannel dedicated for membrane (2-5), (iv) selective UV exposure, (v) cleaning with deionized water. Figure 6.14b reveals the membrane after contacting with deionized water, precisely constrained in the dedicated membrane area having fluidic interfaces between the micro-posts. The tailored DADMAC/NVP(1/3) NbisA 13% membranes have an apparent swelling degree of ~ 20 % which allows for the fabrication of ion exchange membranes with controllable interfaces.

The same membrane solution and membrane preparation parameters are applied on the side-channel and the x-shape design microfluidic devices. Figure 6.14c-d show the obtained membranes on the these fluidic configurations. The x-shape design allows for an unsupported membrane with low confinement stresses. (Fig. 6.14c) The shift of the membrane from the connecting gap towards the upper channel was caused by a slight misalignment of the photo-mask. For the side-channel design (Fig. 6.14d), the slight volume expansion of the hydrogel in the bridging channels may still cause the detachment from the side channels even though not as severe as for pure DADMAC membranes. (Fig. 6.12) The side-channel design suggests the largest confinement stresses on the prepared hydrogels among the other two configurations.

In-Situ Ion Transport Measurements

The ion transport across the resultant positively charged membranes fabricated in the microchannels was investigated on the micro-devices. Passive and active ion transport was studied without and with applied DC potential across the membrane, respectively.

The passive charge transport via diffusion of the ions in the absence of external applied potential was quantified by in-situ local conductivity measurements. Diffusion experiments were conducted by filling one of the main fluidic microchannels by a concentrated aqueous NaCl solution (C_o^c = 10 mM) and a dilute aqueous NaCl solution. (C_o^d = 0.1 mM) The

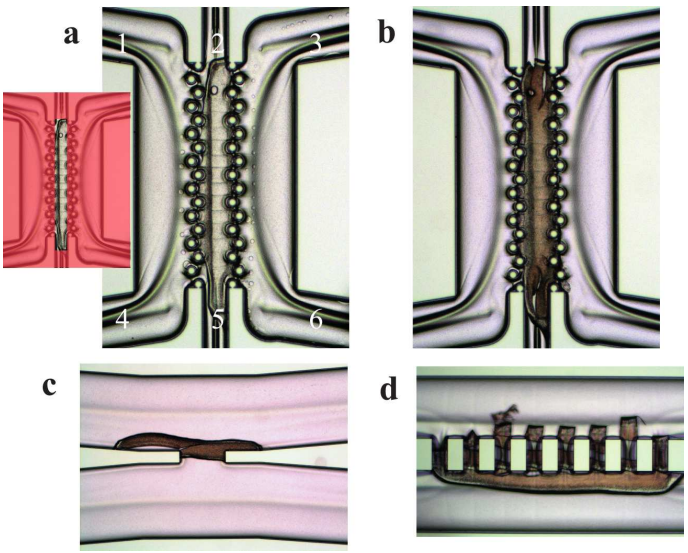

Figure 6.14: Membranes with controllable swelling properties prepared by the developed fabrication method. (a) Optical microscopy image of a polymerized solution in the middle channel (2-5) in a three-channel design. Here the microchannels (1-4) and (3-6) are filled with monomer solution. (b) The hydrogel membrane obtained after the deionized water cleaning of the microchannels shown in (a). (c) The hydrogel membrane obtained in an x-shape device. (d) The hydrogel membrane obtained in a side-channel design. In (a-d) the employed membrane solution is DADMAC/NVP(1/3) NbisA 13%.

change in conductivity of the dilute and the concentrated side microchannels was measured in time intervals of ~ 3 hours in a total time period of 24 hours. During the measurements the salt solutions were stationary.

Figure 6.15 shows the experimental results of a diffusion experiment as a function of time in comparison to the numerical results obtained by the solution of Fickian diffusion of salt molecules in the aqueous phase and in the membrane. 2D simulation was performed on the same microfluidic geometry with identical dimensions. The diffusion equation was solved for the concentrations in the dilute and concentrated side microchannels. The ion transport in the membrane was also described by diffusion with an apparent diffusion coefficient $D_{\mathrm{mem}}^{\mathrm{app}}$ which was parametrized during the

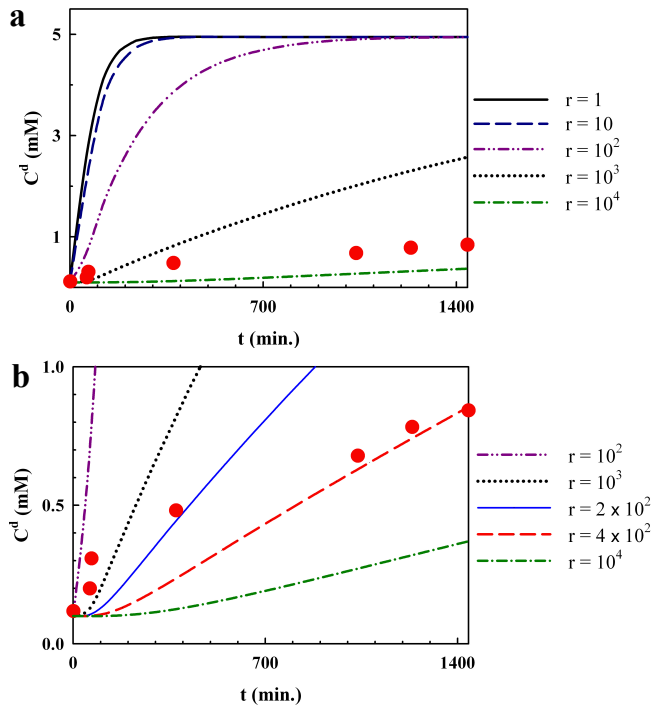

Figure 6.15: Experimental and numerical local salt concentration profiles as a function of diffusion time. (a) Increasing salt concentration profiles in the dilute side microchannel with an initial $C_o^d = 0.1$ mM obtained by conductivity measurements and numerics when $C_o^c = 10$ mM. Here the circles (•) show the experimental results and the solid lines show the numerical results obtained for varying fitting parameters r. (b) The zoom-in of (a) with additional r values.

simulation. $D_{\text{mem}}^{\text{app}}$ was varied as a function of the diffusion coefficient of NaCl in water D_{aq}, where $D_{\text{mem}}^{\text{app}} = D_{\text{aq}}/r$. Therefore when $r = 1$, the ion transport in membrane is equivalent to that of aqueous solution and the equilibrium concentration of 5mM NaCl is established in ~ 3 hours. (Fig. 6.15a) When r $\gg 1$, the time required for equilibration is much longer due to the high resistance in ion transport in the membrane. (Fig. 6.15a)

The experimental results revealed in Figure 6.15 show that the initial concentration in the dilute side microchannel ($C_o^d = 0.1$ mM) increases

slowly by time via the diffusion of salt molecules from the concentrated side. Consistent with the increase in the dilute side, the concentration measured in the concentrated side microchannel slowly decreases by only ~ 0.7 mM in 24 hours. (Fig. 6.15) The dense ion exchange membranes are reported have 30 to 200 times lower diffusion coefficients for salts compared to that of water. [32] Though the charged network of the polymer suggesting a favorable transport for the counterions, the coions are repelled due to Donnan exclusion effect. The apparent diffusion coefficient of NaCl in the membrane is predicted to be ~ $2{\times}10^3$ to $4{\times}10^3$ lower than the diffusion coefficient of NaCl in water. (Fig. 6.15b) $D_{\text{mem}}^{\text{app}}$ is estimated to be on the order of 10^{-13} m^2/s. In a previous experimental study [33], apparent diffusion coefficients in crosslinked PEG-diacrylate hydrogels have been reported as 1×10^{-10} m^2/s which is comparable to the diffusion coefficient in water. [34] The PEG-diacrylate hydrogels are slightly positively charged whereas they are not ion selective. The estimated $D_{\text{mem}}^{\text{app}}$ for the tailored DADMAC/NVP (1/3) NbisA 13% membranes are ~ 1000 times lower than that of PEG-diacrylate hydrogels and water, implying a different ion transport mechanism.

Figure 6.15b reveal that the transient concentration profile deviates from the numerical results obtained for diffusion type mass transfer, in particular for the early stages when $t < 6$ hours. The ion flux across charged, ion-selective interfaces is described by Nernst-Planck equation where convection, diffusion and electromigration contributes to the ion transport. [9, 10] During the diffusion experiments, convective flow was not applied implying that the dilute and concentrated NaCl solutions contacting the fabricated membranes were stationary. Therefore the convective flux contribution is negligible. Whereas the contribution of electromigration is of importance in particular for the initial time periods when the concentration difference in dilute and concentrated sides are at maximum resulting in a Donnan potential of ~ 116 mV. The deviation from the diffusion driven transport, which may be attributed to electromigration effects, is indicative of the permselectivity of the fabricated membranes. (Fig. 6.15b)

The charge transport across the prepared microfluidic membranes under an external transverse electrical field was studied by current-voltage (I-U) measurements. Figure 6.16 shows representative I-U measurements performed sequentially on a three-channel microfluidic device including a

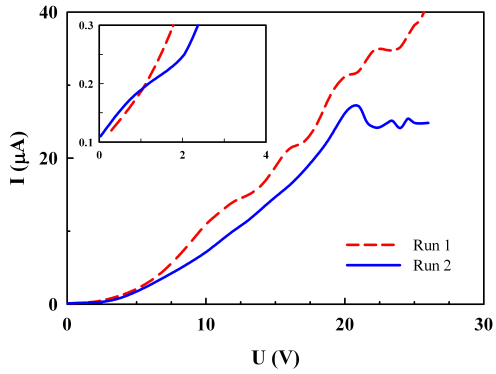

Figure 6.16: I-U measurements The current-voltage response of a three channel design microfluidic device integrated with a DADMAC/NVP(1/3) NbisA 13% membrane obtained by chronopotential measurements. Two sequential recordings are presented.

DADMAC/NVP(1/3) NbisA 13% membrane and stationary electrolyte solutions of 0.1 mM NaCl in the main micochannels. For ion exchange membranes, the diffusion limited transport is typically quantified by the limiting current density j_{lim} obtained experimentally by I-U measurements. [9, 10] At the diffusion limited region, the current reveals a plateau and does not increase with applied potential due to the depletion of ions at the membrane interface. The theoretical limiting current density can be calculated as $j_{\text{lim}} = (DFzC)/\delta$, where D is the diffusion coefficient of the counterion, F the Faraday constant, z the valence of the counterion, C the concentration of the counter ion and δ the thickness of the diffusion layer. [9, 10, 35]

The profiles of current-voltage curves revealed in Figure 6.16 obtained sequentially differ from each other. The first recording does not reveal distinct regimes whereas the second recording show the initially ohmic regime with a linearly increasing current for increasing potential differences and reaching a plateau-like regime ~ at 22 V with a constant current at ~ 24 μA. However the theoretical limiting current ($I_{\text{lim}} = j_{\text{lim}} \cdot A_{\text{mem}}$) is calculated to be 14.4 nA when the diffusion layer thickness δ is considered as the width of the electrolyte microchannel. ($\delta = 200\mu$m) The potential coinciding the limiting current 14.4 nA estimates ~ 3.5 V when only the electrical

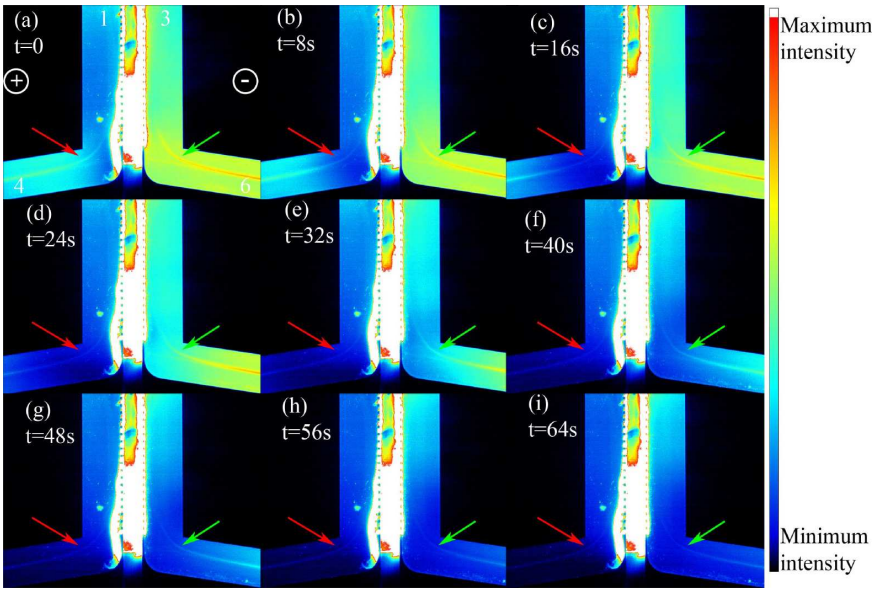

Figure 6.17: Visualization of local charge transport. In (a-i) a time series of optical microscopy images are presented showing the time evolution of the depleting intensity of negatively charged Bodipy.

resistance of electrolyte solution is considered. The inset in Figure 6.16 show a plateau-like regime at ~ 2 V with a current value ~ 200 nA which is higher than the estimated limiting current value. The obtained high currents and the bumpy I-U profiles could be related to galvanic reactions. Considering the electrochemical potential of water splitting 1.2 V [34], the applied high DC voltages can result in galvanic reactions at the direct contact electrodes which creates additional ions and thereby increase the measured currents. Such electrochemical reactions can potentially alter the pH of the system. [36]

The dynamics of charge transport near the DADMAC/NVP membranes is visualized by a negatively charged fluorescent marker Bodipy dissolved in the NaCl electrolyte solution. Bodipy is a pH insensitive fluorophore in comparison to other widely used fluorescent probes. [37]

Figure 6.17 shows an optical microscopy image series of the fluorescent probe Bodipy under a potential difference of 15 V, without any applied

flow. At t=0, there is a considerable fluorescent intensity in both of the microchannels, representing the Bodipy concentration in the channels. It is important to note that Bodipy concentration gradients are established with the onset of the applied voltage at t=0. (Fig. 6.17a) The fluorescent intensities in the microchannels obtained at t=0 in comparison to the low intensities obtained after 64 s reveal the depleting concentration of the negatively charged Bodipy in the microchannels over time. In Figures 6.17a-i, the microchannel on the left of the membrane is on the anodic side and the right channel is on the cathodic side.

On the anodic side depicted by a red arrow, the depleted zone extends towards the bottom left corner of the anodic microchannel at t=8 s. The anodic side microchannel is nearly depleted after 24 s. It is important to note here that the depletion of negatively charged Bodipy propagates towards the outlet of the channel (the anode electrode). The intensity of the area depicted by the green arrow on cathodic side drops much slower compared to the anode microchannel. Even after 64 s, cathode side microchannel is not completely depleted from Bodipy. (Fig. 6.17i) In cathode side channel, the Bodipy depletion initiates from the bottom corner of the membrane and propagates towards the inlet (depicted as 3) adjacent to the membrane area.

In Figures 6.17a-i, the Bodipy concentration gradients within the membrane can not be observed due to the over exposure of this area. Though the depletion layers could clearly be seen, enrichment of Bodipy is not observed. The time series images indicate the migration of negatively charged fluorescent marker towards the positively charged membrane on the cathode side. However, the release of the marker at the anode interface could not be captured, which may be related to the slow transport of the bulky Bodipy molecules across the membrane network.

Local Flow Fields Visualization

The charge and momentum transport near ion selective membranes are coupled. [35, 38] Under intensive externally applied DC voltages, an overlimiting conductance (OLC) regime with severe ion concentration polarization (ICP) effects has been observed in various studies. [2, 39–41] The

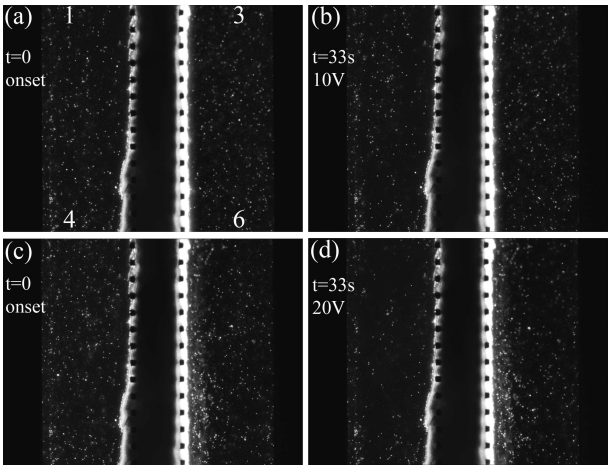

Figure 6.18: Microscope images of a three-channel design device including particle solutions under DC bias. Electrodes at 3 and 6 were ground. Electrodes at 1 and 4 are at 10 V in (a) and (b) at t=0 and t=33 s, respectively. Electrodes at 1 and 4 are at 20 V in (c) and (d) at t=0 and t=33 s, respectively.

dynamic coupled transport processes have been reported to induce additional electrokinetic flows. [2, 36, 38–41] Particle tracking has been often used for visualization of ICP induced electrokinetic flows. [3, 35, 41, 42]

In the presented microfluidic devices including an ion exchange membrane and direct contact metal electrodes, it is imperative to visualize the ICP induced coupled charge and momentum transport by tracking negatively charged particles. The experiments were performed for varying DC bias across the membrane with 1 μm particles seeded in 1mM NaCl solutions at stationary conditions with no externally applied convective flow.

Figure 6.18 show representative optical microscopy images of a three-channel design micro-device with the DADMAC/NVP (1/3) NbisA 13% membranes in the middle confined by stationary particle solutions in the main microchannels. Once a transverse electric field was applied across the membrane, the microscopy images were recorded over time. Figures 6.18a and c represent the initial distribution of particles in the microchannels at the moment a DC bias of 10 V and 20 V, respectively, is applied. After 33

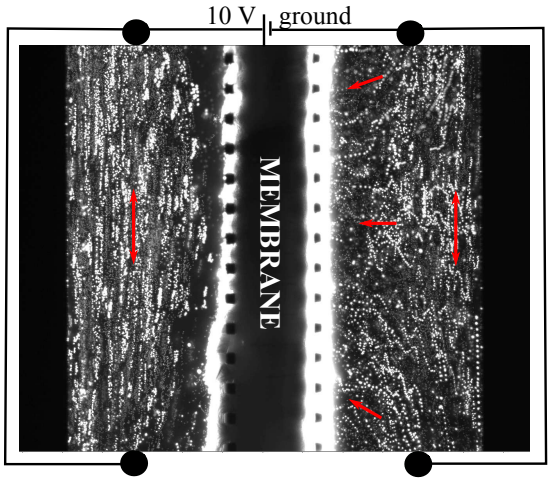

Figure 6.19: Trajectories of particles induced by ICP Time stack of 30 optical microscopy images of fluorescent particles in a three-channel design chip. The direction of the particle velocities are depicted by red arrows.

s of constant DC voltage delivery, the particles, which were initially at stationary conditions with no convective bulk flow, migrate towards the inlet (depicted as 1) and outlet (depicted as 4) of the anodic microchanel at the left hand side of the membrane depleting the microchannel. (Fig. 6.18c-d) The migrated negatively charged particles have been observed to accumulate on the anode electrodes (beyond 1 and 4). The change in particle density in the anode side microchannels was qualitatively proportional to the magnitude of applied voltage. (Fig. 6.18c-d)

The cathode side microchannels are not depleted as severely as the anodic side. In Figure 6.19, the flow induced by the electrophoretic velocity of the particles is presented by time stacking of 30 microscopy images recorded at 3.3 frames per seconds for the same experiment shown in Figure 6.18a-b. In the anodic microchannel, the particles move longitudinal towards the electrodes. (Fig. 6.19) The same longitudinal movement is also observed for the cathode side microchannel approximately in the half of the channel width. (near the silicon boundary) Whereas in the other half of the cathode side channel, the particles move transversely towards the interface of the positively charged membrane. (Fig. 6.19) These

experimental findings obtained by the particle tracking experiments are consistent with the local ion concentration visualizations obtained by fluorescent intensity measurements of Bodipy. (Fig. 6.17) The experimental results reveal the dynamic and complex behavior of coupled charge and momentum transport in microfluidic devices including ion selective interfaces such as ion exchange membranes and metal electrodes.

6.4 Conclusions

In this chapter, ion exchange membranes integrated microfluidic devices are presented. Hydrogel based ion exchange membranes are fabricated locally in the microchannels by selective photo-polymerization. The chemical composition of the membranes are tailored to obtain optimal charge and swelling properties allowing for in-situ fabrication of ion selective membranes with controlled geometries in highly confined microchannels. The swelling of the prepared hydrogel membranes are controlled by varying the charge density and the crosslinking density of the resultant polymer networks. The charge content of the tailored membranes was confirmed by ATR-FTIR.

In the resulting microfluidic devices, the passive charge transport via diffusion and active charge transport via an external DC bias were studied in detail. The obtained experimental results indicate the charge-selectivity of the presented microfluidic membranes. The local salt concentrations were experimentally obtained by conductivity measurements in the microchannels. The predicted apparent NaCl diffusion coefficient of the prepared membranes via salt diffusion experiments are in the range of 0.5 - 2 $\times 10^{-13}$ m^2/s, which is several order of magnitude lower than the diffusion coefficient of ions in water, or that of the counterion in the membrane. The visualizations of local concentration and ICP induced flow fields of negatively charged species reveal developing ion depletion layers near the in-situ prepared anion exchange membranes.

Bibliography

[1] Kim SJ, Song YA, Han J (2010) Nanofluidic concentration devices for biomolecules utilizing ion concentration polarization: theory, fabrication, and applications. *Chem. Soc. Rev.* 39(3):912-922.

[2] Zangle TA, Mani A, Santiago JG (2010) Theory and experiments of concentration polarization and ion focusing at microchannel and nanochannel interfaces. *Chem. Soc. Rev.* 39(3):1014-1035.

[3] Kwak R, Guan G, Peng WK, Han J (2012) Microscale electrodialysis: Concentration profiling and vortex visualization. *Desalination* 308:138-146.

[4] Kim SJ, Ko SH, Kang KH, Han J (2010) Direct seawater desalination by ion concentration polarization. *Nature Nanotech.* 5(4):297-301.

[5] Sommer GJ, Mai J, Singh AK, Hatch AV (2011) Microscale Isoelectric Fractionation Using Photopolymerized Membranes. *Anal. Chem.* 83(8):3120-3125.

[6] Cheng LJ, Chang HC (2011) Microscale pH regulation by splitting water. *Biomicrofluidics* 5(4):046502.

[7] Dhopeshwarkar R, Crooks RM Hlushkou D, Tallarek U (2008) Transient effects on microchannel electrokinetic filtering with an ion-permselective membrane. *Anal. Chem.* 80(4):1039-1048.

[8] Kim SK, Kim JH, Kim KP, Chung TD (2007) Continuous low-voltage dc electroporation on a microfluidic chip with polyelectrolytic salt bridges. *Anal. Chem.* 79(20):7761-7766.

[9] Mulder M (1996) *Basic principles of membrane technology.* (Second edition, Kluwer Academic Publishers).

[10] Mulder M (2004) *Membrane technology and applications* (Second edition, John Wiley & Sons Ltd.).

[11] Kwak R, Pham VS, Lim KM, Han J (2013) Shear Flow of an Electrically Charged Fluid by Ion Concentration Polarization: Scaling Laws for Electroconvective Vortices. *Phys. Rev. Lett.* 110(11):114501-114506.

[12] Park SC, Taek D, Kim HC (2009) Ion bridges in microfluidic systems. *Microfluidics nanofluidics* 6(3):315-331.

[13] Hatch AV, Herr AE, Throckmorton DJ, Brennan JS, Singh AK (2006) Integrated preconcentration SDS-PAGE of proteins in microchips using photo-patterned cross-linked polyacrylamide gels. *Anal.Chem.* 78(14):4976-4984.

[14] Song S, Singh AK, Shepodd TJ, Kirby BJ (2004) Microchip dialysis of proteins using in situ photopatterned nanoporous polymer membranes. *Anal.Chem.* 76(8):2367-2373.

[15] Song S, Singh AK, Kirby BJ (2004) Electrophoretic concentration of proteins at laser-patterned nanoporous membranes in microchips. *Anal.Chem.* 76(15):4589-4592.

[16] Chun, Chung TD, Kim HC (2005) Cytometry and Velocimetry on a Microfluidic Chip Using Polyelectrolytic Salt Bridges. *Anal. Chem.* 77(8):2490-2495.

[17] Chun H, Kim HC, Chung TD (2008) Ultrafast active mixer using polyelectrolytic ion extractor. *Lab Chip* 8(5):764-771.

[18] Sang KK, Hyojin L, Taek DC, Hee CK (2006) A miniaturized electrochemical system with a novel polyelectrolyte reference electrode

and its application to thin layer electroanalysis. *Sens. Actuat. B Chem.* 115(1):212-219.

[19] Han JH, Kim KB, Kim HC, Chung TD (2009) Ionic Circuits Based on Polyelectrolyte Diodes on a Microchip. *Angew. Chem. Int. Ed.* 48(21):3830-3833.

[20] Kim KB, Han JH, Kim HC, Chung TD (2010) Polyelectrolyte junction field effect transistor based on microfluidic chip. *App. Phys. Lett.* 96(14):143506-143506.

[21] Nge PN, Yang W, Pagaduan JV, Woolley AT (2011) Ion permeable membrane for on-chip preconcentration and separation of cancer marker proteins. *Electrophoresis* 32(10):1133-1140.

[22] Vrouwe E (2005) *Quantitative microchip capillary electrophoresis for inorganic ion analysis at the point of care*, (PhD thesis, EWI-BIOS, University of Twente).

[23] Olthuis W, Streekstra W, Bergveld P (1995) Theoretical and experimental determination of cell constants of planar interdigitated electrolyte conductivity sensors. *Sens. Actuat. B* 24-25:252-256.

[24] Andrzejewska E (2001) Photopolymerization kinetics of multifunctional monomers. *Prog. Polym. Sci.* 26:605-665.

[25] Korpe S, Erdoğan B, Bayram G, Ozgen S, Uludag Y, Bicak N (2009) Crosslinked DADMAC polymers as cationic super absorbents. *Reac. Func. Polym.* 69(9):660-665.

[26] Flory PJ (1953) *Principles of polymer chemistry*, (Cornell University Press).

[27] Young JS, Gonzales KD, Anseth KS (2000) Photopolymers in orthopedics: characterization of novel crosslinked polyanhydrides. *Biomater.* 21(11):1181-1188.

[28] Rydholm AE, Reddy SK, Anseth KS, Bowman CN (2007) Development and characterization of degradable thiol-allyl ether photopolymers. *Polym.* 48(15):4589-4600.

[29] Sperling LH (2005) *Introduction to Physical Polymer Science*, (Wiley).

[30] Jeon CH, Makhaeva EE, Khokhlov AR (1998) Swelling behavior of polyelectrolyte gels in the presence of salts. *Macromolec. Chem. Phys.* 199(12):2665-2670.

[31] Ukai A, Hirota N, Terazima M (2000) Radical diffusion measured by the transient grating in a short timescale. *Chem. Phys. Lett.* 319(3-4):427-433.

[32] Miyoshi H (1997) Diffusion coefficients of ions through ion-exchange membranes for Donnan dialysis using ions of the same valence. *Chem. Eng. Sci.* 52(7):1087-1096.

[33] Wu YH, Park HB, Kai T, Freeman BD (2010) Water uptake, transport and structure characterization in poly(ethylene glycol) diacrylate hydrogels. *J. Mem. Sci.* 347(1-2):197-208.

[34] Lide DR (2003) *CRC handbook of chemistry and physics*, (CRC Press, New York).

[35] Chang HC, Yossifon G, Demekhin EA (2012) Nanoscale Electrokinetics and Microvortices: How Microhydrodynamics Affects Nanofluidic Ion Flux. *Annu. Rev. Fluid Mech.* 44(1):401-426.

[36] Nikonenko VV *et al.* (2010) Intensive current transfer in membrane systems: Modelling, mechanisms and application in electrodialysis. *Adv. Coll. Int. Sci.* 160:101-123.

[37] Welder F, Mc Corquodale EM, Colyer CL (2002) Proteinase assay by capillary electrophoresis employing fluorescence-quenched protein-dye conjugates. *Electrophoresis* 23(11):1585-1590.

[38] Mani A, Bazant M (2011) Deionization shocks in microstructures. *Phys. Rev. E* 84:061504.

[39] Dydek EV, Zaltzman B, Rubinstein I, Deng DS, Mani A, Bazant, M (2011) Overlimiting current in a microchannel. *PRL* 107:118301.

[40] Rubinstein I, Zaltzman B (2010) Extended space charge in concentration polarization. *Adv. Coll. Int. Sci.* 159(2):117.

[41] Rubinstein SM, Manukyan G, Staicu A, Rubinstein I, Zaltzman B, Lammertink RGH, Mugele F, Wessling M (2008) Direct observation of a nonequilibrium electro-osmotic instability. *PRL* 101(23):236101.

[42] Yossifon G, Chang HC (2008) Selection of Nonequilibrium Overlimiting Currents: Universal Depletion Layer Formation Dynamics and Vortex Instability. *Phys. Rev. Lett* 101:254501.

7

Summary and Outlook

The transport phenomena at interfaces often determine the bulk transport rates in both micro- and macro- scale. Therefore, a better understanding of the fluid motion and the associated transport processes at these interfaces is essential. The integration of appreciable surfaces with precisely defined interfaces and with various physicochemical properties into micro-scale devices can be harnessed for direct investigations of transport processes. In this context, optimal and controllable interfaces at the boundaries of microchannels are established and the transport processes are studied at these tailored interfaces with a focus on (i) hydrodynamic slippage and coupled mass transfer at gas-liquid interfaces and (ii) charge and momentum transfer at ion selective interfaces.

7.1 Summary

Chapter 2 presents porous superhydrophobic micro-structured polymeric membranes integrated in a micro gas-liquid contacting device. The mass transport of dissolved gas in microchannels, driven by convection-diffusion, is studied both experimentally and numerically. The overall gas absorption measurements reveal the dramatic influence of the membrane morphology on the gassing/degassing of fluids. The experimental results obtained for flat hydrophobic membranes having interconnected gas-filled pores show

efficient supply of gases into liquids, in good agreement with the simulations performed with the assumptions of negligible gas phase and membrane mass transfer limitations. Micro-structured membranes revealed up to 28 % enhanced gas uptake in comparison to that obtained for the flat membranes. The superhydrophobicity of the presented membranes ensures the Cassie-Baxter state of the gas-liquid interfaces in between the porous micro-structures and thereby the establishment of hybrid gas-liquid and liquid-solid interfaces promoting effective hydrodynamic slippage. The resultant slippage induces the enhancement of the mass transfer of the dissolved gas at the slippery gas-liquid interfaces.

Chapter 3 presents the numerical simulations of momentum and mass transport near hybrid surfaces with alternating gas-liquid and liquid-solid interfaces, *i.e.* periodic bubble units. The so called bubble mattresses are established at the boundary of microchannels aligned perpendicular to pressure driven laminar flow. The influences of interface geometries of the shear-free microbubble surfaces on the hydrodynamic slippage and the mass transfer of dissolving solutes at the gas-liquid interfaces are examined. The protrusion angles of the microbubbles into the liquid flow θ and the shear free fractions of the bubble units φ (*i.e.* surface porosities) are varied in the numerical simulations. The effective slip lengths and mass transfer fluxes of dissolving species at the bubble surfaces are obtained for varying θ and φ.

Simulations reveal a strong dependency of the effective slippage on the protrusion angles θ of the bubbles into the flow. The numerical results show a maximum effective slip length when the protrusion angle θ of the microbubbles $\approx 10^o$. The effective slip lengths decrease with increasing protrusion angles when $\theta \gtrsim 10^\circ$. Consequently, a critical protrusion angle exists ($\theta_c = 55^o$), at which a transition from slippery state to frictional state is encountered.

The simulation results show the profound influence of interface geometry of the bubble mattresses, *i.e.* microbubble protrusion angle θ and surface porosity φ, on the interfacial mass transfer. At an optimal protrusion angle θ of the microbubbles $\approx 10^o$ when $\varphi = 0.67$, mass transfer enhancements up to 11 % are predicted with respect to a fully saturated non-slippery wall.

The proposed bubble mattress geometry mimics fictitious porous gas-liquid contacting membranes having regular pores. The experimental verification of the presented numerical results is of paramount importance for the essential aspects of hydrodynamic slippage and interface transport of mass *e.g.* gas absorption/desorption processes which are relevant to both developing and conventional applications in micro- and macro-scale.

Chapter 4 presents novel superhydrophobic microfluidic devices that allow the presence of stable and controllable microbubbles at the boundary of the microchannels. The presented microfluidic approach involves the pressurization of gas that allows for active gas-liquid menisci curvature control, impacting both static and dynamic responses of the interface. The effects of such unique active microbubbles on transverse pressure driven microflows are studied experimentally and numerically. Local flow fields are resolved by micro-particle image velocimetry technique at high resolution. The first experimental effective slip length results are obtained for a wide range of protrusion angles θ of the microbubbles into the liquid flow. ($-2^o < \theta < 43^o$) The measurements reveal a maximum effective slip length, corresponding to a 21 % drag reduction when θ is in the range of -2° to 12°. In agreement with the experimental results, the simulations reveal a maximum effective slip length, corresponding to a 23 % drag reduction at an optimal $\theta \approx 10°$. The experimental and numerical results reveal a decrease in slip length with increasing protrusion angles when $\theta \gtrsim 10°$.

The experimental results obtained for the presented superhydrophobic microbubble mattress show that the hydrodynamic friction and thereby the convective flow throughput in microchannels can potentially be optimized by controlling the interface geometry of the embedded microbubbles. As many micro-scale surface phenomena, the obtained large slip lengths and large drag reductions can be directly beneficial for certain macroscopic applications. Drag reduction is expected to scale as the ratio of the slip length to the thickness of the boundary layer. [1] The obtained results for the bubble mattresses imply the potential opportunity to reduce the operating costs and the energy requirements for the delivery of the liquids in comparison to pipes constrained by non-slippery walls.

Chapter 5 presents the absorption studies of a pure gas into a liquid in laminar flow. Superhydrophobic microfluidic devices are used, that allow the formation of stable and active controlled microbubbles at the

boundary of microchannels. The mass transfer of gas dissolving across the curved bubble surfaces into the liquid is studied for short contacting times. The dynamics of gas absorption is experimentally studied by fluorescent lifetime imaging microscopy where the microbubbles were formed of oxygen gas. The dynamics of interfacial mass transfer of dissolved oxygen are analyzed numerically considering (i) kinetic equilibrium conditions at microbubble surfaces that is conventionally described by Henry's Law and (ii) non-equilibrium conditions at bubble surfaces using Statistical Rate Theory (SRT).

The measurements show that kinetic equilibrium at the gas-liquid interfaces is not established for short contacting times of liquid with the microbubbles. Mass transfer into liquid flow past micro-bubbles can be well described by the simulations performed at non-equilibrium conditions for short exposure times ($\sim$ 180 μs), deviating from the commonly accepted Henry's Law. The convection enhanced bubble mattresses induces wall slip velocities on the order of 10^{-2} m/s. Such slip velocities result in very short contact times for water passing single bubble interfaces which can explain the non-equilibrium boundary condition.

The experimentally measured and numerically calculated convective mass fluxes of dissolved oxygen show that slight increase in Reynolds number Re results in enhanced interfacial mass transfer. Despite the fact that the increasing Reynolds numbers Re result in decreasing exposure times (*i.e.* decreasing dissolved oxygen concentrations at the interface), the enhanced hydrodynamics result in enhanced convective mass flux. Consistent with the literature findings [2, 3] and the results obtained in Chapter 3, the presented results of gas absorption across slippery microbubble surfaces demonstrate that the hydrodynamic slippage amplifies the interfacial mass transport on hybrid substrates consisting of liquid-solid and liquid-gas interfaces.

Chapter 6 presents the integration of hydrogel based anion exchange membranes with controlled amounts of ionic groups into microfluidic devices. Implementing charged membranes having high ion exchange capacity in precisely defined microchannels is highly desirable for charge based separations. This chapter describes a developed methodology allowing for the in-situ fabrication of tailored hydrogel based membranes in highly confined microchannel geometries by selective photo-induced methods.

First, the membrane chemistry is tailored to obtain optimal membrane formulation for microfluidic preparation. The membrane formulation is investigated in detail with a focus on swelling behavior of the resultant membranes. The chemical compositions of the charged poly(DADMAC) based membranes are altered based on equilibrium swelling theory [4] by (i) blending the charged DADMAC monomer with various neutral monomers, (ii) varying the loading of the charged monomer in the base membrane solution, thereby varying the charge density (iii) varying the loading of the crosslinker agent in the base membrane solution, thereby varying the photo-crosslinking density. Hydrogels with controllable swelling degree and charge density are developed.

Second, the in-situ photo-induced preparation parameters are investigated to obtain locally photo-patterned tailored membranes in microchannels by selective UV irradiation. With the developed methodology, the tailored membranes are fabricated locally in microfluidic devices that are designed and fabricated for charge based separations. The local charge and momentum transfer in the novel IEM integrated micro-devices are preliminary investigated utilizing charged fluorescent dyes and particles. The local ion transport across the in-situ prepared anion exchange membranes was studied via passive diffusion experiments and under external DC bias. The obtained experimental findings indicate the permselectivity of the in-situ prepared microfluidic membranes that is of primary importance in many charged based separations.

7.2 Outlook

7.2.1 Gas Liquid Contacting

A variety of practical applications can benefit considerably from tailored slippery surfaces for drag reduction. The results obtained in this study contribute to the advances in drag reduction to a great extent and also stimulate more experimental work.

Bubble Mattresses

Previous experimental studies have shown that the fragility of the Cassie state presents the main technological challenge for the engineered super-

hydrophobic substrates in many applications. [1, 5–7] Cassie-to-Wenzel transition (liquid impregnation into initially gas-filled microstructures) has been encountered due to several reasons including imbalanced liquid pressure, presence of surface defects, dissolution of trapped gas into liquid. Several methods such as electrolysis [8], joule heating [9] and surface vibrations [10] have been exploited to achieve reversible Wenzel-to-Cassie transition routes. The presented active control of bubble geometry via an active control of applied gas pressure suggest another practical approach to sustain a reversible Wenzel-to-Cassie route. The control of hydrodynamic drag by controlling the bubble geometries via a back pressurization approach can potentially be interesting for extreme conditions such as (under)water applications where the hydrostatic pressure can be balanced by the applied gas pressure to prevent the destabilization of the more desirable Cassie state in favor of a Wenzel state. [1]

It is important to note here that in this study the hydrodynamic aspects have been explored in 'clean' systems. The applications where the slippery interfaces can be harnessed often include contaminants which could create surface tension gradients. Shear-free bubble surfaces have been reported to have increased drag coefficients when contaminated by surfactants. [11] It is of great interest to examine the hydrodynamic slippage on the presented bubble mattresses when contacted with various kinds of surfactant solutions at different concentrations.

Another interesting future perspective on the presented bubble mattress design is the hydrodynamic slippage of shear thinning/thickening liquids. Effective slippage is described in terms of the effective surface velocity and the surface shear rate. In this context, the fundamental aspects of slippage in non-Newtonian systems are of particular interest. As the velocity and shear rate gradients at the slippery surface would alter shear-rate-induced effects such as shear-thinning, shear-thickening and time-dependency.

Slippage on a Bubble Mattress with Depinning Contact Lines

In the presented micro-bubble mattress studies, the bubbles are pinned and non-deformed due to operating at low Capillary Ca and Weber We numbers. The obtained results show that the morphology of the pinned

bubble surface determines the extent of slippage. It is important to note that the shear rate can affect the morphology of the gas-liquid menisci, and thereby the slippage. Pinned bubbles can be deformed and even the contact lines can be depinned under high shear and the bubbles can spread or even slide along the substrates.

A previous numerical study of Gao and Feng [12] have reported 2D simulations of a shear-flow over a periodic topology with bubbles trapped in rectangular grooves. Shear-induced depinning of the bubble contact line and the subsequent movement of the contact line on the solid has been predicted to enhance the apparent slippage. Figure 7.1 shows the predicted morphologies of the bubble surfaces with increasing Capillary number Ca, *i.e.* increasing shear rate, adopted from the study of Gao and Feng [12] where the effect of varying shear rates on the effective slippage is numerically studied.

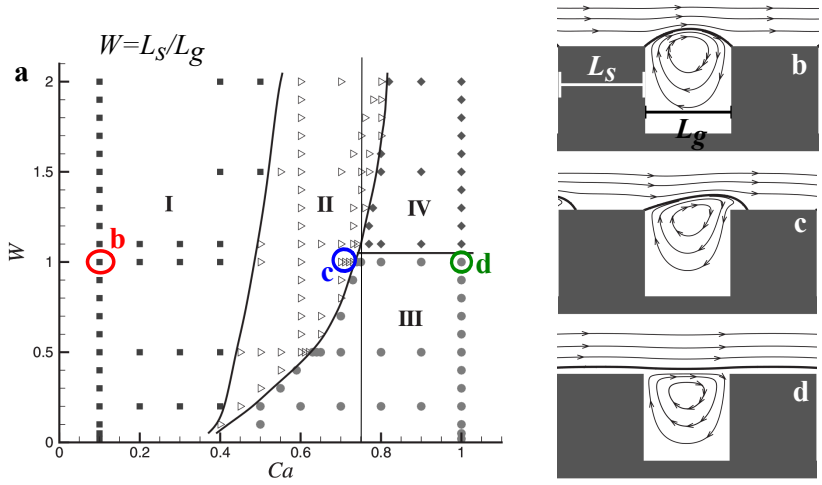

Figure 7.1: Slippage on deforming bubbles. (a) Phase diagram showing four different flow regimes as functions of Capillary number Ca and W ($=L_s/L_g$ where L_s is the width of the solid ridge and L_g is the width of the gas filled groove). (b) Regime I, with the contact line pinned at the edges of the ridge. (W =1 and $Ca = 0.1$) (c) Regime II, with the downstream contact line depinned. (W =1 and $Ca = 0.73$) (d) Regime III where the meniscus is flattened by the shear force to form a continuous gas layer. (W =1 and $Ca = 1$) (a-d) is adopted from ref. [12].

The numerical predictions suggested in the paper by Gao and Feng [12] are of interest for hydrodynamic slippage on superhydrophobic substrates with periodic gas-liquid interfaces. The presented micro-bubble device provides a suitable microfluidic platform for experimental studies of slippage associated with moving contact lines of the bubbles. The back pressurization of the gas phase is critical not only for controlling the shape of the gas bubbles but also for supplying the gas phase continuously which would allow for the formation of gas lubrication layers as in Figure 7.1d. New experiments can be designed to probe the parameter range for measuring the slip lengths with contact line depinning. Higher shear rates can be obtained by using viscous liquids.

Superhydrophobic Porous Membranes

The enhanced mass transfer properties and the promoted slippage make the presented superhydrophobic PVDF membranes prone to various applications. Some examples are cell culturing studies as porous supports (scaffolds) for cells, artificial lung studies as efficient gassing/degassing membranes. The potential advantages include the fast delivery of degassed/gassed blood samples which is of great importance in lung assisting devices. The superhydrophobicity of the presented membranes enable efficient liquid management. Furthermore, the tunable intrinsic porosity of the membranes enables the efficient supply and removal of gases eliminating any undesired size/affinity gas selectivity as encountered in dense membranes, such as PDMS. These promising properties of biocompatible, chemically resistant PVDF membranes affirm their high potential in many bio-related microfluidics, Bio-MEMS, tissue engineering, and cell culturing studies.

Slip Enhanced Marangoni Mixing

Strong enhancement in diffusio-osmosis of mass creating fluid motion induced by solute gradients has been predicted for slippery substrates. [3] In this context, hydrodynamic slippage can augment Marangoni flow which is of potential importance for dispersion of solutes in microfluidics.

Marangoni stress is caused by the surface tension gradients at the interfaces, inducing the so called Marangoni flow. Chemical potential

or temperature gradients based Marangoni stress is often encountered in microfluidic mixing studies. [13]

Marangoni stress τ_m is given as

$$\tau_m = \nabla\gamma \tag{7.1}$$

$$\tau_m = \frac{\partial\gamma}{\partial c}\frac{\partial c}{\partial x} \tag{7.2}$$

where γ and c are the surface tension and the concentration of dissolved surfactant, respectively, and x indicates the distance along the interface.

Small amounts of organic solvents are known to decrease the surface tension dramatically [14] (*e.g.* ethanol-water systems) Ethanol vapor concentration gradient can be established by the aid of the presented micro gas-liquid contacting device in this thesis. (Chapter 2) Micro-structured superhydrophobic porous PVDF membranes allow for the diffusion of vapor and gas and thereby a vapor concentration gradient at the liquid interface causing Marangoni stress at the hybrid surface $\tau_{m,s}$ perpendicular to the laminar microflow. (Fig. 7.2a) The Marangoni stress $\tau_{m,s}$ at the surface is opposed by the hydrodynamic wall shear stress $\tau_{yx,s} = \mu\partial u_x/\partial y$. Since the wall slip velocity is obtained from Navier's slip boundary condition

$$u_{x,s} = b_{eff}\frac{\partial u_x}{\partial y} \tag{7.3}$$

We get

$$u_{x,s} = \frac{b_{eff}}{\mu}\frac{\partial\gamma}{\partial x} \tag{7.4}$$

Figure 7.2 show a series of preliminary numerical simualtions of two mixing streams flowing adjacent to each other in a microchannel. For a hypothetical situation where one stream does not include any solute A ($C_A = 0$) whereas the other stream includes solute A molecules ($C_A = 1$), the convection-diffusion equation is solved for the transient concentration profiles of solute A in the liquid microchannel. (Figs. 7.2b-g) In the simulations a wall slip velocity is imposed at the boundary of the microchannel confined by the membrane. (Eqn. 7.4) The effective slip length b_{eff} is

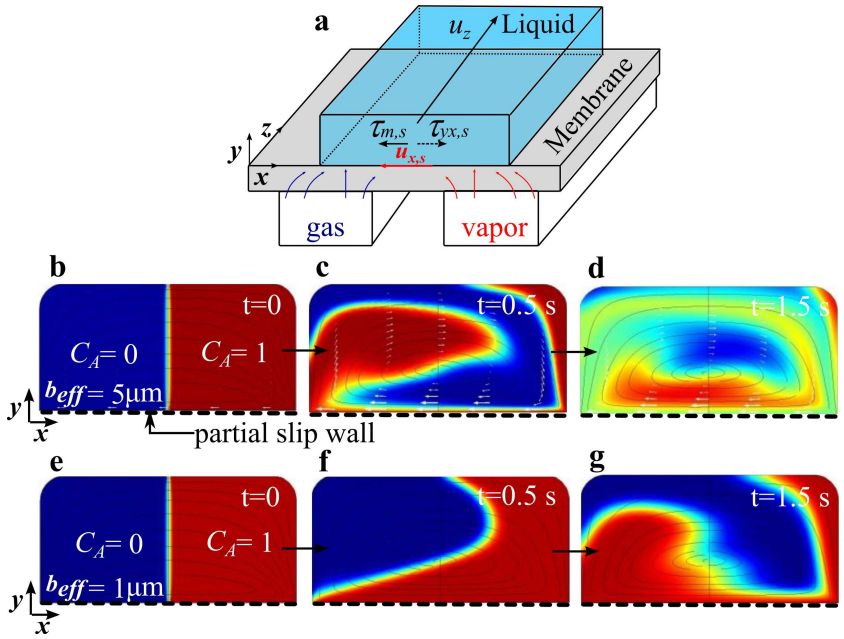

Figure 7.2: Marangoni mixing on a slippery porous membrane. (a) Illustration of slip enhanced Marangoni flow perpendicular to the main flow velocity u_z. The Marangoni stress at the membrane wall $\tau_{m,s}$ is opposed by the wall shear stress $\tau_{yx,s}$. The ethanol vapor and an inert gas diffuses through the membrane which establish surface tension gradients resulting in a Marangoni mixing in xy plane. (b-g) show numerical results of mixing of two streams in a liquid microchannel confined by slippery porous membranes, depicted by the black dash lines. Here the slip velocity and the Marangoni stress is from right to left. When $b_{eff} = 5$ μm, concentration profiles initially t=0 (b), after t=0.5 s (c), and after t=1.5 s (d). When $b_{eff} = 1$ μm, concentration profiles initially t=0 (e), after t=0.5 s (f), and after t=1.5 s (g).

varied. (= 1 μm or = 5 μm) The concentration profiles shown in Figures 7.2b-g reveal that the dispersion of A is faster for a larger slip velocity $u_s = 8.3$ mm/s when $b_{eff} = 5$ μm in comparison to that for $u_s = 1.6$ mm/s when $b_{eff} = 1$ μm. These preliminary results imply that the Marangoni mixing can be augmented by hydrodynamic slippage. Experiments can be designed using the presented micro gas-liquid contacting devices assembled

with slippery porous membranes.

7.2.2 Charged Interfaces in Microfluidics

Ion Exchange Membranes in Microfluidics

The microfluidic device integrated with an anion exchange membrane (Chapter 6) is prone to various applications aiming at charge based separations, ranging from the conventional electrodialysis in micro-scale to the new electrokinetic separations based on ion concentration polarization at intensive currents. Further development of the proposed concept include the future perspectives such as: (i) isolating the electrode effects from the separation medium by for instance employing salt bridges or reference electrode pairs [15], (ii) fabrication of micro-electrodialysis stacks including alternating anion and cation exchange membranes. Two candidates as negatively charged, water soluble monomers that can be fabricated with the developed methodology are 3-Sulfopropyl acrylate potassium salt and 2-Acrylamido-2-methyl-1-propanesulfonic acid sodium salt solution (AMPS) [16]. In addition to the presented positively charged hydrogel based membranes, a photocrosslinkable polymer poly(epichlorhydrin-co-allyl glycidyl ether) (PECH) is a highly promising membrane material for micro scale charged based separations as it is a photo-sensitive polymer and an established anion exchange membrane material. [17]

ICP induced Electrokinetic Instability

Few experimental studies focus on the mechanisms and dynamics of ICP, where the existence of the vortices and their flow streamlines visualized by particle tracking methods [18–22] and the concentration profiles in ICP shocks visualized by fluorescent intensity measurements [23]. Important questions remain regarding the nature of charge and momentum transport upon the development and propagation of ICP, and the factors determining the steady state ICP. As a result, there is a compelling need for detailed microscopic quantitative measurements of dynamics of ICP at OLC regimes. Experimental studies aiming at detailed microscopic characterization of the dynamics of ICP induced flows are lacking in the field so far. [22]

Figure 7.3 present schematics of basic micro/nano-fluidic configurations where important paramaters such as the nature of bulk fluid flow (electroosmotic or pressure-driven flow), the alignment of the applied electric field to the bulk flow direction, confinement effects can be studied by μ-PIV using (sub)micron sized neutral/charged particles seeded in various ionic strength solutions.

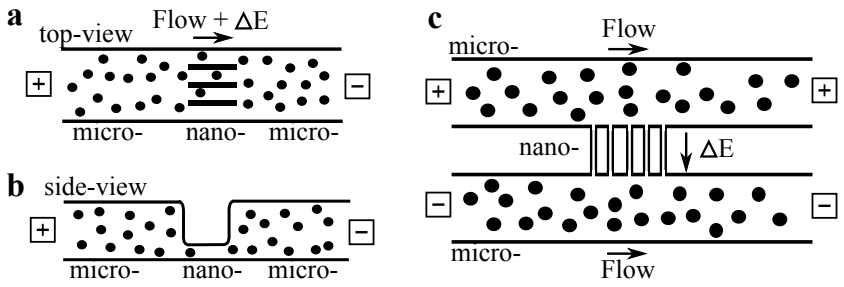

Figure 7.3: Schematic representation of basic micro/nano-fluidic devices for ICP studies at OLC. The alignment of bulk fluid flow and electric field is tangential in (a-b) and transverse in (c). Particles of different size (micro/nano) and charge are of interest.

For preliminary studies of ICP induced electrokinetic instability, microdevices including micro/nano-channel intersections were fabricated. Two microchannels dedicated for bulk fluid flow are connected by an array of 10 nanochannels with depths of ~ 10 nm. (Fig. 7.4c-d)

Figures 7.5a-d show time stacks of optical microscopy images. The solutions were initially at static conditions with no forced convection. A voltage was applied on the three electrodes on the upper microchannel. (V_1, V_2 and V_3) The two electrodes on the bottom microchannel (V_0)

Micro/nanochannels were fabricated on a Borofloat glass wafer. First the photolithography for nanochannel patterns was performed followed by wet etching. A sacrificial chromium/gold (Cr/Au) layer was sputtered on the glass wafer including nanochannels. The photolithography for microchannel patterns was performed on this Cr/Au layer. After wet etching of 20 μm deep microchannels, the sacrificial Cr/Au layer was removed. The fluidic access holes and the opening for electrode pads were fabricated by powder-blasting technique. The micro/nano-channel wafers were confined by a glass wafer including the metal electrodes by anodic bonding. Titanium/platinum (Ti/Pt) electrodes were patterned on Schott glass wafers by photolithography followed by metal sputtering. The residual Ti/Pt layers were removed by metal lift-off procedure.

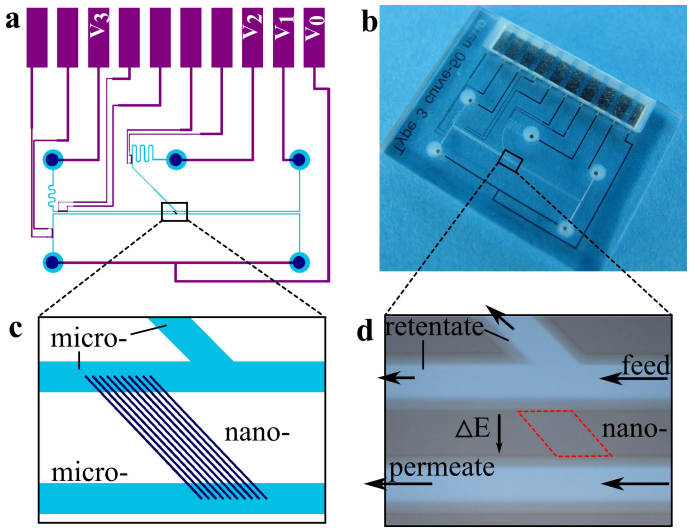

Figure 7.4: Micro/nano-fluidic devices. (a) The layout of a representative micro-device showing the micro and nanochannels, and the electrode configuration. (b) Optical image of a fabricated glass based micro-device. (c) The zoom in of (a) showing the nanochannels geometries. (d) An optical microscopy image of the nanochannels on the micro-device shown in (b). Here the flow and electric field directions are depicted by arrows, the location of the array of nanochannels are indicated by red dash lines. The hydrodynamic resistances of the two split microchannels are equal, meandering sections equating the lengths.

were grounded. The set voltage was kept constant for 20 seconds, then the voltage was directly ramped up to the other set value. Under zero DC bias voltage, the particles are uniformly distributed in both microchannels. Upon an increase in ΔV to 3 V, the particles start to enrich near the micro/nano-channel interfaces at the bottom side microchannel while the particles are locally depleted in the proximity of the micro/nano-channel intersections in the upper microchannel. Figure 7.5b shows that this depletion becomes more pronounced and extends also laterally when ΔV is 4 V. With further increase of ΔV to 6 V (Fig. 7.5c), the particle depletion extends to the whole upper channel and the remaining particles move along the walls of the microchannel. The distributions of particles vary with the variation in DC bias voltages, in agreement with a previous

experimental study where the extending ion depletion zones have been correlated to the applied voltages employing a fluorescent dye. [20]

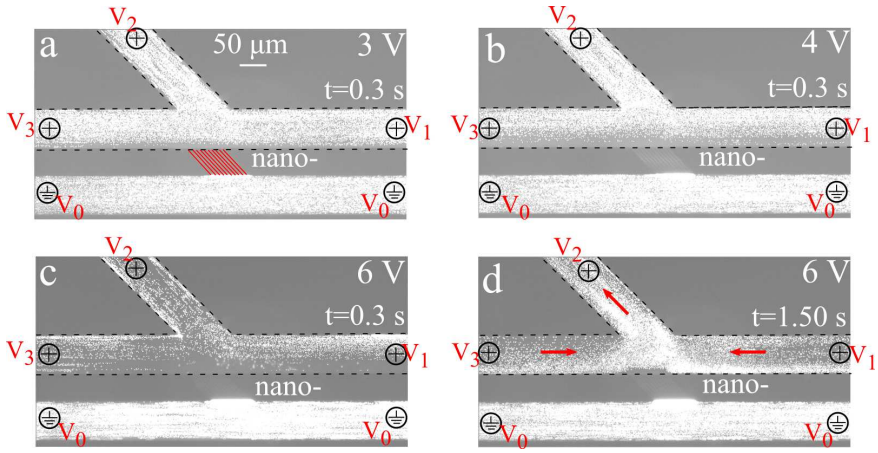

Figure 7.5: Ion depletion/enrichment layers in initially static conditions. Developing ICP with increasing potential difference, visualized by fluorescent particles. The time stack images obtained by the optical microscopy images captured after 0.3 s (a-c) and after 1.5 s (d) upon the onset of DC bias. The red arrows in (d) show the direction of the particle displacement. In (a-d) the depicted potential signs represent the voltage delivery electrode with the given labels (V_0 to V_3) at the inlet/outlet of the corresponding channel.

ICP at intensive currents under a forced convection in the microchannels is of importance since the majority of applications prone to ICP are performed under flow conditions. In Figure 7.6, a micro-flow in both upper and bottom microchannels was obtained by a hydrostatic pressure of 30 mbar at the inlets. In comparison to the results obtained for initially static conditions, the cathode side upper microchannel includes considerable amount of particles when a relatively large ΔV of 20 V is applied. After 0.3 seconds from the onset of 20 V, the particle distribution becomes nonuniform, where the particle density is less in the horizontal outlet microchannel after the split point. (Fig. 7.6a) Furthermore, here a cluster of particles circulating around an axis perpendicular to the bulk fluid flow approaches the micro/nano-channel intersections. After 0.9 seconds from the onset of voltage, this cluster of particles are directed towards the mid-

dle electrode V_2. (Fig. 7.6b) A similar chaotic spiral motion is established again at t = 1.5 s, reducing the particle loading in the horizontal outlet microchannel. These preliminary results imply the transient behavior of the observed ICP effects.

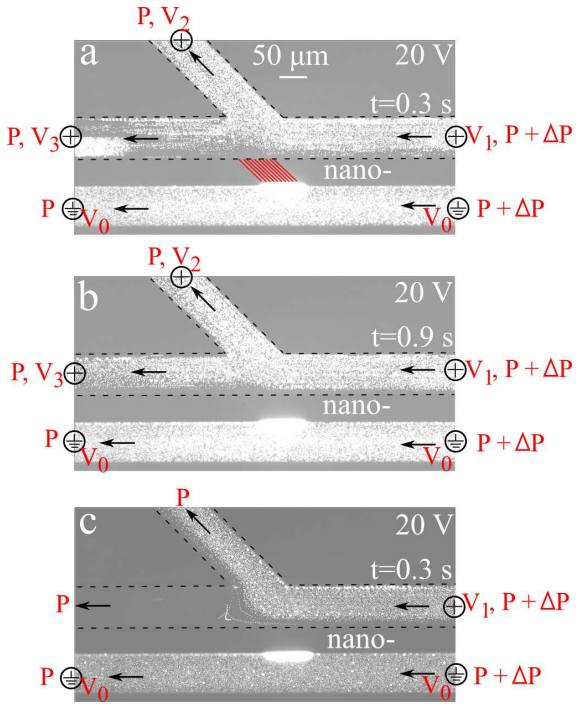

Figure 7.6: Dynamic nature of ICP at OLC under pressure-driven flow. (a-b) Each transient time stack was obtained from 30 microscopy images captured at 100 fps, immediately after each other. In (a), the bright fluorescent particle cluster at the left end of the upper microchannel spins into the depth of the channel around an axis perpendicular to bulk flow direction moving horizontally to left and right, which disappears in (b) at t = 0.9 s. (c) The outlet electrodes of the upper channel are floating potentials. Only V_1 is used for voltage delivery. In (a-c) the employed voltage delivery electrodes and the applied pressure differences are indicated. Here $\Delta P = 0.03$ bar.

Under an applied electric field and pressure-driven flow as shown in Figure 7.6, the net magnitude and direction of the particle velocities are

determined by the electrophoretic velocity components (~ on the order of 10^{-5} m/s) and the bulk fluid flow velocity (~ on the order of 10^{-3} m/s).

To obtain a better insight into the counteracting effects of electric field and bulk fluid flow directions, DC bias was applied via the cathode side inlet electrode V_1, when floating the outlet electrodes V_2 and V_3. (Fig. 7.6c) The resultant distributions of the particles are clearly different than those obtained by applying equal voltage at the three upper electrodes. In Figure 7.6c, the particles are vanished in the horizontal outlet microchannel and the particles coming from the inlet is directed towards the tilted outlet channel in the middle. The particle depletion region has a sharp boundary near the micro/nano- channel intersections parallel to the tilted nanochannels. Similar kind of ion depletion boundary layers have been reported in a previous study on water desalination by ICP at OLC regimes. [24] It is important to note here that, the obtained particle distributions in the presented preliminary experiments differ from the depletion boundary layers reported in [24] as transient profiles with an oscillation behavior in time were observed here. Besides, the electrode configuration used for the delivery of DC bias had a strong influence on the flow profiles.

The preliminary results obtained with the fabricated micro/nano-fluidic devices highlight the need for detailed transport studies of charge and momentum near ion selective interfaces at intensive currents. Substantial understanding can be gained by μ-PIV studies on dynamical electrokinetic flows at OLC regimes and by one-to-one comparisons of measurements with simulations performed at the identical settings. The investigation of ICP and its related transport phenomena is of critical importance to various fields for many conventional technologies suffering from ICP [25–27] and for many new applications operating under ICP principle [28, 29]. For example in water purification by ion exchange membranes, OLC is helpful since it leads to faster throughput (salt removal). Once the factors determining the steady state ICP at OLC are resolved, electrically driven membrane processes may be operated at OLC regimes faciliated by tailored membranes including chemical and/or physical heterogeneities. [30] Conversely, in microfluidic pre-concentration applications, the instabilities associated with OLC are undesirable since they enhance mixing and suppress the pre-concentration efficiency.

7.3 Samenvatting

Transportverschijnselen aan grensvlakken bepalen vaak de bulk transportsnelheden, zowel op microschaal als macroschaal. Derhalve is een beter begrip van vloeistofbeweging en aanverwante transportprocessen aan deze grensvlakken essentieel. Het integreren van oppervlaktes met goedgedefinieerde grensvlakken en met verschillende fysiochemische eigenschappen in microsystemen kan worden gebruikt voor het direct bestuderen van transportprocessen. Vanuit dit oogpunt is gewerkt aan de ontwikkeling van beheersbare en geoptimaliseerde grensvlakken in microkanalen, en zijn transport processen van deze grensvlakken bekeken met als aandachtspunten (i) hydrodynamische *slip* en bijbehorende massa-overdracht van het gas-vloeistof grensvlak, en (ii) ladings- en momentum overdracht van ion selectieve membranen. In dit proefschrift getiteld *Microfluidic Studies of Interfacial Transport* zijn de resultaten van het onderzoek beschreven.

In **hoofdstuk 2** worden poreuze superhydrofobe microgestructureerde polymeer membranen gepresenteerd die geïntegreerd zijn in een gas vloeistof microcontact systeem. Het massatransport van in microkanalen opgelost gas, gestuurd door convectie-diffusie, is zowel experimenteel als numeriek bestudeerd. Gas absorptie metingen tonen de sterke invloed van de morfologie van het membraan op het vergassen/ontgassen van vloeistoffen. De experimentele resultaten behaald met vlakke hydrofobe membranen - met onderling verbonden en met gas gevulde poriën - tonen een efficiënte levering van gassen aan vloeistoffen, en komen goed overeen met uitgevoerde simulaties met als uitgangspunten verwaarloosbare gasfase en membraan massatransport beperkingen. Microgestructureerde membranen behalen een tot 28% hogere gasopname ten opzichte van vlakke membranen. De superhydrofobiciteit van deze membranen garandeert de Cassie-Baxter toestand van de gas-vloeistof grensvlakken in de poreuze microstructuren, en bewerkstelligt derhalve hybride gas-vloeistof en vloeistof-vaste stof grensvlakken die de effectieve hydrodynamische *slip* bevorderen. De resulterende *slip* leidt tot een verhoogd massatransport van opgelost gas door de gas-vloeistof grensvlakken.

Hoofdstuk 3 bespreekt de numerieke simulaties van momentum en massatransport in de buurt van hybride oppervlaktes met afwisselend gas-vloeistof en vloeistof-vaste stof grensvlakken, d.w.z. periodieke gasbel eenheden. Deze zogenaamde gasbel matrassen bevinden zich op de

grens van microkanalen die loodrecht georiënteerd zijn ten opzichte van de drukgestuurde laminaire stroming. De invloed van de geometrie van grensvlakken van shear-free microbel oppervlaktes op de hydrodynamische *slip* en massa-overdracht van oplossende stoffen aan het gas-vloeistof grensvlak is onderzocht. De uitsteekhoek θ van de microbellen in de vloeistofstroom en de shear-free fractie φ van de gasbel eenheden (d.w.z. oppervlakte porositeit) zijn gevarieerd in de numerieke simulaties. De effectieve *slip* lengtes en massatransport fluxen van oplossende stoffen aan het gasbel oppervlak zijn verkregen door θ en φ te variëren.

Uit de simulaties blijkt dat de effectieve *slip* sterk afhangt van de uitsteekhoek θ van gasbellen in de vloeistofstroom. De numerieke resultaten tonen een maximale effectieve *slip* lengte voor een uitsteekhoek $\theta \approx 10^o$. De effectieve *slip* lengtes nemen af voor toenemende uitsteekhoeken voor $\theta \gtrsim 10^o$. Dientengevolge is er een kritische uitsteekhoek ($\theta_c = 55^o$) waar een transitie van *slip* naar frictie plaatsvindt. De simulatieresultaten tonen de grote invloed aan van de grensvlak-geometrie van de gasbel matrassen, d.w.z. uitsteekhoek θ van de microbellen en oppervlakte porositeit φ, op de massa-overdracht van het grensvlak. Voor de optimale uitsteekhoek $\theta \approx 10^o$ en $\varphi = 0.67$ geven simulaties een toename in massa-overdracht tot 11% t.o.v. een volledig verzadigde niet-gladde wand. De voorgestelde gasbel matras geometrie bootst fictieve poreuze gas-vloeistof contact membranen met regelmatige poriën na. Experimentele verificatie van de beschreven numerieke resultaten is van het grootste belang voor de essentiële aspecten van de hydrodynamische *slip* en het massatransport over het grensvlak, bijvoorbeeld gas absorptie/desorptie processen die relevant zijn voor zowel nieuwe als conventionele toepassingen op micro- en macroschaal.

In **hoofdstuk 4** worden nieuwe superhydrofobe microfluïdische systemen gepresenteerd met de mogelijkheid tot het generen van stabiele en controleerbare microbellen op de grens van de microkanalen. De voorgestelde microfluïdische aanpak omvat het onder druk brengen van gas, wat zorgt voor een actieve beheersing van de kromming van de gas-vloeistof menisci, dat op zijn beurt invloed heeft op zowel de statische als dynamische respons van het grensvlak. De effecten van dergelijke unieke actieve microbellen op drukgestuurde vloeistof microstromen zijn experimenteel en numeriek bestudeerd. Lokale stromingsprofielen zijn bepaald met behulp van de techniek micro-particle image velocimetry op hoge resolutie. De eerste ex-

perimentele resultaten voor effectieve *slip* lengtes zijn verkregen voor een breed scala van uitsteekhoeken θ van de microbellen in de vloeistofstroom (-2° to 12°). De metingen laten een maximale effectieve *slip* lengte zien als θ in het bereik van -2^o tot 12^o ligt, overeenkomend met een wrijvingsvermindering tot 21%. Dit is in overeenstemming met simulaties, waaruit bleek dat er een maximale effectieve *slip* lengte is voor $\theta \approx 10^o$ met een vermindering van de wrijving van 23%.

De experimentele resultaten behaald met dit superhydrofobe gasbel matras laten zien dat de hydrodynamische wrijving in microkanalen, en daarmee de convectieve stromingsdoorvoer, mogelijkerwijs kan worden geoptimaliseerd middels het actief regelen van de grensvlak-geometrie van de ingebedde microbellen. Overeenkomstig aan andere oppervlakte verschijnselen op microschaal kunnen de behaalde grote *slip* lengtes en grote wrijvingsverminderingen ook gunstig zijn voor bepaalde macroscopische toepassingen. De verwachting is dat weerstandsvermindering schaalt als de verhouding van de *slip* lengte tot de dikte van de grenslaag. [1] De behaalde resultaten met gasbel matrassen impliceren mogelijkheden om bedrijfskosten en energieverbruik voor de levering van vloeistoffen te verminderen (in vergelijking met conventionele buizen met de beperking van niet-gladde wanden).

Hoofdstuk 5 gaat over de absorptie van zuiver gas in een laminair stromende vloeistof. Hiervoor zijn superhydrofobe microfluïdische systemen gebruikt, waarmee het mogelijk is stabiele en actief beheersbare microbellen te creëren op de grens van microkanalen. De massa-overdracht van het in de vloeistof oplossende gas over de gekromde grensvlakken is bestudeerd voor korte contacttijden. De dynamiek van gas absorptie is onderzocht met behulp van *fluorescent lifetime imaging microscopy* daar waar microbellen van zuurstofgas werden gevormd. Voor opgelost zuurstof is de dynamiek van de massa-overdracht van het grensvlak numeriek geanalyseerd, met in acht neming van (i) de kinetische evenwichtscondities bij microbel oppervlaktes (conventioneel beschreven door de wet van Henry), en (ii) de *Statistical Rate Theory* (SRT) in geval van niet-evenwichtscondities aan deze oppervlaktes.

De metingen tonen aan dat er geen kinetisch evenwicht tot stand komt aan de gas-vloeistof grensvlakken in geval van korte contacttijden tussen de vloeistof en de microbellen. Massa-overdracht tussen de microbellen en

de vloeistofstroom kan goed worden beschreven met simulaties uitgevoerd voor niet-evenwichtscondities voor korte blootstellingstijden (~180 μs), en wijken derhalve af van de algemeen gebruikte wet van Henry. De gasbel matrassen met verhoogde convectie leiden tot wand *slip* snelheden in de orde van 10^{-2} m/s. Dergelijke *slip* snelheden resulteren in zeer korte contacttijden tussen het water en elke afzonderlijke gasbel, wat de niet-evenwichtsconditie kan verklaren.

Uit de experimenteel gemeten en numeriek berekende convectieve massa fluxen van opgelost zuurstof blijkt dat een lichte stijging van het Reynolds getal (Re) resulteert in een verbeterde grensvlak massa-overdracht. Ondanks het feit dat hogere Reynoldsgetallen (Re) leiden tot afnemende contacttijden (d.w.z. lagere concentraties van opgelost zuurstof aan het grensvlak), resulteert de verbeterde hydrodynamica in een verhoogde convectieve massa flux. In overeenstemming met literatuur [2, 3] alsmede de resultaten beschreven in hoofdstuk 3, tonen deze resultaten betreffende gas absorptie van microbel oppervlaktes aan dat hydrodynamische *slip* het grensvlak massatransport van hybride substraten, bestaande uit gas-vloeistof en vloeistof-vaste stof grensvlakken, versterkt.

Hoofdstuk 6 beschrijft de integratie van op hydrogel gebaseerde anion-uitwisselingsmembranen in microfluïdische systemen met controleerbare hoeveelheden ionische groepen. Het implementeren van geladen membranen met een hoge ion uitwisselingscapaciteit in microkanalen is zeer wenselijk voor ladingsgebaseerde scheidingen. Er is een selectieve, lichtgeïnduceerde methode ontwikkeld voor de *in-situ* fabricage van op hydrogel gebaseerde membranen in microkanalen.

Als eerste is de membraanchemie afgestemd richting optimale vormingscondities voor microfluïdische toepassingen. De membraanvorming is in detail onderzocht, met specifieke aandacht voor het uitzettingsgedrag van de verkregen membranen. De chemische samenstellingen van de op poly(DADMAC) gebaseerde membranen zijn gemodificeerd op grond van de evenwichtsuitzettingstheorie [4] middels (i) het mengen van het geladen monomeer DADMAC met verschillende neutrale monomeren, (ii) het variëren van de hoeveelheid van het geladen monomeer in de basismembraan oplossing, waardoor de ladingsdichtheid gevarieerd wordt, (iii) het variëren van de hoeveelheid *crosslinker agent* in de basismembraan oplossing, waardoor de dichtheid van *photo-crosslinking* gevarieerd wordt. Er zijn

derhalve verschillende types hydrogel met een regelbare uitzettingsgraad en ladingsdichtheid ontwikkeld.

Vervolgens zijn parameters die gerelateerd zijn aan *in-situ* licht geïnduceerde fabricage methodes onderzocht, met als doel het creëren van lokale, middels licht gepatroneerde membranen in microkanalen met behulp van selectieve UV-belichting. Met de ontwikkelde methode zijn daadwerkelijk membranen gerealiseerd in microfluïdische systemen voor scheidingen op basis van lading. Met geladen fluorescerende kleurstoffen en deeltjes zijn basis-experimenten uitgevoerd om de lokale lading en momentum overdracht in deze nieuwe geïntegreerde IEM systemen te onderzoeken. Het lokale ion transport door *in-situ* gemaakte anion uitwisselingsmembranen is geverifieerd middels passieve diffusie experimenten alsmede een externe DC bias. De verkregen experimentele bevindingen duiden op de perm-selectiviteit van de *in-situ* gerealiseerde microfluïdische membranen, wat van primair belang is voor veel ladingsgebaseerde scheidingen.

Bibliography

[1] Bocquet L, Lauga E (2011) A smooth future? *Nature Mater.* 10:334-337.

[2] Bocquet L, Barrat J-L (2007) Flow boundary conditions from nano- to micro-scales. *Soft Matter* 3:685-693.

[3] Ajdari A, Lydéric B (2006) Giant amplification of interfacially driven transport by hydrodynamic slip: diffusio-osmosis and beyond. *Phys. Rev. Lett.* 96(18):186102.

[4] Flory PJ (1953) *Principles of polymer chemistry*, (Cornell University Press).

[5] Rothstein JP (2010) Slip on superhydrophobic surfaces. *Annu. Rev. Fluid Mech.* 42:89-109.

[6] Zheng Q-S, Yu Y, Zhao Z-H (2005) Effects of hydraulic pressure on the stability and transition of wetting modes of superhydrophobic surfaces. *Langmuir* 21:12207-12212

[7] Govardhan RN, Srinivas GS, Asthana A, Bobji Ms (2009) Time dependence of effective slip on textured hydrophobic surfaces. *Phys. Fluids* 21:052001.

[8] Lee C, Kim CJ (2011) Underwater restoration and retention of gases on superhydrophobic surfaces for drag reduction. *Phys. Rev. Lett.* 106:014502.

[9] Krupenkin TN *et. al.* (2004) Underwater restoration and retention of gases on superhydrophobic surfaces for drag reduction. *Langmuir* 20:3824-3827.

[10] Boreyko JB, Christopher HB, Celeste RP, Chen C-H (2011) Wetting and dewetting transitions on hierarchical superhydrophobic surfaces. *Langmuir* 27(12):7502-7509.

[11] Takagi S, Matsumoto Y (2010) Surfactant Effects on Bubble Motion and Bubbly Flows. *Annu. Rev. Fluid Mech.* 43:615-636.

[12] Gao P, Feng JJ (2009) Enhanced slip on a patterned substrate due to depinning of contact line. *Phys. Fluids* 21:102102.

[13] Mitre E *et. al.* (2007) Turbo-mixing in microplates. *J. Biomol. Screen.* 12(3):361-369.

[14] Vazquez G, Alvarez E, Navaza JM (1995) Surface tension of Alcohol + Water from 20 to 50 ^{o}C. *J. Chem. Eng. Data* 40(3):611-614.

[15] Kim SK, Kim JH, Kim KP, Chung TD (2007) Continuous low-voltage dc electroporation on a microfluidic chip with polyelectrolytic salt bridges. *Anal. Chem.* 79(20):7761-7766.

[16] Walker CW (2002) Proton-conducting polymer membrane comprised of a copolymer of 2-acrylamido-2-methylpropanesulfonic acid and 2-hydroxyethyl methacrylate. *J. Power Sources* 110(1):144-151.

[17] Sollogoub C *et. al.* (2009) Formation and characterization of crosslinked membranes for alkaline fuel cells. *J. Mem. Sci.* 335(1):37-42.

[18] Rubinstein SM, Manukyan G, Staicu A, Rubinstein I, Zaltzman B, Lammertink RGH, Mugele F, Wessling M (2008) Direct observation of a nonequilibrium electro-osmotic instability. *PRL* 101(23):236101.

[19] Kwak R, Guan G, Peng WK, Han J (2012) Microscale electrodialysis: Concentration profiling and vortex visualization. *Desalination* 308:138-146.

[20] Kim SJ, Wang YC, Lee JH, Jang H, Han J (2007) Concentration polarization and nonlinear electrokinetic flow near a nanofluidic channel. *Phys. Rev. Lett* 99:044501.

[21] Yossifon G, Chang HC (2010) Changing nanoslot ion flux with a dynamic nanocolloid ion-selective filter: Secondary overlimiting currents due to nanocolloid-nanoslot interaction. *Phys. Rev. E* 81:066317.

[22] Kwak R, Pham VS, Lim KM, Han J (2013) Shear Flow of an Electrically Charged Fluid by Ion Concentration Polarization: Scaling Laws for Electroconvective Vortices. *Phys. Rev. Lett.* 110(11):114501-114506.

[23] Zangle TA, Mani A, Santiago JG (2009) On the propagation of concentration polarization from microchannel-nanochannel interfaces part II: Numerical and experimental study. *Langmuir* 25:3909-3916.

[24] Kim SJ, Ko SH, Kang KH, Han J (2010) Direct seawater desalination by ion concentration polarization. *Nature Nanotech.* 5(4):297-301.

[25] Mishchuk N (2010) Concentration polarization of interface and nonlinear electrokinetic phenomena. *Adv. Coll. Int. Sci.* 160:16-39.

[26] Manzares JA, Murphy WD, Mafe S, Reiss H (1993) Numerical simulation of the nonequilibrium diffuse double layer in ion-exchange membranes. *J. Phys. Chem.* 97:8524-8530.

[27] Nikonenko VV *et al.* (2010) Intensive current transfer in membrane systems: Modelling, mechanisms and application in electrodialysis. *Adv. Coll. Int. Sci.* 160:101-123.

[28] Kim SJ, Han J (2008) Self-sealed vertical polymeric nanoporous-junctions for high throughput nanofluidic applications. *Anal. Chem.* 80:3507-3511.

[29] Wang YC, Han J (2008) Pre-binding dynamic range and sensitivity enhancement for immuno-sensors using nanofluidic preconcentrator. *Lab Chip* 8:392-394.

[30] Balster JH (2006) *Membrane module and process development for monopolar and bipolar electrodialysis*, (PhD thesis, TNW-MTG, University of Twente).

Acknowledgements

DURING the course of my doctoral research, many people provided their kind and generous support to me. It is a pleasure to express my sincere gratitude to first of all, my promoter Rob Lammertink, who has been also my daily supervisor, or in other words my 'mentor'. I am grateful for all the time he has given for me and the invaluable knowledge, rich experiences he has conveyed to me. I would like to express my sincere gratitude to Peichun Amy Tsai for being my daily supervisor in the last months. I am grateful for her guidance, support, criticism and for all the inspiring discussions.

I am indebted to Detlef Lohse, Han Gardeniers and Chao Sun for their invaluable contributions to this research. I am grateful to them for all the valuable knowledge and rich experience. I owe my gratitude to Matthias Wessling for his support, encouragement and guidance. I would like to thank Mark Hempenius, Jan Eijkel and Ron Gill for the beneficial discussions and their inspiring suggestions.

I would like to thank the members of my research group, Soft Matter, Fluidics and Interfaces (SFI), not only for the cooperative, peaceful and fruitful working environment, but also for the great company. I would like to also thank the members of Mesoscale Chemical Systems Group (MCS), Membrane Science and Technology Group (MST) and the Inorganic Membranes Group (IM). It has been a pleasure for me to work together with all of you. I thank Antoine Kemperman, Nick Benes, Louis Winnubst, Zandrie Borneman, Herman Teunis, John Heeks, Ineke Punt and Harmen Zwijnenberg for their support and kind understanding in several ways. I

owe my special thanks to Lidy Harryvan and Greet Kamminga for their understanding, patience to my endless questions and the great support in all the paperwork.

Having a classical chemical engineering and membrane technology background before starting this research, many people kindly helped me to gain experience in microfabrication techniques. I am grateful for all the knowledge, tips and tricks from Stefan Schlautmann and Christiaan Bruinink. I thank Roald Tiggelaar for the inspiring discussions, for his invaluable support. I thank Jan Van Nieuwkastelle for sharing his microfluidic chip holder designs. I thank Ad Sprenkels for the beneficial discussions on conductivity measurements. I thank Alex Vermaning for his efforts and enthusiasm in conductivity measurements.

During the course of my doctoral studies, I had the opportunity to work with four master students, Sander Haase, Julian Crediet, Hein Verputten and Aljosha Hupje, and one bachelor student, Hannah Ijmker. I would like to thank them for the nice work they have done, which have further improved this research. I would like to also thank Claas Willem Visser for his collaboration and his contributions.

In Enschede, where I first moved alone four years ago, I got the chance to meet many nice people, who have become friends soon. Many thanks for the great company in the office, in the labs, in the SFI breaks, and more importantly out there in the 'life'. I would like to also thank all my Turkish friends with whom our paths crossed in Enschede. Special thanks to my paranymphs, Yali and Stefan, Berk, Pinar, Roald, Roland, Seckin and Sinem for all the sharing!

Last but never the least, I would like to thank to very special people for me, Cem and my mother Emel. I am well aware that words are just too simple to describe my gratitude to you and the intimacy we share which always make me feel 'at home' wherever I am or whatever has happened. Cem, thank you for your presence, understanding and patience. Mother, thank you for being always there for me, for your endless love and unwavering belief in me. Without your support, I would not be the person I am today.

Elif

When the music is over, turn off the lights...

A

Conductivity Measurements

A.1 Calibration of the Impedance Analyzer

Stock NaCl aqueous solutions were prepared in the concentration range 0.1 mM to 100 mM. The conductivity of the stock NaCl solutions were measured by a bench scale conductivity probe. (WTV, Cond3110) Figure A.1 shows the conductivities G (S/cm) measured in bench scale, as a function of the concentrations C (mM) of the stock solutions.

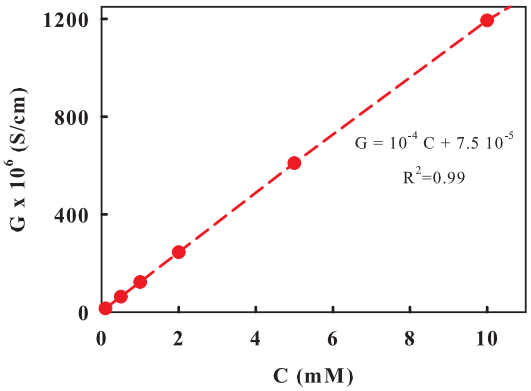

Figure A.1: Conductivities of the stock solutions as a function of salt concentration, measured by a bench scale conductivity probe.

The microfluidic devices presented in Chapter 6 include three conductivity measurement electrode pairs. The calibration of the on-chip impedance analyzer was performed for each conductivity measurement electrode pair by the stock NaCl solutions. Blank microchannels without an integrated membrane were filled with the salt solutions. The electrical resistances Z (Ω) and the phase levels were measured under static and flow conditions. Figure A.2a-b show a representative Bode plot obtained for a conductivity measurement electrode pair on a three-channel design microfluidic device for various ionic strength NaCl solutions.

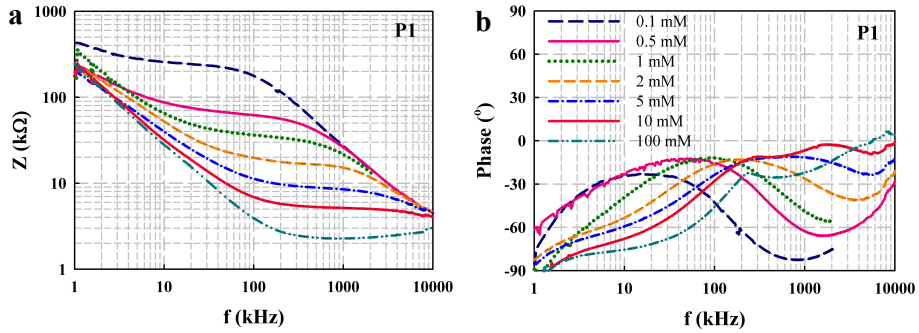

Figure A.2: A representative measured Bode plot. (a) Impedance magnitude measurements as a function of frequency for varying salt concentrations C. (b) Impedance phase measurements as a function of frequency for varying salt concentrations C, of the same measurements shown in (a).

The impedance Z is frequency f dependent on planar finger type conductivity electrodes. [1,2] The electrical characteristics of such conductivity cells are typically described by simplified equivalent electrical circuit models including the resistance of the electrolyte solution R_{el}, the capacitances formed by the electrical double layers C_{DL} and the cell capacitance C_{cell}. [1,2] The plateau region represents the resistance of the

1 Vrouwe E (2005) *Quantitative microchip capillary electrophoresis for inorganic ion analysis at the point of care*, (PhD thesis, EWI-BIOS, University of Twente).

2 Olthuis W, Streekstra W, Bergveld P (1995) Theoretical and experimental determination of cell constants of planar interdigitated electrolyte conductivity sensors. *Sens. Actuat. B* 24-25:252-256.

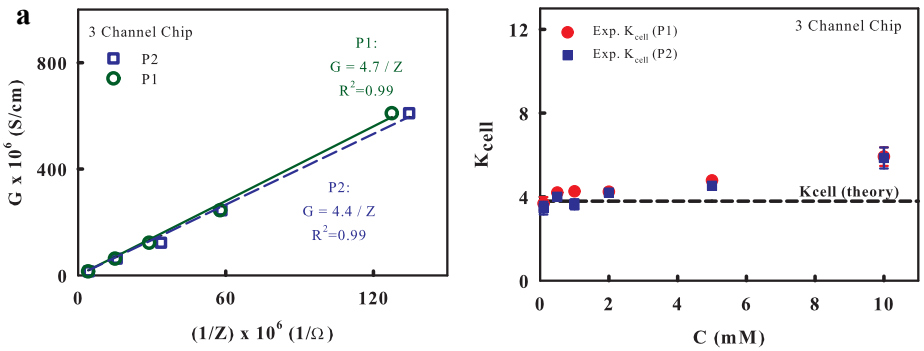

Figure A.3: Measured and calculated cell constants K_{cell}. (a) The measured conductance $(1/Z)$ with respect to the conductivities of the stock solutions having different ionic strengths. P1 and P2 are two distinct electrode pairs in a three-channel design device, having identical geometries. The slopes show the experimental K_{cell} values for P1 and P2 electrodes. (b) The experimentally obtained K_{cell} values for P1 and P2 electrodes in (a) are compared with the calculated K_{cell}, depicted by the black dash line.

electrolyte solution obtained at optimal frequency ranges for conductivity measurements where the measured phase values approach 0^o, confirming the resistive behavior in this region. (Fig. A.2)

The measured electrical resistances Z at optimal frequency regions can be correlated to the conductivity of the stock solutions. (Fig. A.2a) Following Ohm's Law, the electrical resistance Z (Ω) and the conductance σ (S) are proportional, $Z = 1/\sigma$. The measured conductance σ, *i.e.* the measured resistance Z, is related to the conductivity G as

$$G = \mathrm{K}_{cell} \cdot \sigma \tag{A.1}$$

where K_{cell} (1/cm) is the cell constant of the electrode pair. The geometry of the conductivity measurement electrode determines the cell constant. Experimental cell constants K_{cell} are obtained by the measured conductance values and the known conductivity of the salt solutions at the corresponding concentration (Fig. A.1) for each electrode pair. Figure A.3a shows the linear correlation between the measured conductances (σ=$1/Z$) and the conductivities of the salt solutions for two different electrode pairs. Here, the slopes give the experimental cell constants K_{cell}.

Since the geometry of the conductivity electrodes are identical, similar K_{cell} values were obtained.

The cell constant K_{cell} can also be determined theoretically. As described in previous studies, K_{cell} for planar interdigitated finger type electrodes is given as [1,2]

$$\mathrm{K}_{cell} = \frac{1}{(N-1)L} \cdot \frac{2K(k)}{K\left(\sqrt{1-k^2}\right)} \tag{A.2}$$

where $K(k)$ is the elliptical of first kind, given by

$$K(k) = \int_0^1 \frac{1}{(1-x^2)(1-k^2x^2)} dx \tag{A.3}$$

For electrodes with more than two fingers N > 2, k is described as

$$k = cos\left(\frac{\pi}{2} \cdot \frac{w}{w+s}\right) \tag{A.4}$$

The theoretical cell constant was calculated from the equations A.2-A.4. Figure A.3b shows the calculated and the measured K_{cell} values for varying salt concentrations of the stock solutions. Since the cell constant is determined by the geometry of the finger type conductivity electrodes, the calculated K_{cell} does not depend on the concentration. The experimental K_{cell} is in a good agreement with the calculated one in the concentration range of 0.1 mM to 10 mM (Fig. A.3b) whereas the experimental K_{cell} deviates from the theoretical value out of this range. Therefore, during the conductivity measurements, the initial concentrations of the running solutions were selected considering this operating range.

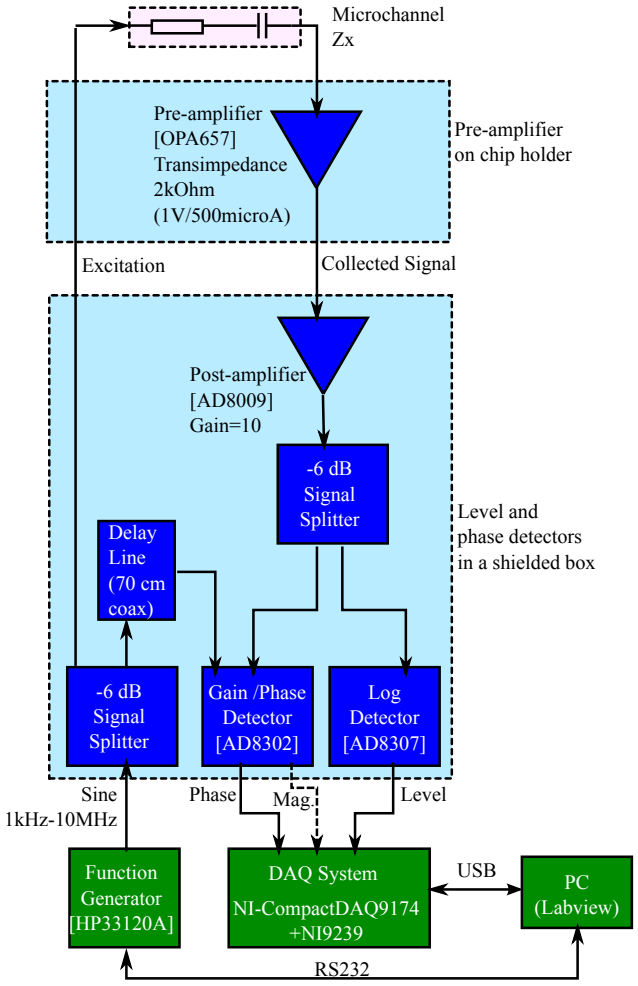

Figure A.4: The block diagram of the in-house built impedance analyzer working in constant voltage mode.

A.2 Description of the Impedance Analyzer

Impedance measurements were performed by an in-house built impedance analyzer in constant voltage mode. (TCO) The block diagram of the electronic measurement system is provided in Figure A.4. The analyzer includes two analog devices, (i) AD8307 which is the level detector and (ii)

AD8302 which is used to measure the phase angle between the excitation voltage and the current flowing through the solution resistance Z_x. The excitation voltage is split into two via a signal splitter. One part of the signal is used as the excitation voltage for the solution resistance Z_x, and the other part is sent to the AD8302 phase detector where used as a reference for the phase measurement.

The current response of the on-chip conductivity cell is measured by a trans-impedance amplifier (OPA657). This amplifier converts the current reading to its voltage value with an amplification of 10 ×. The amplified voltage splits into two. One part is sent to the log detector, for the level measurement and the other part is sent to the phase detector for the phase measurement. The phase and level measurements are performed by a data acquisition system. (NI Compact DAQ system) Labview software is used to control the function generator and the data acquisition system. An algorithm in the software calculates the complex impedance and phase values. The software allows for the electronic calibration of the the system which is performed by an open-short-load calibration procedure.

Detailed schematics showing the electronic design and circuits can be found in Figures A.5-A.7.

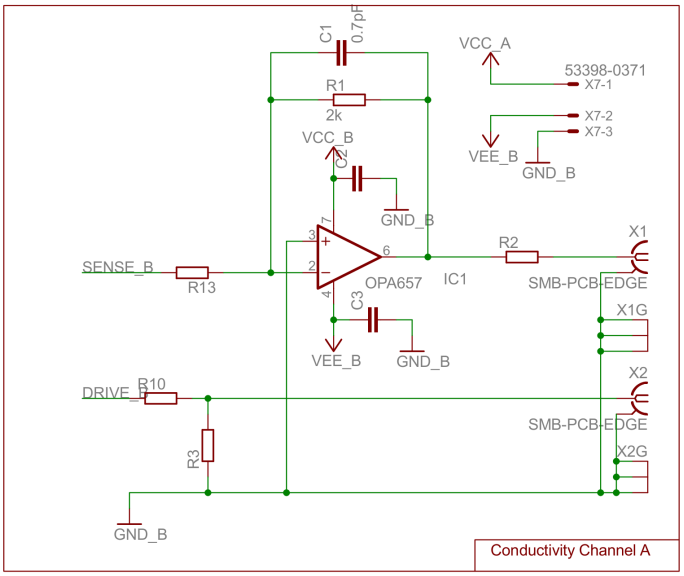

Figure A.5: Detailed schematic of one of the trans-impedance amplifier (OPA657) for one conductivity measurement electrode, provided by TCO. Three trans-impedance amplifier units were built on the chip holder for three conductivity electrode pairs.

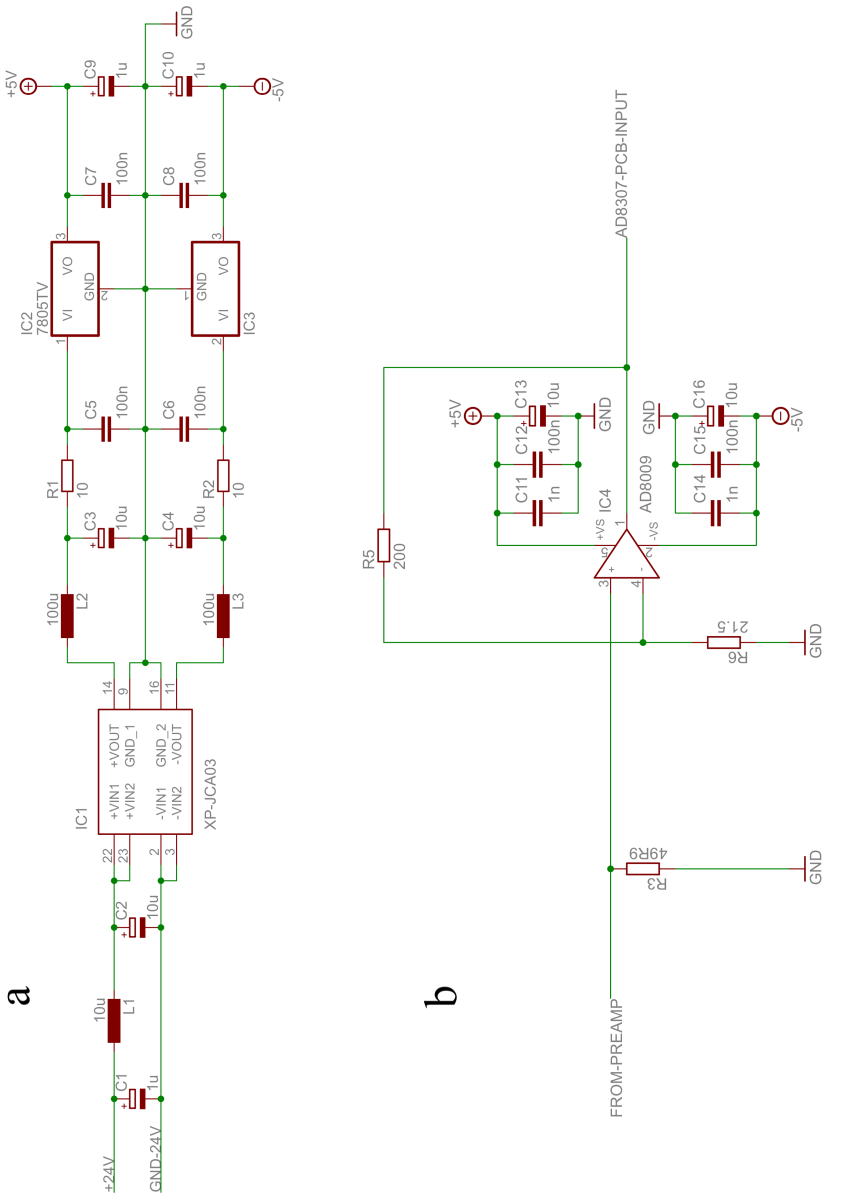

Figure A.6: Detailed schematic of the power supply (a) and post-amplifier units (b), provided by TCO.

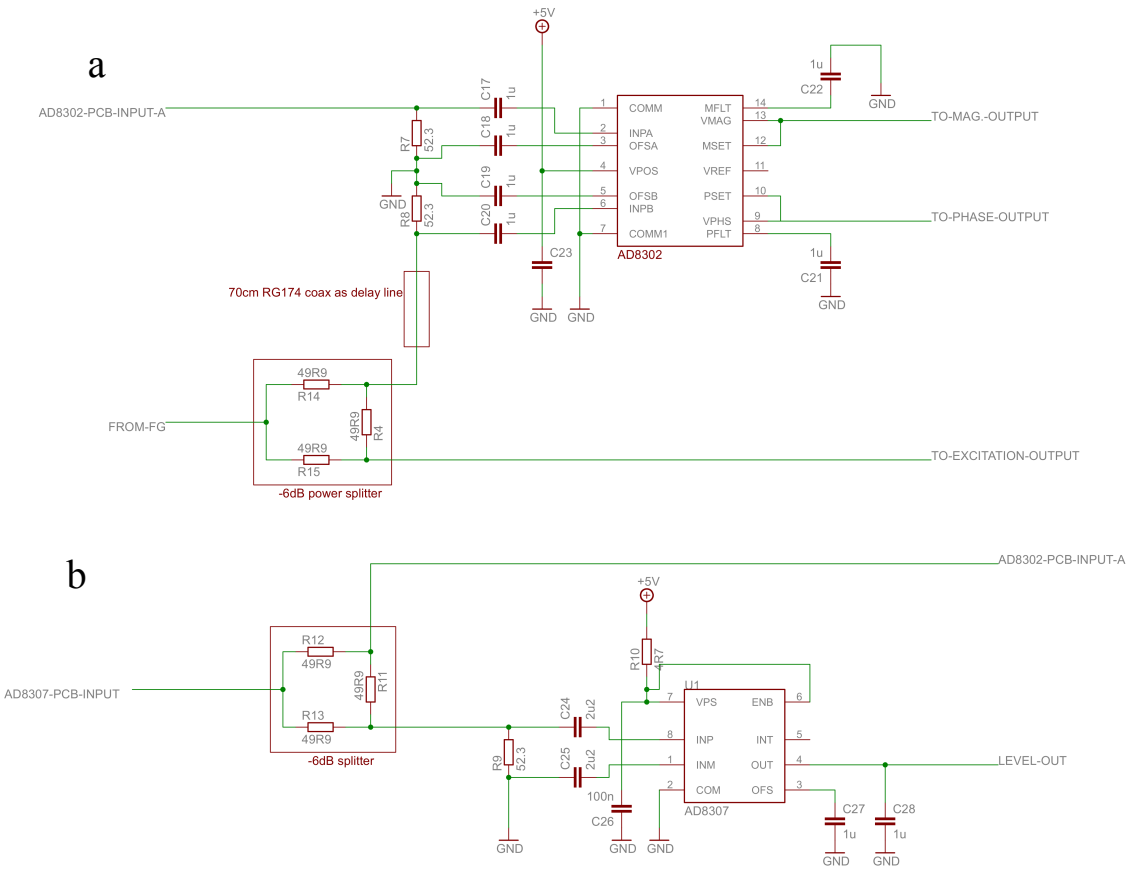

Figure A.7: Detailed schematic of the gain-phase detector (a) and logarithmic detector units (b), provided by TCO.